Max-Planck-Institut
für Meteorologie

MAX-PLANCK-GESELLSCHAFT

International Max Planck Research School
on Earth System Modelling

Modelling long-term, large-scale sediment dynamics in an Earth System Model framework

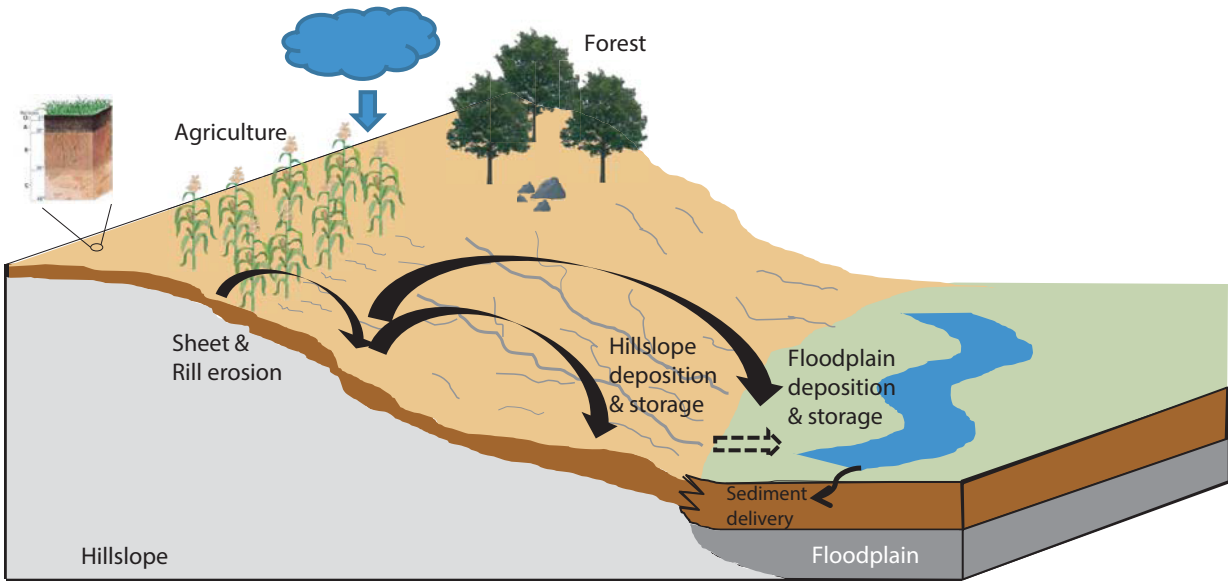

Victoria Naipal

Hamburg 2016

Berichte zur Erdsystemforschung
Reports on Earth System Science

177
2016

Hinweis

Die Berichte zur Erdsystemforschung werden vom Max-Planck-Institut für Meteorologie in Hamburg in unregelmäßiger Abfolge herausgegeben.

Sie enthalten wissenschaftliche und technische Beiträge, inklusive Dissertationen.

Die Beiträge geben nicht notwendigerweise die Auffassung des Instituts wieder.

Die "Berichte zur Erdsystemforschung" führen die vorherigen Reihen "Reports" und "Examensarbeiten" weiter.

Notice

The Reports on Earth System Science are published by the Max Planck Institute for Meteorology in Hamburg. They appear in irregular intervals.

They contain scientific and technical contributions, including Ph. D. theses.

The Reports do not necessarily reflect the opinion of the Institute.

The "Reports on Earth System Science" continue the former "Reports" and "Examensarbeiten" of the Max Planck Institute.

Anschrift / Address

Max-Planck-Institut für Meteorologie
Bundesstrasse 53
20146 Hamburg
Deutschland

Tel./Phone: +49 (0)40 4 11 73 - 0
Fax: +49 (0)40 4 11 73 - 298

name.surname@mpimet.mpg.de
www.mpimet.mpg.de

Layout

Bettina Diallo and Norbert P. Noreiks
Communication

Copyright

Modelling long-term, large-scale sediment dynamics in an Earth System Model framework

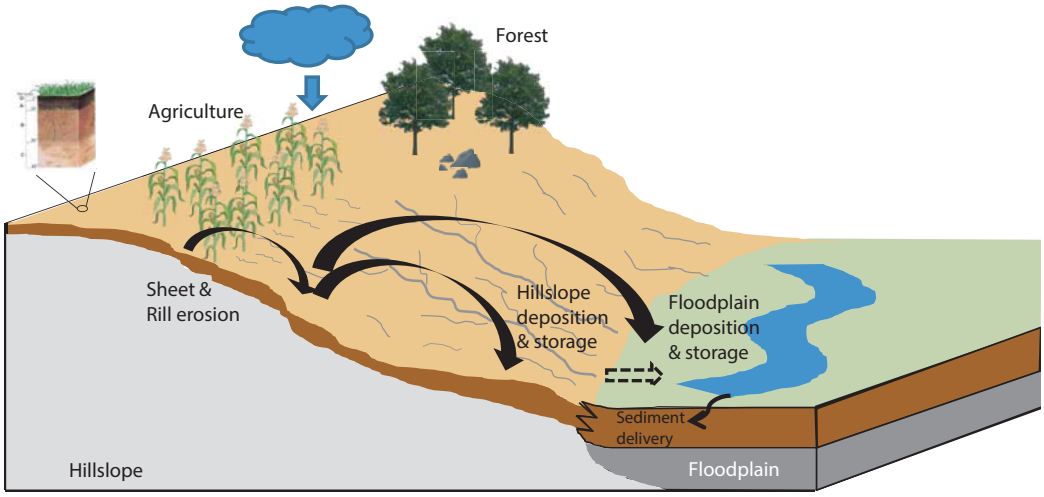

Dissertation with the aim of achieving a doctoral degree
at the Faculty of Mathematics, Informatics and Natural Sciences
Department of Earth Sciences of Universität Hamburg

submitted by

Victoria Naipal

Hamburg 2016

Victoria Naipal

Max-Planck-Institut für Meteorologie
Bundesstrasse 53
20146 Hamburg

Tag der Disputation: 12.01.2016

Folgende Gutachter empfehlen die Annahme der Dissertation:

Prof. Dr. Martin Claußen
Dr. Christian Reick

Berichte zur Erdsystemforschung / Max-Planck-Institut für Meteorologie 177
Reports on Earth System Science / Max Planck Institute for Meteorology 2016

ISSN 1614-1199

"A nation that destroys its soils destroys itself"

U.S. President Franklin D. Roosevelt

Abstract

For the last centuries soil erosion has been accelerating globally due to human activities. Accelerated soil erosion and the resulting soil redistribution have impacted the lateral fluxes of carbon and nutrients across terrestrial ecosystems. However, as Earth System Models (ESMs) ignore these lateral fluxes altogether, the anthropogenic impact to these fluxes remains unquantified. The aim of this study is to close this knowledge gap by the development of methods and tools, compatible with ESMs, to simulate long-term soil redistribution on a global scale.

In this context the computation of topographical- and rainfall erosivity factors of an existing soil erosion model (the Revised Universal Soil Loss Equation, RUSLE) was adjusted to improve the performance of the RUSLE model at a coarse resolution of ESMs. Application of the model in combination with observed data on environmental factors confirmed the accelerated soil erosion rates in many regions, with a global mean rate of $6.5\,\mathrm{t\,ha^{-1}\,year^{-1}}$ for present day. However, no specific global trend of erosion is found for the last millennium (850 - 2005AD) when data on climate and land cover from different ESMs is used. This shows that the adjusted RUSLE model is very sensitive to climate and land cover data.

In order to simulate soil redistribution, a new large-scale sediment budget model was developed. This model builds on the adjusted RUSLE model and simulates beside soil erosion, also sediment deposition in floodplains and on hillslopes, as well as sediment transport. The new model was forced with climate and land cover data from the Max Planck Institute Earth System Model (MPI-ESM) for the last millennium. The model reproduces the spatial distribution of sediment storage in floodplains when compared to observations from the Rhine catchment, and shows that the change in erosion rates during the last millennium modified the sediment budgets resulting in a significant increase in sediment storage for different catchments. Globally, land use change turned out to be the main driver behind this increase for most of the catchments during the last millennium. Here, catchment characteristics, such as slope and area, play an important role in buffering or intensifying the effect of external forces.

The main limitations of the model are related to the fact that model parameters are calibrated based on data from the Rhine catchment only, and to the neglection of other types of soil erosion. Furthermore, a general limitation in simulating historically realistic soil redistribution arises from the unknown initial state of a river catchment. Most catchments in northern latitudes have been in a transient state since the last glaciation in contrast to tropical catchments.

Finally, soil erosion can result in significant fluxes of carbon and nutrients, of which only a small part is exported by rivers globally. This indicates the importance of including sediment dynamics in ESMs to estimate the overall impact of soil redistribution on the biogeochemical cycles, and to quantify the human impact on these cycles. With the new sediment budget model an important first step is made in this direction.

Zusammenfassung

Über die letzten Jahrhunderte hat sich die Bodenerosion aufgrund menschlicher Aktivitäten global beschleunigt. Die beschleunigte Bodenerosion und die daraus resultierende Bodenumverteilung verändern den lateralen Transport von Kohlenstoff und Nährstoffen in den terrestrischen Ökosystemen. Da Erdsystemmodelle (ESMs) solch laterale Transporte nicht beschreiben, wurde der anthropogene Einfluss auf diese Flüsse bisher allerdings nicht quantitativ bestimmt. Um zur Schließung dieser Wissenslücke beizutragen, werden in dieser Arbeit Methoden und Werkzeuge für Ersystemmodelle zur Simulation der globalen Langzeit-Umverteilung des Bodens entwickelt.
Dazu wurde zunächst die Berechnung der topographie- und regenspezifischen Erosivitätsfaktoren des bereits vorhandenden Bodenerosionsmodell (Revised Universal Soil Loss Equation, $RUSLE$) an die grobe Auflösung von ESMs angepasst. In Kombination mit Beobachtungsdaten verschiedener Umweltfaktoren bestätigt die Anwendung des Modells die beschleunigten Erosionsraten für viele Regionen weltweit, mit einer heutigen mittleren globalen Bodenerosionsrate von 6.5 t ha^{-1} pro Jahr. Allerdings ergab sich für das letzte Jahrtausend (850 - 2500AD) kein global einheitlicher Trend der Bodenerosion bei Verwendung von Klima- und Landbedeckungsdaten aus verschiedenen Erdsystemsimulationen. Offensichtlich ist das angepasste RUSLE-Modell bezüglich dieser Eingabedaten sehr sensitiv.
Um die Bodenumverteilung zu simulieren, wurde ausgehend von dem angepassten RUSLE-Modell ein großräumiges Sedimentbilanzmodell entwickelt. Dieses neue Modell simuliert neben Bodenerosion auch Sedimentablagerung an Hängen und in Flußauen, sowie den Sedimenttransport. Zum Antrieb des Modells wurden Klima- und Landbedeckungsdaten aus Simulationen des letzten Jahrtausends mit dem Erdsystemmodell des Max-Planck-Instituts für Meteorologie (MPI-ESM) verwendet. Das Modell reproduziert die beobachtete Sedimentverteilung in den Flußauen des Einzugsgebietes des Rheins und zeigt weltweit für verschiedene Flusseinzugsgebiete eine starke Zunahme der Sedimentmengen infolge der Intensivierung der Erosion im letzten Jahrtausend. Landnutzungsänderungen erweisen sich weltweit für die meisten Flusseinzugsgebiete als Hauptursache dieser Entwicklung. Die Stärke des Effektes hängt stark von den Besonderheiten des jeweiligen Einzugsgebietes ab, wie etwa dessen Fläche und den herrschenden Steigungsverhältnissen.
Die Haupteinschränkungen des Modells ergeben sich durch dessen Kalibrierung allein auf Basis von Daten für das Rheineinzugsgebiet, sowie durch die Nichtberücksichtigung anderer Arten von Bodenerosion. Darüberhinaus ergibt sich eine generelle Einschränkung für die Simulation historisch realistischer Bodenumverteilung aus der Unkenntnis des Anfangszustands der jeweiligen Flusseinzugsgebiete. Im Gegensatz zu tropischen Einzugsgebieten befinden sich die Einzugsgebiete nördlicher Breiten seit der letzten Vereisung in einem transienten Zustand.
Schließlich wird in der Arbeit diskutiert, dass Bodenerosion zu starken Umverteilungen von Kohlenstoff und Nährstoffen führen kann, die aber global nur zu einem

geringen Teil über Flusssysteme exportiert werden. Hierdurch ergibt sich die besondere Notwendigkeit die globale Sedimentdynamik in Erdsystemmodelle zu integrieren um die Folgen der Bodenumverteilung für die globalen biogeochemischen Kreisläufe abzuschätzen und um zu quantifizieren, welchen Anteil der Mensch daran hat. Die Entwicklung des neuen Sedimentbilanzmodells ist ein erster wichtiger Schritt in diese Richtung.

Contents

Chapter 1

Introduction

1.1 Background

In the year 2015 the monthly mean atmospheric CO_2 concentrations have reached 400 parts per million (ppm) for the first time in recorded history based on data from the Mauna Loa Observatory in Hawaii. CO_2 concentrations have not been this high for the past millions of years (Honisch et al., 2009; Lüthi et al., 2008). This milestone has led to more concerns regarding global warming and the future climate. The Conference of Parties in Paris in the year 2015 aims, therefore, to reach a universal legally binding agreement that can lead to a reduction of greenhouse gas (GHG) emissions to limit global warming to below 2 °C (www.cop21.gouv.fr). Limiting global warming to below 2 °C is not only a political, economical and societal challenge, but also a challenge for the scientific community which still struggles to accurately quantify all present day sources and sinks of carbon.

It is well known that the increasing CO_2 concentrations is a result of rapid emissions by human activities such as fossil fuel combustion and land use change (Ciais et al., 2014). This emitted CO_2 is currently taken up in about equal parts by the ocean and the terrestrial system (Ciais et al., 2014). For the terrestrial system a net sink is observed as a result of an imbalance between several sink and source processes. However, the exact contribution of all the relevant processes behind this net sink is still unknown (Ciais et al., 2014; Friedlingstein et al., 2014).

One major reason for this knowledge gap is the ignorance of the contribution of world's soils and soil related processes, such as soil erosion, to atmospheric CO_2 concentrations and climate change (Todd-Brown et al., 2014). Soils are one of the largest stores of carbon, storing about 1500-2400 Pg of carbon, which is almost three times the quantity stored in the terrestrial biomass, and twice that in the atmosphere (Ciais et al., 2014; Lal, 2003). This soil carbon pool is in direct exchange with the atmosphere. At the same time, soils support life on our planet by storing and cleaning drinking water, supporting the production of food and keeping the air breathable (Wall and Six, 2015; Quinton et al., 2015). The United Nations (UN) have therefore recognized the year

2015 as the International Year of Soils, with the focus on the increasing pressures on soils and their ripple effect on global challenges (Wall and Six, 2015). Soil security is now a priority and several UN Sustainable Goals for the future directly or indirectly involve soil research.

Human induced alterations of soils that accelerate soil erosion can lead to significant changes in net terrestrial ecosystem carbon balances and negatively affect the society through climate change feedback's (Van Oost et al., 2012; Schuman and Herrick, 2002; Wall and Six, 2015).

For the last centuries to millennia soil erosion has been accelerating globally due to human activities, such as deforestation and agricultural practices (Bork and Lang, 2003). Currently, global rates of soil erosion exceed the rates of soil production by several orders of magnitude (Hoffmann et al., 2015; Montgomery, 2007; Wall and Six, 2015). Accelerated soil erosion is a process that triggers land degradation in the form of nutrient loss, a decrease in the effective root depth, water imbalance in the root zone and finally also productivity reduction (Yang et al., 2003). Deposition of the eroded soil downstream has lead to the alteration of fluvial ecosystem functioning and structure (Hoffmann et al., 2015). All this is a threat to sustainable agriculture and climate on the long term, that is currently exacerbated by the global population growth and climate change.

Soil erosion by rainfall and the resulting sediment deposition and transport (soil redistribution) play an important role in the mineralization and sequestration of soil carbon and the loss of carbon and nutrients from ecosystems (Van Oost et al., 2007). On the one hand, mineralization of soil carbon at eroding sites and during transport can lead to significant fluxes of GHGs (Lal, 2003; Van Oost et al., 2007; Lal, 2005). On the other hand, the transport of carbon and nutrients from a terrestrial ecosystem can result in either sequestration of carbon at deposition sites (Stallard, 1998; Van Oost et al., 2007), or significant lateral fluxes of carbon and nutrients (Van Oost et al., 2007; Quinton et al., 2010). However, the net global effect of soil redistribution on the vertical and lateral fluxes of carbon and nutrients is still unknown.

The land components of Earth System Models (ESMs) are the main tools to investigate the terrestrial carbon cycle and land use and land cover change (LULCC). They mainly represent the effects of fossil fuels and land use change on the carbon cycle and the resulting carbon flux between soil and the atmosphere (Regnier et al., 2013). However, they ignore carbon exchange associated with soil redistribution and the resulting lateral fluxes of carbon and nutrients from land to the ocean (Regnier et al., 2013; Van Oost et al., 2012).

Recent evidence demonstrated that human activities, such as land use change, fertilizer use, and those that accelerate soil erosion, have significantly altered this lateral transport (Regnier et al., 2013; Stallard, 1998; Bauer et al., 2013; Le Quéré et al., 2013). For example, Regnier et al. (2013) estimated that human activities increased the carbon flux to inland waters by as much as $1.0\,\mathrm{Pg\,C\,yr^{-1}}$. As ESMs, currently, ignore lateral flows of carbon and nutrients altogether, anthropogenic disturbance of

the biogeochemical cycles remain largely unquantified (Regnier et al., 2013).
To address this problem, soil redistribution should be included in ESMs to estimate the effects of soil redistribution on the biogeochemical cycles. Not only will this improve the understanding of human disturbances of the biogeochemical cycles, but it will also decrease the large uncertainties in the soil response to climate and land use change.
Another aspect that underpins the importance of modeling soil redistribution on a global scale is the fact that soil erosion can lead to tipping points in a landscape. A tipping point is defined as the threshold, which is reached when small changes in external conditions lead to abrupt changes in the equilibrium conditions of a system (Lenton, 2011). Accelerated soil erosion can on millennial and longer timescales lead to modifications of the landscape, in terms of soil structure and texture, nutrient and productivity loss, that result in strong positive feedbacks between soil, vegetation, hydrology and the atmosphere. Such feedback's can lead to a state or tipping point in the landscape formation from which the landscape can not recover anymore. For example, the studies of Bork (1989) and Bork and Lang (2003) show that land use change during the last millennium in Germany lead to very vulnerable soils where precipitation extremes triggered sudden strong erosion fluxes that transformed the landscape. Unfortunately, soil erosion in relation to tipping points in a landscape has not yet been studied before on a regional or global scale due to the lack of suitable techniques. Modelling soil redistribution with ESMs would therefore open the possibility to study soil-vegetation-atmosphere interactions and the overall effect on the climate system.
The overall long-term aim of this study is to contribute in quantifying the anthropogenic impact on the lateral fluxes of carbon and nutrients, through improving the understanding on how soil redistribution affects the lateral fluxes on a global scale. Soil redistribution operates on different scales of time and space, and involves interactions with multiple processes in the terrestrial system. Therefore, before introducing the specific objectives of this study, (1) the processes behind soil erosion and (2) soil redistribution, as well as (3) the effects of soil redistribution on the biogeochemical cycles, are explained in more detail.

1.2 Global soil erosion

Soil erosion describes the detachment of soil particles from the surface by rainfall or wind. This study focuses on soil erosion by rainfall. Soil erosion by rainfall comprises: splash erosion, sheet or rill erosion and gully erosion (Morgan, 2009). Splash erosion occurs when soil particles are detached from the surface and moved from their places due to the impact of falling raindrops. In this way, soil erosion is primarily related to the energy of the falling raindrops, which is a result of the precipitation intensity and amount. Sheet or rill erosion occurs when the water is concentrated in flows and transports the detached soil particles downhill. Here, the second parameter that provides energy for the soil to erode comes into light, which is the topography of the

landscape. The steeper the topographical slope, the stronger the sheet or rill erosion will be. Finally, gully erosion occurs, when the flow concentration becomes so large that the incisions in the soil created by rill erosion get deeper and wider (Thapa, 2010; Morgan, 2009).
Besides precipitation and topography there are other environmental factors, such as land cover and soil characteristics, that significantly affect soil erosion but at the same time are not the drivers behind soil erosion. On the one hand, the structure and texture of the soil to be eroded determine how resistant the soil is to splash erosion (Morgan, 2009). On the other hand, these soil characteristics determine how large the shear stress is, which affects the overland flow when rill or even gully erosion takes place (Léonard and Richard, 2004). Soils in agricultural landscapes are usually organic and lack large soil particles such as gravel that makes these soils very vulnerable to soil erosion.
Land cover can limit soil erosion due to the presence of roots that minimize the energy of overland flow (Vannoppen et al., 2015), and by the density of the land cover itself that minimizes the energy of falling raindrops (García-Ruiz, 2010). The effects of human activities on soil erosion are mainly via alternation of land cover, where for example, forest is replaced by crops and the ability of the land cover to limit soil erosion decreases (Van Oost et al., 2012). These effects are correlated with the level of land management (Renschler and Harbor, 2002). For example, tillage strongly increases soil erosion rates compared to natural conditions. Other management strategies, such as rotation of crops, cause less disastrous effects on soil erosion.
Land cover and land use interact with all the other environmental parameters that affect soil erosion, which hampers the ability to quantify the effects of land use change. For example, the effect of land use change on erosion depends on the place of land use change in the landscape. Land use change on steep hillslopes leads to larger soil erosion rates than land use change in flat areas. The effects of land use change on erosion can also be modified by precipitation. If cycles of harvesting and planting of crops coincide with strong precipitation rates, the resulting erosion rates will be larger in comparison to occasions where the strong precipitation rates occur when the plants are fully grown. It is thus essential, to capture these interactions between the different environmental parameters that affect erosion in order to estimate accurate erosion rates.
In return, soil erosion affects all the environmental parameters mentioned above (Toy et al., 2002; Morgan, 2009). Erosion affects the physical and chemical properties of soils, and at the same time vegetation growth (Toy et al., 2002). The topography can be changed on long-term due to the loss and mobilization of large amounts of soil. Finally, climate can also be influenced by erosion on centennial to millennial timescales due to the potential of erosion to significantly affect global biogeochemical cycles and plant productivity. This highlights the need to study soil erosion not as a stand alone process but rather in interaction with the dynamics of vegetation, soil, biogeochemical cycles and climate, which requires a comprehensive global approach.
The interaction of soil erosion with many components of the Earth system once more

underpins the fact that even though erosion starts as a local scale phenomenon it can have global effects. In the next section will be shown that sediment redistribution plays an important role in this interaction due to its ability of catalyzing the local impacts of soil erosion to larger scales by the transport of eroded material from land to the ocean.

1.3 Global soil redistribution

Soil redistribution is the complete cycle of soil erosion, transport of eroded material in the form of sediment by overland flow or wind, and the resulting sediment deposition. In this study, the focus is only on soil redistribution by rainfall. Soil redistribution does not always result in a net loss of soil or degraded land, but can also lead to soil formation and the improvement of soil quality and texture in deposition sites. The mount of sediment that can be transported by overland flow depends on the transport capacity of the flow, which is defined as the maximum sediment mass that can be transported (Notebaert et al., 2006). Deposition in depressions occurs when the transport capacity of overland flow is lower than the sediment production by erosion. Deposition sites can be divided into two groups, (1) the foot of hillslopes and natural and man-made barriers on the hillslopes and (2) floodplains and drainage network (Fig. 1.1). Depending on the energy of the overland flow, eroded soil particles will be first deposited on the hillslopes itself, especially when man-made barriers are created by agricultural practices. If the overland flow is stronger or the shear stress to the overland flow is lower, soil particles will be transported and deposited at the foot of hillslopes or in floodplains (Fig. 1.1). Depending on the residence time of soil particles in the floodplains they will eventually reach the drainage network (Fig. 1.1). The residence time is related to the sediment connectivity of the catchment, which describes the physical transfer of material from hillslopes to the floodplain and is mainly determined by the complexity of topography (Hooke, 2003; Hoffmann, 2015). Land use change can affect this connectivity by local scale barriers that capture eroded sediment and prevent it from being transported to the drainage network.

Due to deposition, not all of the eroded material in a catchment reaches the drainage network. The amount of sediment that does reach the drainage network and is transported downstream towards the outlet of the catchment is referred to as the sediment yield (Thapa, 2010). Although measurements of soil erosion on a large spatial scale are rare, there exists a global database on measured sediment yield from rivers (Peucker-Ehrenbrink, 2009). Sediment yield can be used to study the net effect of soil redistribution in a catchment.

External forces working on the catchment, such as land use change or climate change, can significantly alter the soil redistribution in a catchment. However, external forces do not lead to an immediate change in sediment yield due to a time lag created by the residence time of the sediments in a catchment. This complicates the investigation of external forces on soil redistribution from data on sediment yields.

Therefore, a global model is needed that can simulate sediment fluxes as a result of soil redistribution on long timescales. In addition, such a model can be used to study the effects of soil redistribution on the global biogeochemical cycles and the climate, presented in the following section.

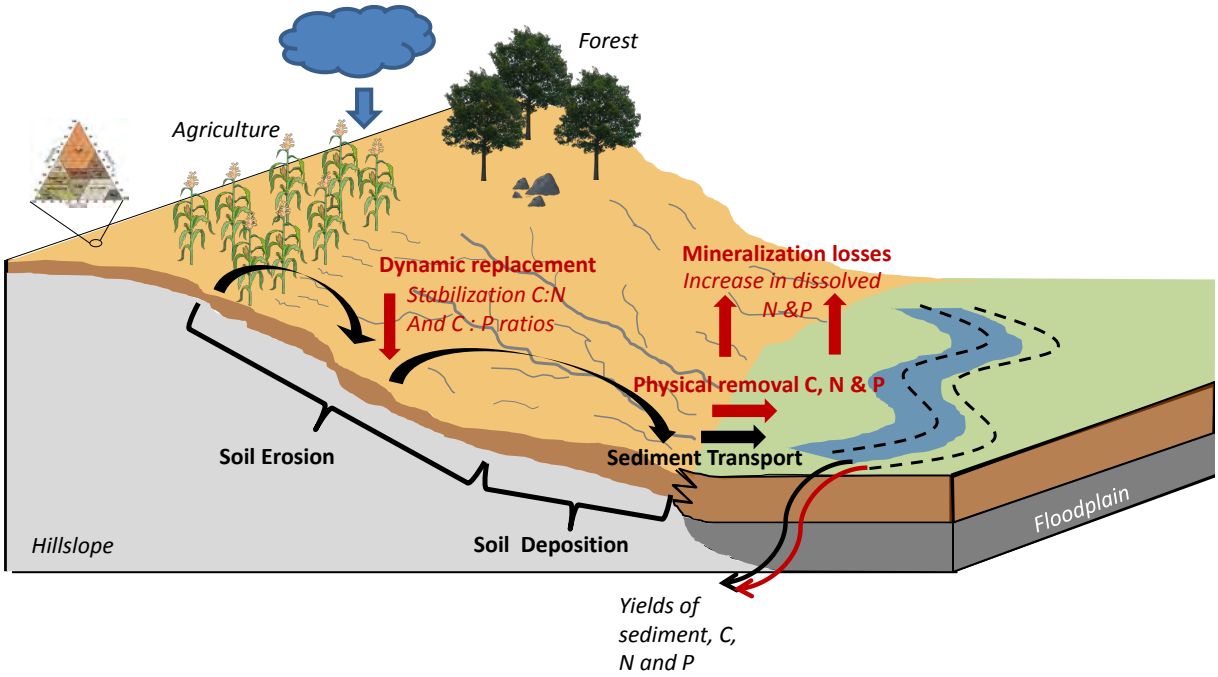

Figure 1.1: A simple representation of a landscape showing soil redistribution fluxes (black arrows) and fluxes from possible interactions with the carbon and nutrient cycles (red arrows). C, N and P stand for carbon, nitrogen and phosphorus.

1.4 Carbon and nutrient cycles

Soil redistribution affects the carbon cycle primarily through the soil organic carbon (SOC) pool (Fig. 1.1). The main processes by which soil redistribution interacts with SOC are (1) disruption of soil aggregates, (2) removal of carbon by overland flow, (3) on-site mineralization of SOC and (4) mineralization of displaced SOC or SOC that is transported in the drainage network, and finally (5) re-aggregation of soil in depressions and in the drainage network that buries carbon rich sediments in these places (Lal, 2003).

For a long time, soil redistribution has been seen as a major source of carbon emissions due to the mineralization of SOC during soil detachment, transport and deposition. The effects of soil redistribution on the global carbon cycle have received considerable attention after the pioneering work of Stallard (1998), who proposed that global soil redistribution can also result in a sequestration of carbon by soils and in a sink of

atmospheric CO_2.

On the one hand, accelerated soil erosion can promote the uptake of carbon by soils or reduce carbon emissions from soils. When soil erosion takes place, carbon is removed from the top soil and carbon-depleted subsoil is exposed. This can reduce the carbon emissions over eroding sites due to less available carbon for decomposition (Van Oost et al., 2012). At the same time carbon-depleted soils have usually a larger saturation deficit of carbon and can therefore potentially take up more carbon than noneroding sites (Van Oost et al., 2012; Stewart et al., 2007). On the other hand, carbon is sequestered in soils due to sediment deposition that buries carbon rich sediment in depressions. This burial of carbon can become a sink for atmospheric CO_2 when the eroded carbon is replaced somewhere else by means of photosynthesis. This is called dynamic replacement of carbon and usually occurs in agricultural areas. Even when carbon losses due to soil erosion are high, the use of fertilizers can promote photosynthesis such that the losses are compensated by the production of new carbon that can be fixed in buried soil. Furthermore, it should be noted that although soil erosion can be a sink for carbon, this can be temporary (Van Oost et al., 2012). Depending on the residence time of sediments in the reservoirs of a catchment the sink can become a source. Van Oost et al. (2012) indicated that carbon may be preserved effectively at annual to decadal timescales, but can result in losses of the buried carbon at centennial to millennial timescales. At the same time, the preservation of carbon is complicated by the fact that human activities can alter the residence times. The magnitude of the net effect of erosion on SOC is thus determined by the rate at which SOC is replaced on eroding sites, on the changes of reactivity of SOC as a result of transport and burial, the preservation of carbon, and the rates of erosion and deposition (Van Oost et al., 2007).

Very little work has been done on the effects of large scale soil redistribution on nutrient cycles such as the nitrogen and phosphorous cycles (Quinton et al., 2010). Soil redistribution can lead to a significant loss of nutrients from the soil system (Quinton et al., 2010; Zhang et al., 2004; Pimentel, 2006). Nutrients are in large concentrations present in clayey and silty soils and in soils with a high percentage of soil organic matter (SOM). As soil erosion removes first the small grain soil (clay, silt), nutrients are more prone to soil redistribution. This could promote nutrient limitation that can be difficult to compensate when the losses are large compared to gain fluxes. Potentially, this could result in productivity loss and on a longer term to a tipping point in the system where the vegetation cannot be restored to the previous productive state anymore (Zhang et al., 2004). High concentrations of dissolved nutrients in the water can also promote algal blooms and phytoplankton productivity that can have negative effects on the environment.

Beside physical removal of nutrients, soil erosion can also enhance mineralization of the nutrients by disruption of soil aggregates and the transport of these aggregates by overland flow, resulting in an increased availability of dissolved nutrients for biota (Balesdent et al., 2000; Quinton et al., 2010). On long-term this enhanced mineral-

ization can lead to a general depletion of organic nutrients. The depletion of organic nutrients in eroding sites can become a source in deposition areas where increased concentrations of nutrients can act as fertilizers.
In addition to these general effects of soil redistribution on the nutrient cycles, there are some effects that are dependent on the nutrient type. Nitrogen, for example, gets quickly taken up by biota or mineralized during sediment transport. Deposition of sediment containing nitrogen can therefore lead to an increased carbon to nitrogen ratio and thus resulting in the stabilization of the nitrogen in the soil. For the phosphorus cycle, removal by chemical weathering of exposed subsoil due to soil erosion can be equally important to the physical removal by soil erosion (Quinton et al., 2010; Filippelli, 2008). As all these processes act simultaneously, the net effect of soil redistribution on the biogeochemical cycles is difficult to estimate, however, the need for this estimate is urgent in order to better understand the effects of human activities in the future.

1.5 Thesis outline

The motivation of this study is to develop methods and tools to simulate long-term soil redistribution on a global scale using coarse resolution climate and land cover data. Having the tools to simulate soil distribution on a global scale would open the possibility to investigate its impact on the global biogeochemical cycles, and on the soil-vegetation-atmosphere interactions.
The main objective of this study is to derive long-term soil erosion rates and sediment fluxes on a global scale, and to investigate the effects of land use change and climate change on these sediment fluxes.
The aim of chapter 2 is to develop an erosion model in the framework of ESMs, to quantify global soil erosion rates for present day and for the last millennium. The particular research questions for this chapter are:

1. How can realistic global soil erosion rates be derived for present day, and what are the main uncertainties?

2. Can global soil erosion rates that are derived from observational datasets be reproduced with climate and land cover data from Earth System Models?

3. How did soil erosion change during the last millennium and what were the main drivers behind this change?

The first part of this chapter is published in the journal of Geoscientific Model Development (GMD).
The focus of chapter 3 is the newly developed global sediment budget model compatible with ESMs and building on the erosion model of chapter 2. The aim is to use

this model to quantify the change in global sediment storage and fluxes during the last millennium, with the following research questions being investigated:

1. How to simulate large-scale sediment storage and fluxes for the long-term (centennial to millennial timescales)?
2. How did sediment storage change during the last millennium and what were the main drivers behind this change?
3. How do catchment characteristics influence the change in sediment storage on the long-term?

Part of this chapter is under review for the journal Earth Surface Dynamics.
Chapter 4 is an outlook chapter on the significance of laterally displaced carbon and nutrients due to soil erosion. The aim is to point out the importance of studying the effects of soil redistribution on the biogeochemical cycles, and identify the main processes that should be modelled in order to quantify the overall effects on the biogeochemical cycles. The research questions here are:

1. How large are present-day lateral fluxes of carbon and nutrients due to soil erosion only?
2. How does soil redistribution impact these lateral fluxes of carbon and nutrients?
3. Which approach should be taken to quantify the main effects of soil redistribution on the carbon and nutrient cycles?

The content of this chapter will be used as a basis for developing the tools to relate soil redistribution to the carbon and nutrient cycles.
Chapter 5 provides the final summary and discussion of the results as well as the perspectives for future research on modelling sediment dynamics and biogeochemical cycles in ESMs.

1.6 Formal remarks

The studies presented in the next three chapters are conducted under supervision and guidance of Dr. Christian Reick and support of Prof.Dr. Kristof Van Oost, and others regarding data and technical solutions. In contrast to the introduction and the summary and conclusions, the next three chapters are therefore written in the first person plural. I kindly ask the reader to keep this is mind.

Chapter 2

Accelerated soil erosion - a global phenomenon[1]

2.1 Introduction

Currently, there exists a large uncertainty in the global soil erosion rates as can be seen from recent studies that show rates between 20 and 200 Pg year^{-1} (Doetterl et al., 2012). This indicates that modelling soil erosion on a global scale is still a difficult task due to the very high spatial and temporal variability of soil erosion. Different approaches were previously applied to estimate soil erosion on a large or global scale. Most of these approaches are based on extrapolated data from agricultural plots, sediment yield or extrapolated river sediment estimates (Milliman and Syvitski, 1992; Stallard, 1998; Lal, 2003; Pimentel et al., 1995; Hooke, 2000; Wilkinson and McElroy, 2007).
An alternative approach is based on the use of soil erosion models, in order to be able to predict soil erosion rates for the past and future. One of the most applied models to estimate soil erosion on a large spatial scale is the semi-empirical/process-based Revised Universal Soil Loss Equation (RUSLE) model (Renard et al., 1997). This model stems from the original Universal Soil Loss Equation (USLE) model developed by the USDA (USA Department of Agriculture), which is based on a large set of experiments on soil loss due to water erosion from agricultural plots in the USA. These experiments covered a large variety of agricultural practices, soil types and climatic conditions, making it a suitable tool on a regional to global scale. The RUSLE model predicts the average annual soil erosion rates by rainfall and is formulated as a product of a rainfall erosivity factor, soil erodibility factor, land cover factor, topographical factor, and a support practice factor. The RUSLE model was first applied on a global scale by Yang

[1]Part of this study has been published as a research paper in **Naipal, V.**, Reick, C., Pongratz, J., and Van Oost, K.: Improving the global applicability of the RUSLE model - adjustment of the topographical and rainfall erosivity factors, Geosci. Model Dev., 8, 28932913, doi:10.5194/gmd-8-2893-2015, 2015.

et al. (2003) and Ito (2007) for estimating the global soil erosion potential. Various limitations were observed when applying this model on global scale. Firstly, the model is originally developed to be applicable on the agricultural plot scale. This makes the model incompatible with the coarse spatial scale of global data sets on soil-erosion-influencing factors such as precipitation, elevation, land use and soil characteristics. Secondly, the RUSLE and USLE models were parameterized for environmental conditions of the USA and are thus not directly applicable to other areas in the world. Thirdly, only sheet and rill erosion are considered. Finally, the RUSLE model does not contain sediment deposition and sediment transport terms, which are closely linked to soil erosion.

However, the RUSLE model is to our knowledge one of the few erosion models that has the potential to be applied on a global scale due to its simple structure and empirical basis. Therefore, it is of key importance to address the above mentioned limitations first.

To address the first two limitations, Van Oost et al. (2007) presented in their work a modified version of the USLE model for application on agricultural areas on global scale. They based their model on large-scale experimental soil erosion data from the USA (National Resource Inventory, NRI, database of Agriculture (2000)) and Europe by deriving reference factors for soil erosion on agricultural land and for certain USLE parameters. They also introduced a procedure to scale slope, which is an important parameter in the topographical factor of the USLE/RUSLE model. In this scaling procedure slope was scaled from the GTOPO30 1 km resolution digital elevation model (Survey, 1996) to the coarser resolution of the erosion model. This method was based on high resolution OS (Ordnance Survey; 10 m resolution) and SRTM (Shuttle Radar Topography Mission) data on elevation (90 m resolution, International Centre for Tropical Agriculture, CIAT) for England and Wales.

Doetterl et al. (2012) showed that together with the topographical factor, the rainfall erosivity factor explain up to 75 % of the erosion variability across agricultural areas at the large watershed scale. These factors represent the triggers for soil erosion by providing energy for soil to erode. They can also be seen as the natural components of the RUSLE model, as they include very little or no modification by human activities (Angulo-Martinez et al., 2009) apart from indirect effects on precipitation and extreme events due to anthropogenic climate change. In this way they represent the natural environmental constraints to soil erosion that are important to capture before the effect of human activities on soil erosion through land use change can be investigated.

Previous studies on global soil erosion calculated the global rainall erosivity factor based on the total annual precipitation (Renard and Freimund, 1994). This method is different from the method presented in the original RUSLE model (Renard et al., 1997), which is mainly based on 30 min precipitation intensity. The reason for the method of Renard and Freimund (1994) is the lack of high resolution precipitation intensity on a global scale. However, high resolution precipitation intensity is an important explaining parameter of the rainfall erosivity factor and therefore, the applicability of

the method of Renard and Freimund (1994) is limited.
The main objective of this chapter is to extend the applicability of the RUSLE model to a coarse resolution at global scale, in order to make the model compatible with Earth System Models (ESMs). This would enable future studies on the effects of soil erosion for the past, current and future climate. To this end, we develop generally applicable methods that improve the estimation of slope and climatic factors from coarse resolution global data sets. These methods should not only be applicable across agricultural areas as in the studies of Van Oost et al. (2007) and Doetterl et al. (2012) but also across non-agricultural areas. We adjust the topographical factor to the coarse resolution of the global scale based on the scaling of slope according to the fractal method. The adjustment of the rainfall erosivity factor to the global scale is based on globally applicable regression equations. We derived these regression equations for different climate zones based on parameters for precipitation, elevation and the simple precipitation intensity. This approach is validated using several high resolution data sets on the rainfall erosivity factor. To investigate the effects of these adjustments to both factors on global soil erosion rates we use climate and land cover data from global observational datasets for present day. Also, a comparison of the modelled global soil erosion rates with independent estimates from high resolution and high precision data sets of Europe and the USA is performed.
Next, the performance of the adjusted RUSLE model is tested when coarse resolution data from various ESMs is used instead of observational datatsets. For this purpose, climate and land cover data from five selected ESMs of the Coupled Model Intercomparison Project Phase 5 (CMIP5) is used to estimate present-day erosion rates with the adjusted RUSLE model. These erosion rates are then compared with those derived from observational datasets and the resulting uncertainties are estimated.
Finally, the global trends in soil erosion and their drivers is investigated during the last millennium. Additionally, first estimations of uncertainties are provided when modelling soil erosion using coarse resolution data from ESMs on a millennial timescale. An overview of these uncertainties is important for the prediction of global soil erosion rates with ESMs.

2.2 Methods

2.2.1 The RUSLE model

This study uses a modified version of the RUSLE model (based on Renard et al. (1997)), which calculates mean annual soil loss rates by sheet and rill erosion according to the following equation

$$E = R * K * C * LS * P \tag{2.1}$$

where E is the average annual soil loss ($\mathrm{t\,ha^{-1}\,year^{-1}}$), R is the rainfall erosivity factor ($\mathrm{MJ\,mm\,ha^{-1}\,h^{-1}\,year^{-1}}$), K is the soil erodibility factor ($\mathrm{t\,ha\,h\,ha^{-1}\,MJ^{-1}\,mm^{-1}}$), C is the land cover factor (dimensionless), LS is the slope length and slope steepness factor (dimensionless), and P is the support practices factor (dimensionless).
The R factor is described by Hudson (1971) and Wischmeier and Smith (1978) as the result of the transfer of kinetic energy of raindrops to the soil surface. This causes a detachment of soil and the downslope transport of the soil particles, depending on the amount of energy, rainfall intensity, soil type and cover, topography and management (Da Silva, 2004). The original method of calculating erosivity is described by Wischmeier and Smith (1978) and Renard et al. (1997) as

$$R = \frac{1}{n} \sum_{j=1}^{n} \sum_{k=1}^{m_j} \left(\mathrm{EI}_{30}\right)_k , \tag{2.2}$$

where n is the number of years of records, m_j is the number of storms of a given year j, and EI_{30} is the rainfall erosivity index of a storm k. The event's rainfall erosivity index EI_{30} ($\mathrm{MJ\,mm\,ha^{-1}\,h^{-1}}$) is defined as

$$\mathrm{EI}_{30} = I_{30} \sum_{r=1}^{m} e_\mathrm{r} v_\mathrm{r}, \tag{2.3}$$

where e_r and v_r are, respectively, the unit rainfall energy ($\mathrm{MJ\,ha^{-1}\,mm^{-1}}$) and the rainfall depth (mm) during a time period r, and I_{30} is the maximum rainfall intensity during a time period of 30 min ($\mathrm{mm\,h^{-1}}$). The unit rainfall energy, e_r, is calculated for each time period as

$$e_\mathrm{r} = 0.29 \left(1 - 0.72 e^{-0.05 i_\mathrm{r}}\right) , \tag{2.4}$$

where i_r is the rainfall intensity during the time period ($\mathrm{mm\,h^{-1}}$).
The topographical factor of RUSLE, which is the LS factor, is composed of the slope length factor (L) and the slope steepness factor (S). The L factor is computed according to Renard et al. (1997) by the following equation

$$L = \left(\frac{l}{22.13}\right)^{m}, \tag{2.5}$$

where

$$m = \frac{F}{1+F} \quad \text{and} \quad F = \frac{(\sin\theta/0.0896)}{\left(3\left(\sin\theta\right)^{0.8}+0.56\right)}, \tag{2.6}$$

in which θ is the slope and l is the slope length in meters.
The S factor is generally computed by the continuous function of Nearing (1997)

$$S = 1.5 + \frac{17}{1+e^{(2.3-6.1*\sin\theta)}}. \tag{2.7}$$

The K factor is a lumped parameter that accounts for the reaction of the integrated annual soil profile to the process of soil detachment, and transport by raindrops and surface flow (Renard et al., 1997). The K factor can be calculated according the method of Torri et al. (1997), where K is a function of the texture, which is represented by the silt (f_{silt}), clay (f_{clay}) and sand (f_{sand}) fractions, and the organic matter content (OM in percent)

$$K = 0.0293(0.65 - Dg + 0.24Dg^2) * e^{(-0.0021\frac{OM}{f_{clay}} - 0.00037(\frac{OM}{f_{clay}})^2 - 4.02f_{clay} + 1.72f_{clay}^2)} \tag{2.8}$$

where Dg is defined as:

$$Dg = -3.5f_{sand} - 2f_{silt} - 0.5f_{clay} \tag{2.9}$$

The C factor is mainly determined by the vegetation and computed using biophysical attributes such as the vegetation cover density. In this study we use the Normalized Difference Vegetation Index ($NDVI$) to calculate the C factor according to the method of De Jong et al. (1998)

$$C = e^{\{-\alpha*\frac{NDVI}{\beta-NDVI}\}} \tag{2.10}$$

where the parameters α and β are set to respectively 2 and 1.

The P factor takes into account the effect of contouring, terracing, and subsurface drained areas (Renard et al., 1997).

2.2.2 Improving the global applicability of the RUSLE model

2.2.2.1 Adjustment of the topographical factor

As seen in Eqs. (2.6)–(2.7), slope is a crucial parameter and thus an accurate estimation is essential in deriving accurate estimates of the L and S factors and soil erosion rates. For an accurate estimation of the slope, input elevation data from digital elevation models (DEMs) should capture the detailed spatial variability in elevation. However, global DEMs are often too coarse to capture the detailed topography because of the surface smoothening effect. To account for this problem it is assumed that topography is fractal. Following Klinkenberg and Goodchild (1992) and Zhang et al. (1999), slope can be expressed as a function of the spatial scale by applying the variogram equation. The variogram equation is used to approximate the fractal dimension of topography and is expressed as follows:

$$(Z_p - Z_q)^2 = k d_{pq}^{4-2D}, \tag{2.11}$$

so that

$$\frac{|Z_p - Z_q|}{d_{pq}} = \alpha d_{pq}^{1-D}, \tag{2.12}$$

where Z_p and Z_q are the elevations at points p and q, d_{pq} is the distance between p and q, k is a constant, $\alpha = k^{0.5}$, and D is the fractal dimension. Because the left side of Eq. (2.12) represents the slope, it can be assumed that the slope (θ) is related to the spatial scale or the grid size (d) in

$$\theta = \alpha d^{1-D}. \tag{2.13}$$

This result implies that by calculating the fractal properties (D and α) Eq. (2.13) can be used to calculate slope at any specified d. The local fractal dimension (D) describes the roughness of the topography while the local value of α is related to the concept of lacunarity, which is a measure of the size of "gaps" (valleys and plains) in the topography (Zhang et al., 2002). To estimate the spatial variations of D and α, Zhang et al. (1999) proposed to relate these parameters to the standard deviation of elevation. Hereby it is assumed that the standard deviation of elevation does not change much with the DEM resolution. D is then calculated as a function of the standard deviation (σ) in a $3\,\text{pixel} \times 3\,\text{pixel}$ moving window, as proposed by Zhang et al. (1999):

$$D = 1.13589 + 0.08452 \ln \sigma. \tag{2.14}$$

To estimate α we used the modified approach by Pradhan et al. (2006). They derived α directly from the steepest slope in a $3\,\text{pixel} \times 3\,\text{pixel}$ moving window, called α_{steepest} in the following. Having obtained α_{steepest} and D from a grid at a given resolution, the scaled slope (θ_{scaled}) for a target grid resolution (d_{scaled}) is obtained by

$$\theta_{\text{scaled}} = \alpha_{\text{steepest}} d_{\text{scaled}}^{1-D}. \tag{2.15}$$

Pradhan et al. (2006) also showed that in their case study the ideal target resolution for downscaling slope was 150 m. This is due to the breakdown of the unifractal concept at very fine scales, which was shown to happen at a scale of 50 m. Altogether, this fractal method shows that a high resolution slope can be obtained from a low resolution DEM as is needed by the RUSLE model.
In this study, we investigate the performance of the fractal method on a global scale using different global DEMs as a starting point. The target resolution of downscaling is put to 150 m (about 5 arcsec) according to Pradhan et al. (2006). It should be noted that the spatial scale on which the original RUSLE and USLE models are operating is usually between 10 and 100 m, which indicates that the 150 m target resolution may be still too coarse for a correct representation of slope. The DEMs that are used here are given in Appendix A.1.

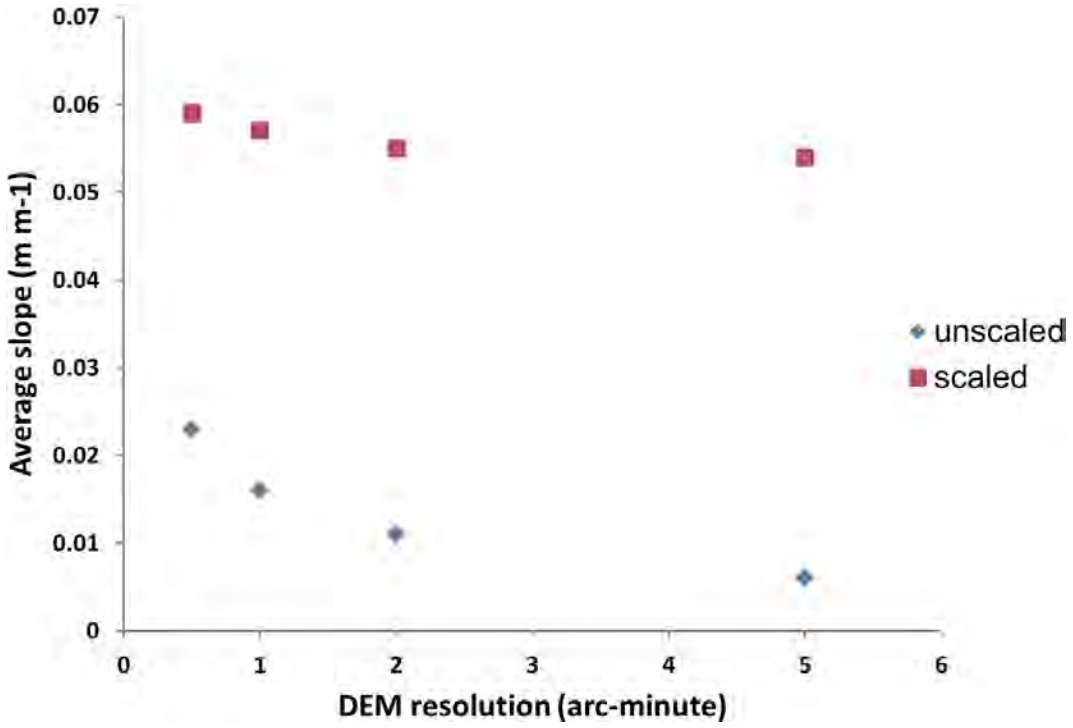

Figure 2.1: Global average unscaled slope estimated from different coarse resolution digital elevation models (DEMs) as function of their resolution (blue), and global average scaled slope from the same DEMs as function of their resolution (red).

As reported in previous studies (Zhang et al., 1999; Chang and Tsai, 1991; Zhang and Montgomery, 1994), the average slope decreases with decreasing DEM resolution. This confirms the expectation of loss of detail in topography at lower DEM resolutions. A large difference is found between the unscaled global average slope from the 5 arcmin and the 30 arcsec DEMs, which is in the order of $0.017\,\mathrm{m\,m^{-1}}$ or 74 % (Table 2.1). After applying the fractal method, the scaled slopes at 150 m target resolution from all DEMs increased significantly compared to the unscaled slopes (Fig. 2.1). However, there is still a difference of about $0.05\,\mathrm{m\,m^{-1}}$ or 8.5 % between the scaled slopes from

Table 2.1: Fractal parameters and the resulting mean global slopes before and after applying the fractal method on the different DEMs. Increase of slope means the increase of the average global slope of a DEM after applying the fractal method; difference after scaling = $\frac{\theta_{\text{scaled(DEM)}} - \theta_{\text{scaled(GTOPO30)}}}{\theta_{\text{scaled(GTOPO30)}}} * 100$; difference before scaling = $\frac{\theta_{\text{(DEM)}} - \theta_{\text{(GTOPO30)}}}{\theta_{\text{(GTOPO30)}}} * 100$.

DEM	Resolution	Standard deviation of elevation	Mean D	Mean α_{steepest}	θ	θ_{scaled}	Increase of θ	Difference after scaling	Difference before scaling
	arcmin	m			m m^{-1}	m m^{-1}	%	%	%
GTOPO30	0.5	570	1.32	0.99	0.023	0.059	61	0	0
ETOPO1	1	530	1.35	1.08	0.016	0.057	71.9	−3.4	−30.4
ETOPO2	2	549	1.37	1.17	0.011	0.055	80	−6.8	−52.2
ETOPO5	5	562	1.42	1.25	0.006	0.054	88.9	−8.5	−73.9

the 5 arcmin and the 30 arcsec DEMs (Table 2.1). This difference can be attributed to several factors. One factor could be the underlying assumption that the standard deviation of elevation (σ) is independent of the DEM resolution. Although σ does not change much when considering different resolutions, there is still a general decrease in mean global σ when going from the 5 arcmin to the 30 arcsec DEM (Table 2.1). Due to the dependence of the fractal dimension (D) on σ (Zhang et al., 1999), a decrease of σ leads to a decrease in D and therefore an increase in the scaled slope. Other factors that could play a role here are the dependence of α_{steepest} on the steepest slope, and the breakdown of the fractal method at certain scales and in certain environments. Zhang et al. (1999) mentioned that the scaling properties of slope are affected in very coarse resolution DEMs if σ changes considerably. On the other hand, Pradhan et al. (2006) mentioned the breakdown of the fractal method at very fine scales. This can indicate that the 150 m target resolution is not appropriate for some topographically complex regions in the world or, as addressed by Zhang et al. (1999), the DEMs used in this study are too coarse to scale down the slope to 150 m accurately for these regions.
After applying the fractal method on a 30 arcsec resolution DEM, the scaled slope shows a clear increase in detail, while the unscaled slope shows a strong smoothening effect (Fig. 2.2a, b). It is found that, after scaling, the slope values range from 0 to 85 degree and are less than 2 degree in 80% of the area. In contrast, all slope values are less than 45 degree and range between 0 and 2 degree in 89% of this area when slope is computed directly from the 30 arcsec DEM. The scaled slope from the 30 arc-second DEM will be used in this study to estimate the global soil erosion rates by the RUSLE model.

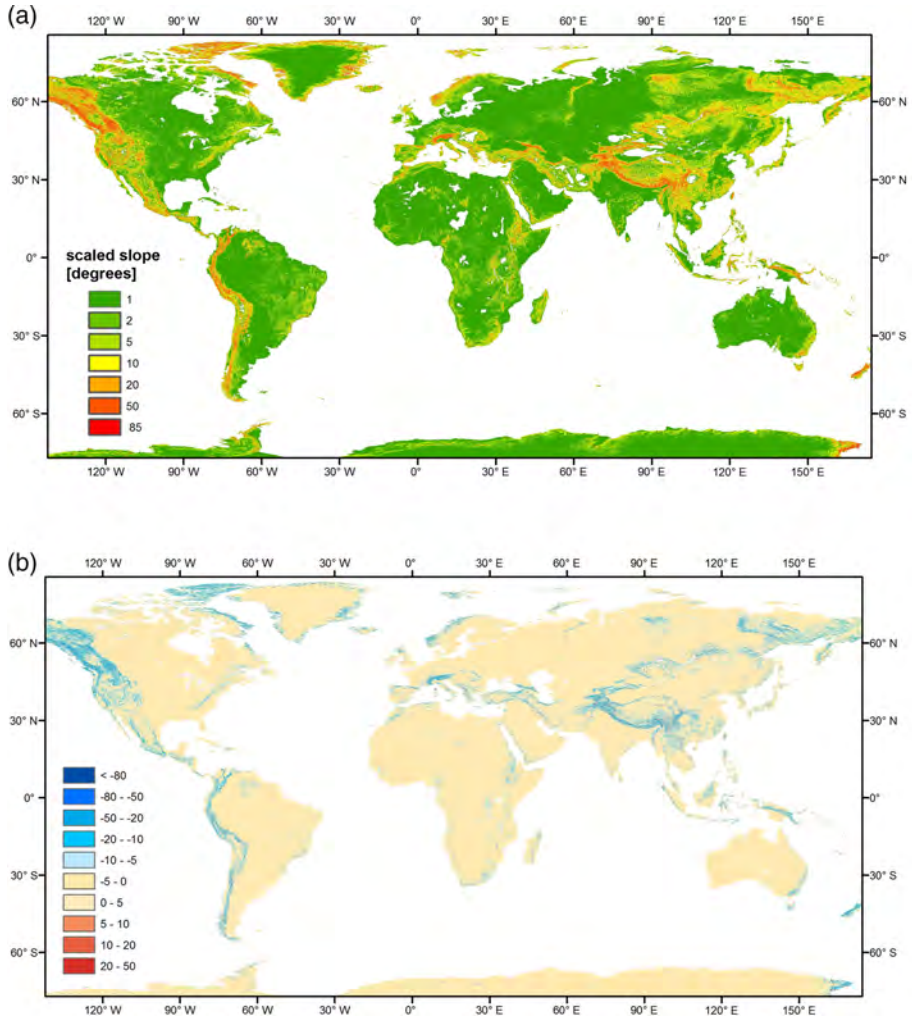

Figure 2.2: **(a)** A global map of the scaled slope derived from the 30 arcsec DEM using a target resolution of 150 m. **(b)** A global map showing the difference between the unscaled and scaled slopes (in degrees), where bluish colours show an underestimation by the unscaled slope when compared to the scaled slope and reddish colours show and overestimation.

2.2.2.2 Adjustment of the rainfall erosivity factor

The information needed to calculate the R factor according to the method of Wischmeier and Smith (1978) is difficult to obtain on a large spatial scale or in remote areas. Therefore, different studies have been done on deriving regression equations for the R factor (Angulo-Martinez et al., 2009; Meusburger et al., 2012; Goovaerts, 1999; Diodato and Bellocchi, 2010). Most of these studies, however, concentrate on a specific area and can therefore not be implemented on the global scale. Studies on global soil erosion estimation by the RUSLE model or a modified version of it (Doetterl et al., 2012; Van Oost et al., 2007; Montgomery, 2007; Yang et al., 2003) have all used the method of Renard and Freimund (1994). Renard and Freimund (1994) related the R factor to the total annual precipitation (P, mm) based on erosivity data available for 155 stations in the USA, shown in the following equations

$$\begin{aligned} R &= 0.0483P^{1.61}, \quad P \leq 850\,\text{mm} \\ R &= 587.8 - 1.219P + 0.004105P^2, \quad P \geq 850\,\text{mm}. \end{aligned} \tag{2.16}$$

To test how this method performs globally, we calculated the R factor according to the method of Renard and Freimund (1994) (Eq. 2.16) first. Here we used the 0.25 degree resolution annual precipitation data from the Global Precipitation Climatology Centre (GPCC) product (in Appendix A.1). Then, we selected three regions to validate the resulting R values and their variability: the USA United States Environmental Protection Agency (2001), Switzerland (Meusburger et al., 2012), and the Ebro Basin in Spain (Angulo-Martinez et al., 2009). For these regions, high resolution erosivity data are available from pluviographic data of local meteorological stations across the whole region.

Figure 2.3 shows that the R values computed with the Renard and Freimund (1994) method strongly overestimate R when compared to the high resolution R data of the selected regions. For the USA the R factor of Renard and Freimund (1994) shows an overall overestimation for the western USA and for a large part of the eastern USA when compared to the high resolution R factor (Table 2.5, Fig. 2.3a). In particular, a strong overestimation is seen for the north-west coast of the USA. This region is known to have complex rainfall patterns due to the presence of mountains and high local precipitation intensities with frequent snow fall (Cooper, 2011). It should be noted that the USA is not the best suited case study for testing the R values computed with the Renard and Freimund (1994) method, as this method is based on climate data from stations in the USA. The available high resolution or observed data on the R factor from Switzerland and the Ebro Basin are better suited for an independent validation. For Switzerland, which has a complex precipitation variability influenced by the relief of the Alps (Meusburger et al., 2012), the R factor of Renard and Freimund (1994) shows a strong overall overestimation when compared to the high resolution R values (Table 2.5, Fig. 2.3b). For the Ebro Basin, located in Spain, the observed R data were available for the period 1997–2006 from Angulo-Martinez et al. (2009). Also here the method of Renard and Freimund (1994) overestimates the R factor and is not able to reproduce the high spatial variability of the R data (Table 2.5, Fig. 2.3c).
To better represent the R factor on a global scale, the R estimation was based on the updated Köppen–Geiger climate classification (Table 2.2, Fig. 2.4). The Köppen–Geiger climate classification is a global climate classification and is based on the vegetation distribution connected to annual cycles of precipitation and temperature (Lohmann et al., 1993). The reason for this approach is that this classification system includes annual cycles of precipitation and is thus indirectly related to precipitation intensity. Based on this, it is possible to derive regression equations for the R factor that are applicable for each individual climate zone of the classification. This provides a basis to calculate the R factor with coarse resolution data on a global scale.

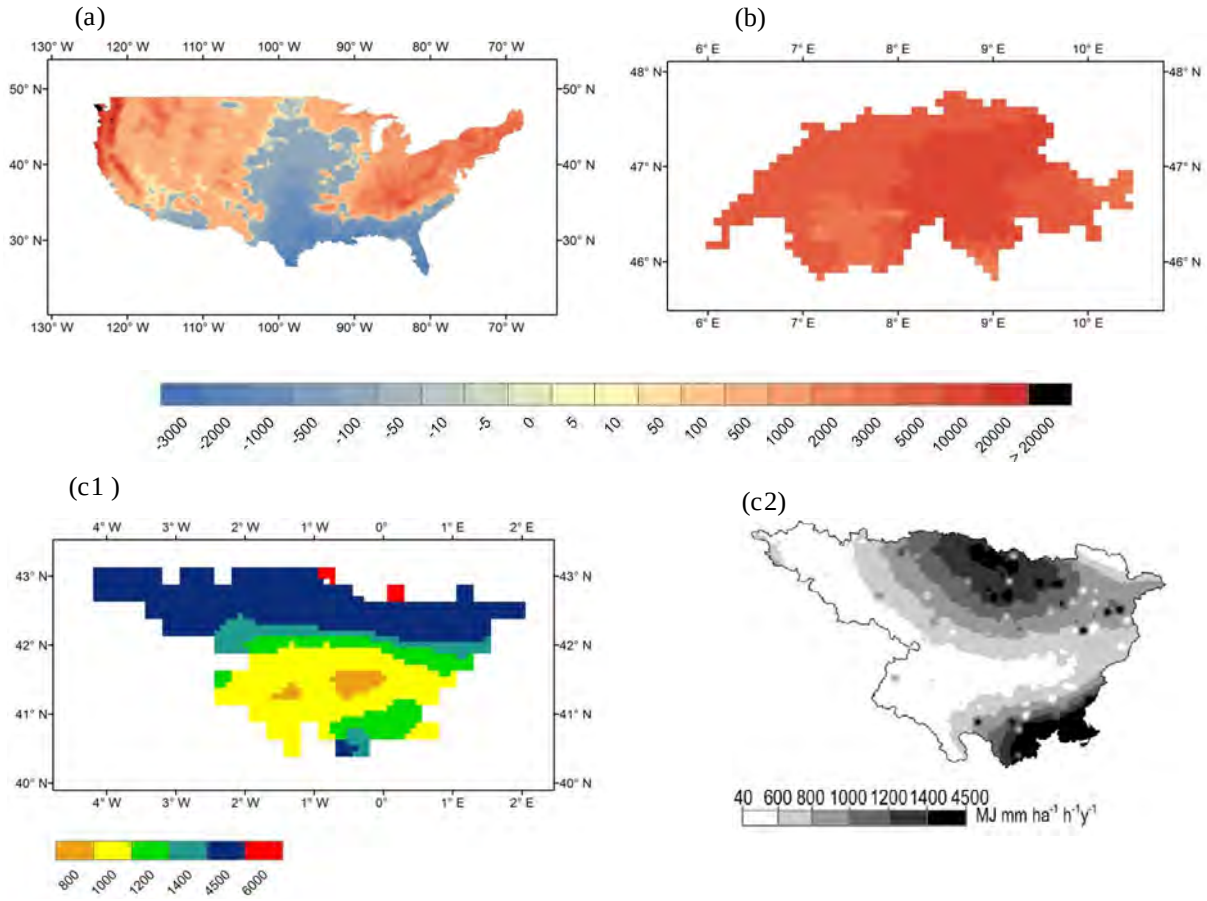

Figure 2.3: Spatial difference plots showing the difference between the high resolution R values and R values calculated with the method of Renard and Freimund (1994) for **(a)** the USA, **(b)** Switzerland and **(c)** the Ebro Basin in Spain; in panels **(a)** and **(b)** the blue colours show an underestimation of the calculated R factor when compared to the high resolution R values, while the red colours show an overestimation; the Ebro Basin serves here as an independent validation set and it has two graphs: **(c1)** a spatial plot of erosivity according to Renard and Freimund (1994) and **(c2)** the high resolution R values from Angulo-Martinez et al. (2009) (all values in the graphs are in MJ mm ha^{-1} h^{-1} year^{-1}).

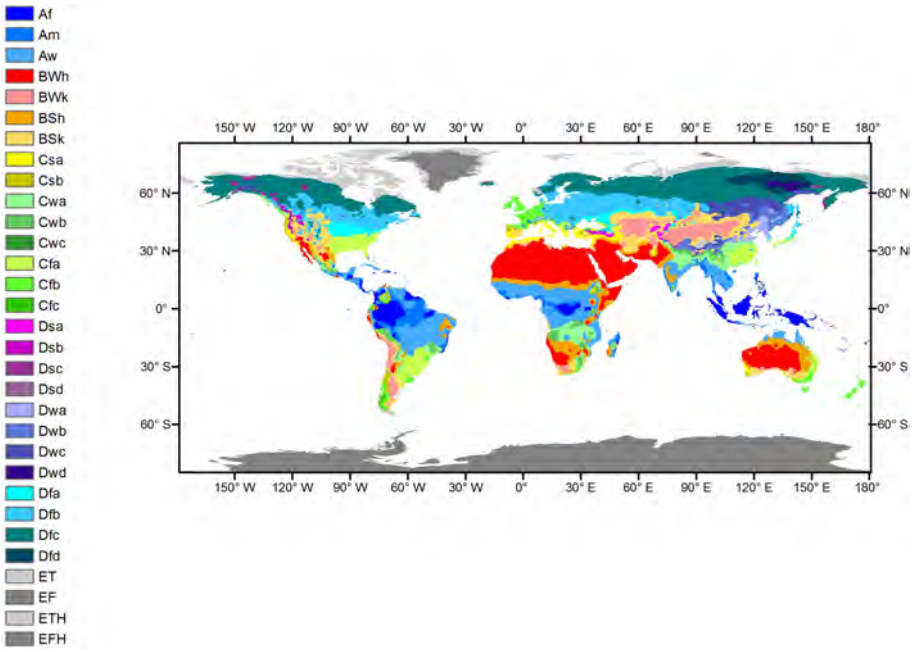

Figure 2.4: The Köppen–Geiger climate classification global map at a resolution of 5 arcmin (Peel et al., 2007).

Table 2.2: Description of Köppen climate symbols and defining criteria (from Peel et al. (2007).

First	Second	Third	Description	Criteria*
A			Tropical	$T_{cold} \geq 18$
	f		– rainforest	$P_{dry} \geq 60$
	m		– monsoon	Not (Af) & $P_{dry} \geq 100–MAP/25$
	w		– savannah	Not (Af) & $P_{dry} < 100–MAP/25$
B			Arid	$MAP < 10P_{threshold}$
	W		– desert	$MAP < 5P_{threshold}$
	S		– steppe	$MAP \geq 5P_{threshold}$
		h	– hot	$MAT \geq 18$
		k	– cold	$MAT < 18$
C			Temperate	$T_{hot} > 10$ & $0 < T_{cold} < 18$
	s		– dry summer	$P_{sdry} < 40$ & $P_{sdry} < P_{wwet}/3$
	w		– dry winter	$P_{wdry} < P_{swet}/10$
	f		– without dry season	Not (Cs) or (Cw)
		a	– hot summer	$T_{hot} \geq 22$
		b	– warm summer	Not (a) & $T_{mon10} \geq 4$
		c	– cold summer	Not (a or b) & $1 \leq T_{mon10} < 4$
D			Cold	$T_{hot} > 10$ & $T_{cold} \leq 0$
	s		– dry summer	$P_{sdry} < 40$ & $P_{sdry} < P_{wwet}/3$
	w		– dry winter	$P_{wdry} < P_{swet}/10$
	f		– without dry season	Not (Ds) or (Dw)
		a	– hot summer	$T_{hot} \geq 22$
		a	– warm summer	Not (a) & $T_{mon10} \geq 4$
		c	– cold summer	Not (a, b or d)
		d	– very cold winter	Not (a or b) & $T_{cold} \leq -38$
E			Polar	$T_{hot} < 10$
	T		– tundra	$T_{hot} > 0$
	F		– frost	$T_{hot} < -0$

* MAP: mean annual precipitation, MAT: mean annualtemperature, T_{hot}: temperature of the hottest month,T_{cold}: temperature of the coldest month, T_{mon10}: number of months where thetemperature is above 10, P_{dry}: precipitation of the driest month,P_{sdry}: precipitation of the driest month in summer, P_{wdry}: precipitation of the driest month in winter, P_{swet}: precipitation of the wettest month in summer, P_{wwet}: precipitation of the wettest month in winter, $P_{threshold}$: varies according to the following rules (if 70 % of MAP occurs in winter then $P_{threshold} = 2\,MAT$, if 70 % of MAP occurs in summer then $P_{threshold} = 2\,MAT + 28$, otherwise $P_{threshold} = 2\,MAT + 14$). Summer (winter) is defined as the warmer (cooler) 6-month period of AMJJAS (ONDJFM).

As a basis for deriving the regression equations for the R factor we used high resolution R maps of the USA from the United States Environmental Protection Agency (2001). The USA covers most of the world's climate zones and is also the largest region with available high resolution R data. Linear multiple regression was used to adjust R:

$$\log(R_i) = \beta_0 + \sum_{j=1}^{n} \beta_{i_j} \log\left(X_{i_j}\right) + \varepsilon_i,$$
$$\text{for } i = 1, 2, \ldots, n, \tag{2.17}$$

where X is the independent explanatory variable, j is the number of explanatory variables, β is a constant and ε is the residual.

The regression operates on one or more of the following parameters (X_j): total annual precipitation (GPCC 0.25 degree product), mean elevation (ETOPO 5 DEM), and the simple precipitation intensity index, SDII. It should be mentioned that the SDII was only available on a very coarse resolution of 2.5 degree for certain regions on Earth, such as parts of Europe and the USA. The SDII is calculated as the daily precipitation amount on wet days (≥ 1 mm) in a certain time period divided by the number of wet days in that period. Previous studies that performed regression of R showed that precipitation and elevation were in most cases the only explanatory variables (Meusburger et al., 2012; Mikhailova et al., 1997; Goovaerts, 1999; Diodato and Bellocchi, 2010; Angulo-Martinez et al., 2009). Here, we added to the regression the SDII as it is a simple representation of precipitation intensity, which is an important explaining variable of the R factor. The precipitation and SDII data sets were rescaled to a 5 arcmin resolution (corresponding to 0.0833 degree) to match the Köppen–Geiger climate classification data that was available at the resolution of 6 arcmin (corresponding to 0.1 degree).

Furthermore, high resolution erosivity data from Switzerland (Meusburger et al., 2012) and annual precipitation from the GPCC 0.5 degree product were used to derive the regression equations for the R factor for the polar (E) climate zones. These climate zones are not present in the USA. For the rest of the climate zones that are not present in the USA it was difficult to obtain high resolution erosivity data. Therefore, we maintained the method of Renard and Freimund (1994) for those climate zones to calculate erosivity.

Also, we kept the R factor of the Renard and Freimund (1994) method if no clear improvement of the R factor was found when using the new regression equations for a specific climate zone. Here, we mainly used the r^2 combined with the residual standard error to evaluate if the new regression equations showed a clear improvement in the R factor. The Renard and Freimund (1994) R factors where kept for the hot arid climate zone (BWh) and the temperate climate zone with a hot summer (Csa) in the USA. These are just two climate zones out of the 17 evaluated ones, which show that the Renard and Freimund method performs as good as or slightly better than the regression method. All data sets for deriving the R factor are described in Appendix A.1.

Table 2.3: Linear multiple regression equations for different climate zones, relating high resolution R factor from the USA with one or more significant parameters: annual total mean precipitation, P (mm), mean elevation, z (m), and the simple precipitation intensity index, SDII (mm day^{-1}).

Climate zone	Explaining parameters	Regression function – optimal	R^2	Residual standard error
BWk	P, SDII	$R = 0.809P^{0.957} + 0.000189\text{SDII}^{6.285}$		
BSh	P, SDII	$\log R = -7.72 + 1.595 \log P + 2.068 \log \text{SDII}$	0.97	0.22
BSk	P, SDII, Z	$\log R = 0.0793 + 0.887 \log P + 1.892 \log \text{SDII} - 0.429 \log Z$	0.89	0.35
Csb	P	$R = 98.35 + 0.000355P^{1.987}$		0.16
Cfa	P, SDII, Z	$\log R = 0.524 + 0.462 \log P + 1.97 \log \text{SDII} - 0.106 \log Z$	0.89	0.11
Cfb	P, SDII	$\log R = 4.853 + 0.676 \log P + 3.34 \log \text{SDII}$	0.97	0.21
Dsa	Z, SDII	$\log R = 8.602 - 0.963 \log \text{SDII} - 0.247 \log Z$	0.51	0.05
Dsb	P	$\log R = 2.166 + 0.494 \log P$	0.45	0.25
Dsc	SDII	$\log R = 6.236 - 0.869 \log \text{SDII}$	0.51	0.02
Dwa	P	$\log R = -0.572 + 1.238 \log P$	0.99	0.02
Dwb	P, SDII	$\log R = -1.7 + 0.788 \log P + 1.824 \log \text{SDII}$	0.98	0.02
Dfa	P, SDII	$\log R = -1.99 + 0.737 \log P + 2.033 \log \text{SDII}$	0.9	0.16
Dfb	P, SDII, Z	$\log R = -0.5 + 0.266 \log P + 3.1 \log \text{SDII} - 0.131 \log Z$	0.89	0.32
Dfc	SDII	$\log R = -1.259 + 3.862 \log \text{SDII}$	0.91	0.23
ET	P	$\log R = -3.945 + 1.54 \log P$	0.14	0.42
EF + EFH	P	$\log R = 16.39 - 1.286 \log P$	0.6	0.13
ETH	P, SDII	$\log R = 21.44 + 1.293 \log P - 10.579 \log \text{SDII}$	0.52	0.53

Table 2.4: Linear multiple regression equations for different climate zones for regions that have no data on the simple precipitation intensity index, SDII (mm day^{-1}). The regression equations relate high resolution erosivity from the USA to the annual total mean precipitation, P (mm), and/or the mean elevation, z (m).

Climate zone	Optimal regression function (when SDII is not available)	R^2	Residual standard error
BWk	Method Renard and Freimund (1994)		
BSh	$\log R = -8.164 + 2.455 \log P$	0.86	0.5
BSk	$\log R = 5.52 + 1.33 \log P - 0.977 \log Z$	0.76	0.52
Cfa	$\log R = 3.378 + 0.852 \log P - 0.191 \log Z$	0.57	0.23
Cfb	$\log R = 5.267 + 0.839 \log P - 0.635 \log Z$	0.81	0.5
Dsa	$\log R = 7.49 - 0.0512 \log P - 0.272 \log Z$	0.48	0.06
Dsc	$\log R = 4.416 - 0.0594 \log P$	0.015	0.03
Dwb	$\log R = 1.882 + 0.819 \log P$	0.81	0.08
Dfa	$\log R = -2.396 + 1.5 \log P$	0.65	0.29
Dfb	$\log R = 1.96 + 1.084 \log P - 0.34 \log Z$	0.74	0.48
Dfc	$\log R = -3.263 + 1.576 \log P$	0.56	0.49
ETH	$\log R = -10.66 + 2.43 \log P$	0.4	0.59

Tables 2.3 and 2.4 show the resulting regression equations for climate zones for which we found initially a low correlation between the R values calculated by the method of Renard and Freimund (1994) and the high resolution R values from the United States Environmental Protection Agency (2001) and Meusburger et al. (2012). Figure 2.5 shows for each addressed climate zone how the method of Renard and Freimund (1994) and the new regression equations compare to the high resolution R of the USA. For the cold climate zones with a dry summer (Ds), the new regression equations show only a slight improvement as compared to the method of Renard and Freimund (1994). Also for the polar climate zones (E) the new regression equations still show a significant bias. However, they perform much better compared to the method of Renard and Freimund (1994). For most of the addressed climate zones the SDII explains a large part of the variability in the R factor. The elevation plays a smaller role here. Elevation can be an important explaining variable in regions with a high elevation variability, which then affects the precipitation intensity.
From tables 2.3 and 2.6 it can be concluded that the R factor in climate zones without a dry season (f) can be easily explained by the total annual precipitation and the SDII. Dry climate zones, especially dry summer climate zones, showed a weaker correlation. This is most likely due to the fact that the SDII is too coarse to explain the variability in the low precipitation intensity in the summer. It is also interesting to see that even though the SDII was derived from a very coarse resolution data set, it turned out to be still important for deriving more accurate R values.
We also show for each addressed climate zone a comparison of the newly computed average R factor with the average high resolution R factor, and the uncertainty range (Table 2.6). The uncertainty range was computed by taking into account the standard deviation of each of the parameters in the regression equations. As mentioned before, the polar climate zones showed the largest uncertainty range.
The new regression equations significantly improved the R values and spatial variability in the western USA and lead to an average R factor that was closer to the data mean (Table 2.5, Fig. 2.6a). Although the new regression equations show a bias for the polar climate zones (the minimum and maximum R values are not captured), the resulting mean R values for Switzerland show a strong improvement (Table 2.5, Fig. 2.6b).
Furthermore, the variability in the estimated R factor compares well with the variability of the high resolution R factor. It should be noted that Switzerland is not an independent case study for the polar climate zones, as the high resolution R values from this case study were used in our regression analysis. However, the Ebro Basin case study confirms the strong improvement for the polar climate zones (Fig. 2.6c). As the high resolution R values of the USA and Switzerland were used to derive the regression equations, the third case study, the Ebro Basin in Spain, provided an important independent validation. For the Ebro Basin, the new regression equations not only improve the overall mean but also capture the minimum R values better. This resulted in an improved representation of the R variability (Table 2.5, Fig. 2.6c). In Fig. 2.6c, however, there is a clear pattern separation in the newly computed R values,

which is due to the fact that the SDII data are not available for part of the Ebro Basin.

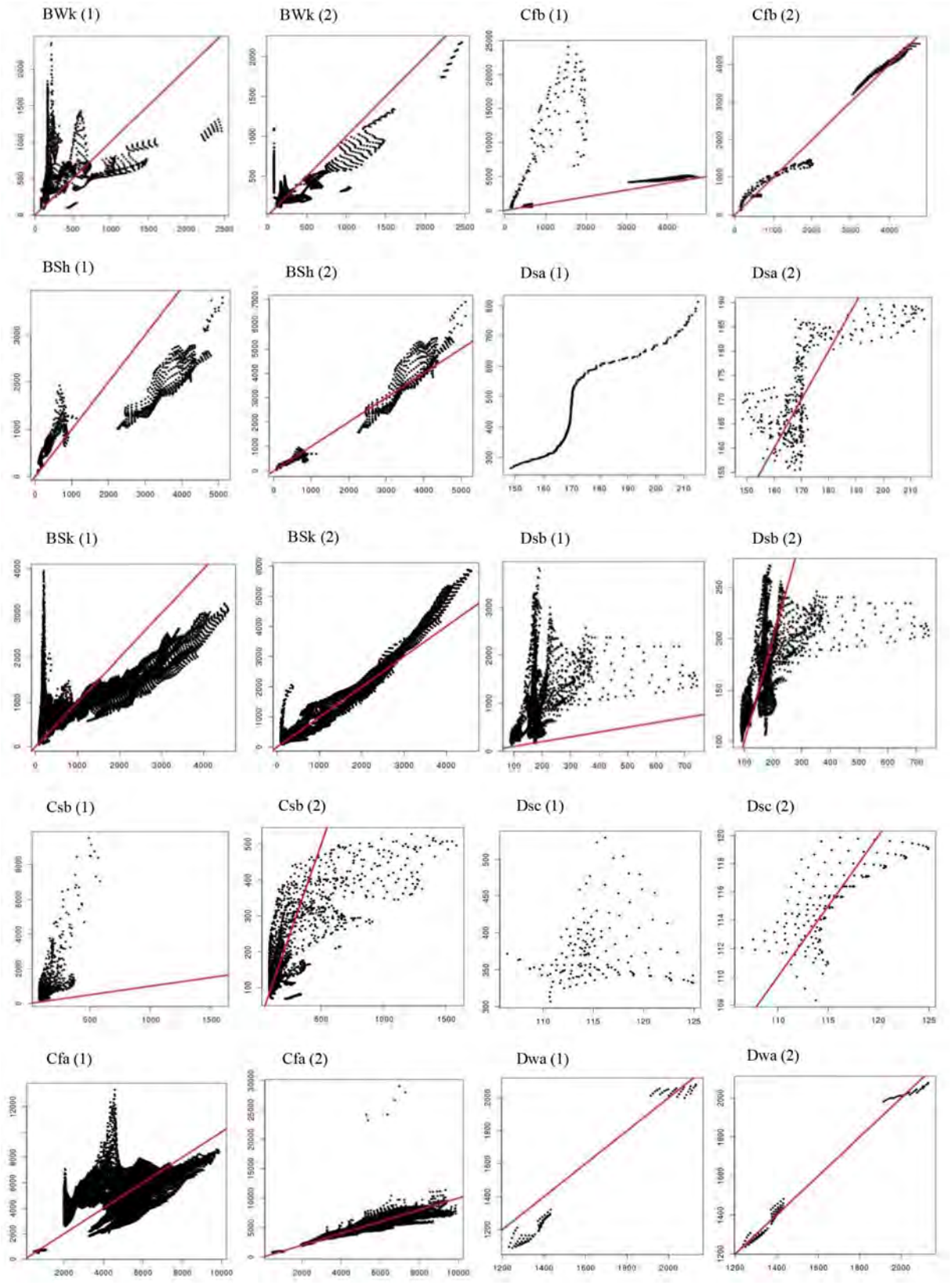

Figure 2.5:

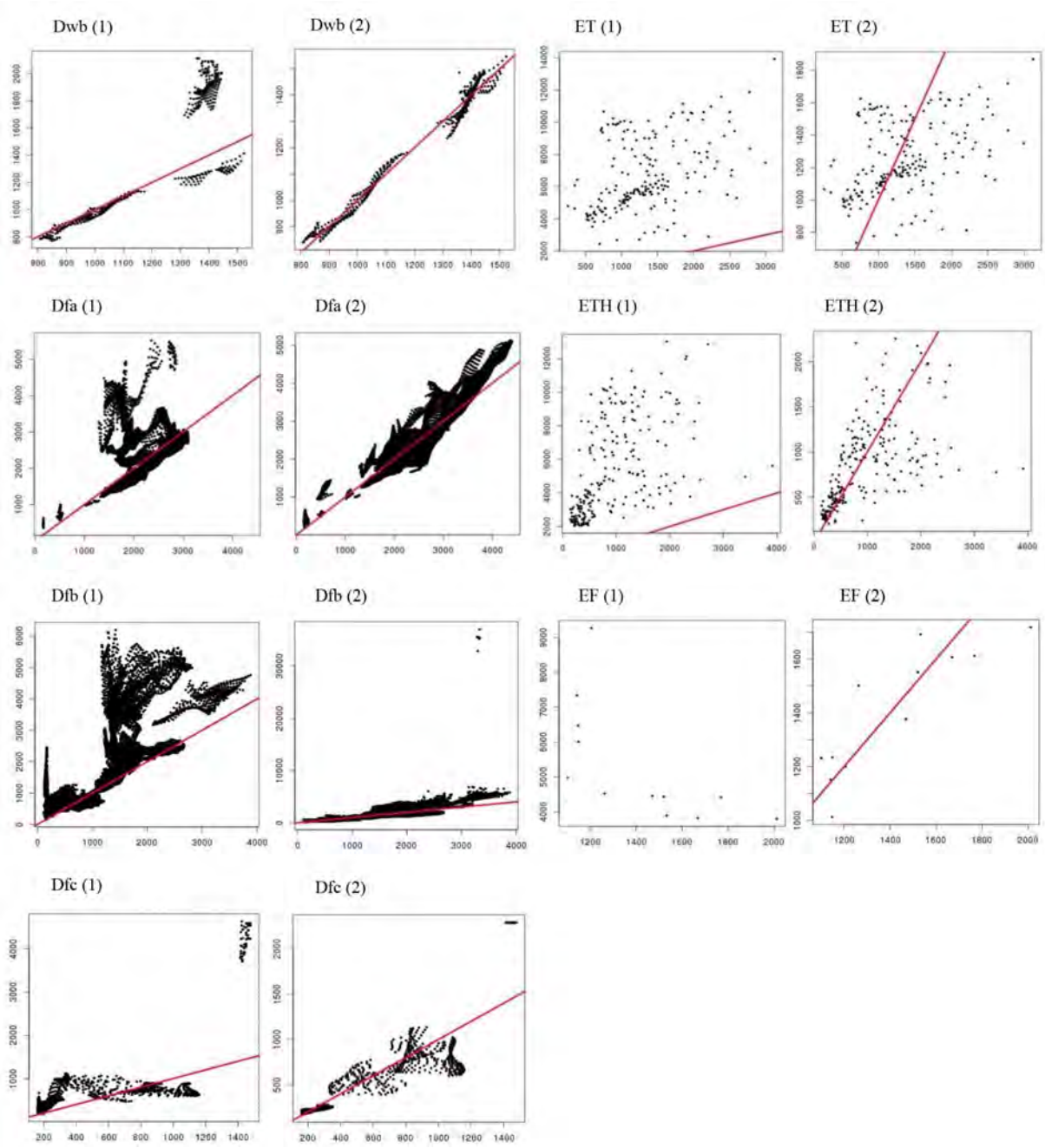

Figure 2.5: Comparison of high resolution R factor data and predicted R values from (1) the Renard and Freimund (1994) method and (2) the new regression equations, for various climate zones; the red line is the 1-to-1 line and does not appear in some graphs because predicted R values are overestimated.

As mentioned before, SDII is an important explaining parameter in the regression equations for most of the addressed climate zones.
Figure 2.7a shows the global patterns of the estimated R factor with the new regression equations. Figure 2.7b shows a difference plot between the estimated R factor with the method of Renard and Freimund (1994) and the R factor estimated with the new regression equations.

Table 2.5: Statistics of the comparison of high resolution R values ($\mathrm{MJ\,mm\,ha^{-1}\,h^{-1}\,year^{-1}}$) from three regions to estimated R values from the Renard and Freimund (1994) method and the new regression equations.

	Observed			Estimated – Renard and Freimund					Estimated – multiple linear regression				
	Range	Mean	Standard deviation	Range	Mean	Standard deviation	Correlation coefficient	Rank correlation coefficient	Range	Mean	Standard deviation	Correlation coefficient	Rank correlation coefficient
Switzerland	121–6500	1204	833	2335–10 131	5798	1654	0.51	0.42	225–2572	1256	472	0.49	0.3
USA (aggregated huc4)	105–4963	1271	1174	57–15 183	1870	2088	0.51	0.68	60–15 808	1691	2188	0.58	0.83
Ebro Basin	40–4500	891	622	747–5910	1529	846	–	–	167–4993	836	701	–	–

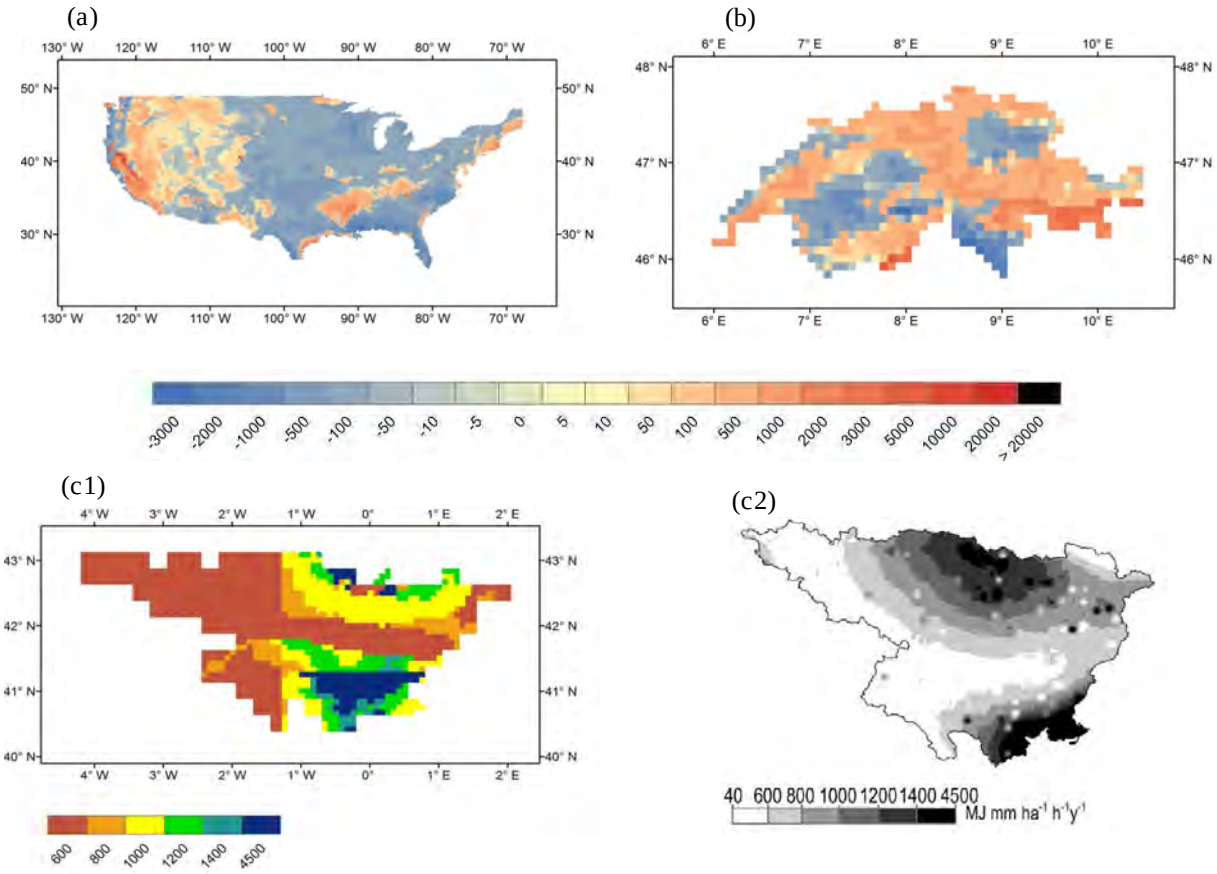

Figure 2.6: Spatial difference plots showing the difference between the high resolution R values and R values calculated with the new regression equations for **(a)** the USA, **(b)** Switzerland and **(c)** the Ebro Basin in Spain; in panels **(a)** and **(b)** the blue colours show an underestimation of the calculated R values when compared to the high resolution R values, while the red colours show an overestimation; the Ebro Basin serves here as an independent validation set and it has two graphs: **(c1)** a spatial plot of the R factor according to the new regression equations, and **(c2)** the high resolution R values from Angulo-Martinez et al. (2009) (all values in the graphs are in $\mathrm{MJ\,mm\,ha^{-1}\,h^{-1}\,year^{-1}}$).

The new regression equations significantly reduced the R values in most regions. However, the tropical regions still show unrealistic high R values (maximum R values go up to $1 \times 10^5\,\mathrm{MJ\,mm\,ha^{-1}\,h^{-1}\,year^{-1}}$). This is because the R factor was not adjusted for the tropical climate zones due to the lack of high resolution R data. Oliveira et al. (2013) found for the R factor in Brazil that the maximum R values for the tropical climate zones reach $22\,452\,\mathrm{MJ\,mm\,ha^{-1}\,h^{-1}\,year^{-1}}$. We find R values in Brazil that exceed this maximum R value found by Oliveira et al. (2013).
Finally, it should be noted that the purpose of the adjusting methods for the S and R factors in this study is to capture more accurately the large-scale mean erosion rates rather than the extremes. Therefore, even though the new regression equations are still not accurate enough for certain climate zones, it is important that the average R factor is represented well. The approach for adjusting the R factor also showed that although

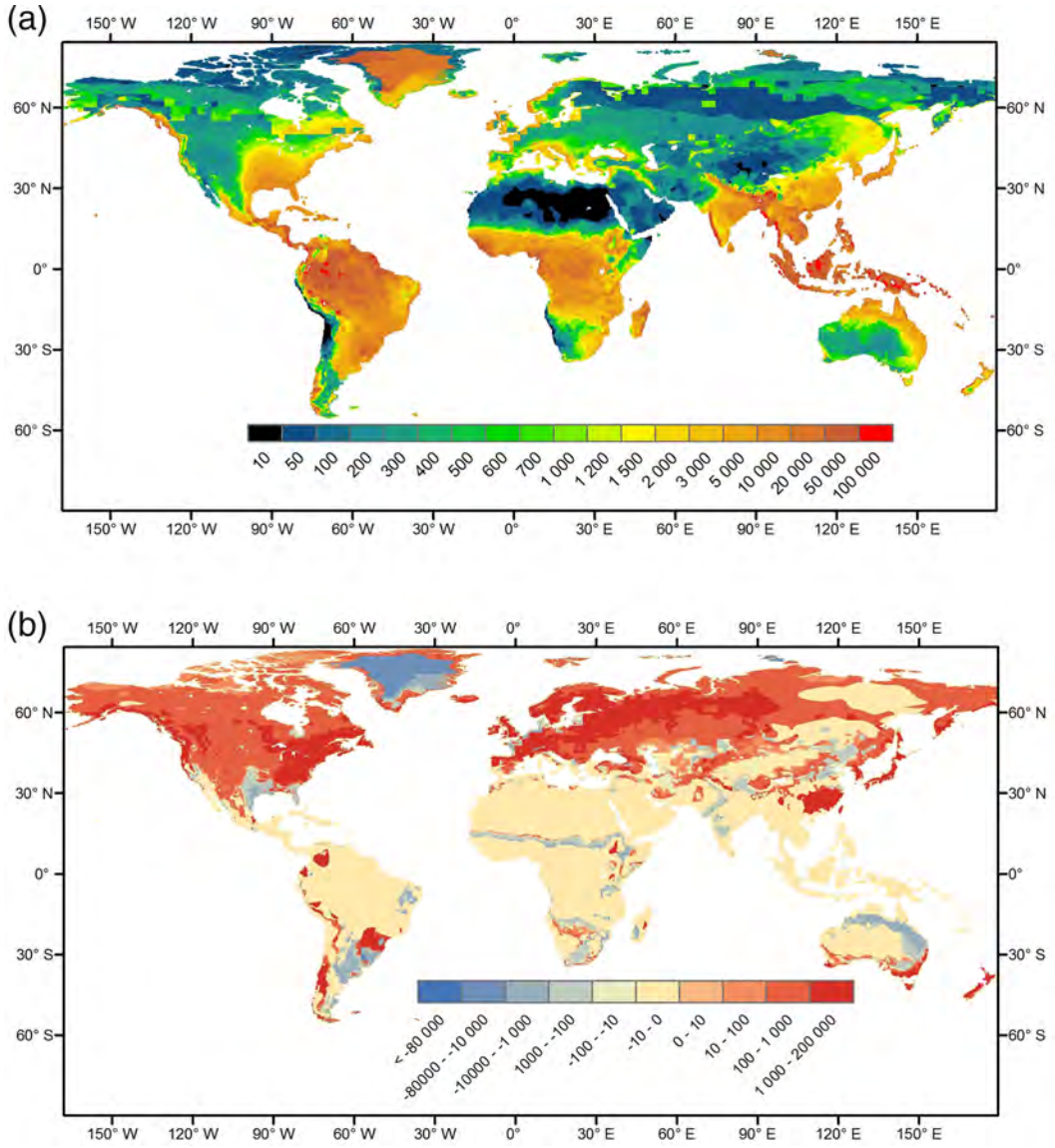

Figure 2.7: **(a)** Global distribution of the new modelled R values according to the new regression equations; and **(b)** a difference map between R values calculated according to the method of Renard and Freimund (1994) and the new modelled R values (MJ mm ha^{-1} h^{-1} year^{-1}), where blue colours indicate lower R values by Renard and Freimund (1994) compared to the new modelled R values, while reddish colours indicate higher R values; map resolution is 5 arcmin.

there is no high temporal resolution precipitation intensity data available on a global scale, the R factor can still be represented well for most climate zones on a large spatial scale. This can be done by using other parameters, such as elevation, and especially one representative of precipitation intensity, such as the SDII. The SDII played an important role here as it improved the estimation of the R factor significantly, even though data was only available at a very low resolution as compared to the other data sets of precipitation, elevation and climate zone classification.

Table 2.6: Mean high resolution R values ($\mathrm{MJ\,mm\,ha^{-1}\,h^{-1}\,year^{-1}}$) from the USA and Switzerland and mean modelled R values with uncertainty range for each addressed climate zone.

Climate	Observed	Renard and Freimund method	Adjusted method	Adjusted method
	R mean	R mean	R mean	uncertainty range
BWk	284	533	291	158–495
BSh	2168	1356	2207	1723–2828
BSk	876	884	885	749–1046
Csb	192	1136	192	133–292
Cfa	5550	5607	5437	4830–6123
Cfb	1984	5359	1971	1431–2715
Dsa	172	445	171	86–340
Dsb	175	896	168	151–187
Dsc	115	374	115	91–145
Dwa	1549	1444	1551	1280–1879
Dwb	1220	1418	1214	1057–1395
Dfa	2572	2983	2582	2346–2843
Dfb	1101	1798	1124	922–1371
Dfc	483	701	483	423–552
ET	1352	6257	1249	23–68 088
EF + EFH	1468	5469	1450	16–132 001
ETH	945	5580	832	0–6 314 918

2.2.3 Parameter estimations based on observed data

In order to demonstrate the consequences of the new parameterizations of the S and R factors for global soil erosion rates, we have to compute the other individual RUSLE factors, the K and C factors. Estimations of the K factor were based on soil data from the gridded 30 arcsec Global Soil Data set for use in Earth System Models (GSDE). GSDE is based on the Harmonized World Soil database (HWSD) and various other regional and national soil databases (Shangguan et al., 2014). We used the method of Torri et al. (1997) to estimate the K factor as described in section 2.2.1, and gave volcanic soils a K factor of $0.08\,\mathrm{t\,ha\,h\,ha^{-1}\,MJ^{-1}\,mm^{-1}}$. This is because these soil types are usually very vulnerable to soil erosion, and the observed K values are beyond the range predicted by the method of Torri et al. (1997) (Van der Knijff et al., 1999). To account for the effect of stoniness on soil erosion we used a combination of the methods by Cerdan et al. (2010) and Doetterl et al. (2012), who based their methods on the original method of Poesen et al. (1994). For non-agricultural areas we used the method of Cerdan et al. (2010), where they reduced the total erosion by 30 % for areas with a gravel percentage larger or equal to 30 %. For agricultural and grassland areas we

used the method of Doetterl et al. (2012), where erosion was reduced by 80 % in areas where the gravel percentage exceeded 12 %.
We calculated the C factor according to the method of De Jong et al. (1998), using 0.25 degree NDVI and land use data for the year 2002. An important limitation of this method is the fact that in winter the C factor is estimated too high (Van der Knijff et al., 1999). This is because the method does not include the effects of mulch, decaying biomass and other surface cover reducing soil erosion. To prevent the C factor from being too high, maximum C values for forest and grassland of 0.01 and 0.05 for pasture were used.
Doetterl et al. (2012) showed that the L and P factors do not contribute significantly to the variation in soil erosion at the continental scale to global scale, when compared to the contribution of the other RUSLE factors (S, R and C). However, this does not mean that their influence on erosion should be ignored completely. They may play an important role in local variation of erosion rates. In our erosion calculations we do not include these factors because we have too little or no data of these factors on a global scale. Including them in the calculations would only add an additional large uncertainty to the erosion rates. This would make it more difficult to judge the improvements we made to the S and R factors.

2.2.4 Parameter estimation based on CMIP5 model data

To estimate global soil erosion rates for the last millennium (850-2005AD) climate and land cover data from existing ESM simulations performed under the framework of CMIP5 were used. (Hurrell and Visbeck, 2011; Taylor et al., 2009). Here, simulations from the following ESMs were selected: MPI-ESM, IPSL-CM5A, CCSM4, MIROC-ESM and bbc-csm1-1 (Table 2.7). For consistency reasons related to the next chapter the low-resolution version of all models will be used for the complete time period (850-2005AD), even though in some cases there was a medium-resolution version available for present-day (1850-2005AD). For present-day the historical experiment (1850-2005AD) was used, for which IPSL-CM5A and CCSM4 provided each a set of six ensemble simulations, and the other models provided each a set of three ensemble simulations. For the total period of the last millenium we combined the past1000 experiment (850-1850AD) with the historical experiment.

For the past1000 experiment each model provided only one simulation. From each model the monthly land cover fractions, leaf area index (LAI) and daily and monthly total precipitation rates, were extracted if available (Table 2.7). The low resolution version of the CCSM4 and bbc-csm1-1 had no available land cover fractions. We therefore used the land cover fractions and LAI from MPI-ESM for the CCSM4 model, and the land cover fractions and LAI from MIROC-ESM for the bbc-csm1-1, as the last two models were similar in their resolution. Due to the resolution of 5 arcmin of the adjusted RUSLE model the processed data of the CMIP5 models was remapped

Table 2.7: List of ESMs used in this study. Data is taken from CMIP5. Tm is monthly temperature, Pm is monthly precipitation, Pd is daily precipitation.'y' stands for yes, data exists, while 'n' stands for no, data is missing.

model	group	resolution	Tm	Pm	Pd	LAI	Tree fraction	Crop fraction	Grass fraction	Shrub fraction	Pasture fraction	Baresoil fraction
MPI-ESM-LR	Max Planck Institute for Meteorology	1.875	y	y	y	y	y	y	y	y	y	y
IPSL-CM5A-LR	Institute Pierre-Simon Laplace	3.75	y	y	y	y	y	y	y	n	n	y
CCSM4	National Center for Atmospheric Research	1.25	y	y	y	y	n	n	n	n	n	n
MIROC-ESM	Japan Agency for Marine-Earth Science Technology, Atmophere and Ocean Research Institute (University of Tokyo), and National Institute for Environmental Studies	2.8125	y	y	y	y	y	y	y	n	y	y
bcc-csm1-1	Beijing Climate Center	2.8125	y	y	y	n	n	n	n	n	n	n

to this specific resolution.
Due to the lack of data on the NDVI, the method as presented in the previous section for estimation of the C factor was not used here. Instead, a new method was developed based on the C values provided by Panagos et al. (2015) for Europe, combined with land cover fractions and LAI from the selected CMIP5 model data. The LAI is used to estimate the percentage vegetation cover (cf), which has been shown to influence the overall value of the C factor for a specific land cover type (of Agriculture, 1978). The cf is estimated according to Beer's Law approximation:

$$cf = 1 - e^{\{-LAI/2\}} \tag{2.18}$$

Four cf classes are distinguished: ≤ 0.2, 0.2 to 0.45, 0.45 to 0.75, and > 0.75. The range in C factors for the different land cover types used in this study is given in table 2.8. If the cf was smaller than 0.22 all landcover types, except bare soil, were given a maximum value of 0.45. This value corresponds to the maximum C values found by of Agriculture (1978) and Panagos et al. (2015). For bare soil the maximum C value was somewhat higher in comparison to the other land cover types according to Panagos et al. (2015).
For the estimation of the R factor the new regression equations presented in section 2.2.2.2 were used here. First, climate classification maps were derived based on the criteria from Peel et al. (2007) for each 100 year time period starting from 850AD till 1950AD, and for present day (1950-2005AD). The derivation of climate classification maps for the last millennium based on CMIP5 data is a new aspect of this study. These maps may differ from the map of Peel et al. (2007) for present day for certain regions such as western Europe, where the models show biases in precipitation amounts. However, the main global variability in the climate zones is captured. To estimate the SDII the daily precipitation rates from the ESM data was used. In combination with the 5 arcmin mean elevation the mean R maps for the 100 year time periods between 850 and 1950AD and present day (1950-2005AD) were derived.
For present day erosion rates with the adjusted RUSLE model were calculated as described previously for each of the ensemble simulations of the CMIP5 models. For the last millennium three main simulations were performed to estimate erosion rates

based on data from the CMIP5 models. The three simulations are: (1) The climate change simulation: Here, the land cover was fixed to the mean conditions of the period 850-950AD during the last millennium, while the climate was variable, (2) The land use change simulation: Here, the climate was fixed to the mean conditions of the period 850-950AD during the last millennium, while the land cover was variable, (3) The default simulation: Here, both land cover and climate vary throughout the last millennium.

Table 2.8: C values for different land cover types and cf classes.

cf	Forest	Shrubs	Grass	Pasture	Crops	Bare soil
> 0.75	0.0001	0.003	0.01	0.05	0.03	0.1
0.6 – 0.75	0.00089	0.029	0.029	0.077	0.14	0.2
0.45 –0.6	0.00168	0.0559	0.048	0.1	0.26	0.29
0.2 – 0.45	0.003	0.1	0.08	0.15	0.45	0.45
≤ 0.2	0.45	0.45	0.45	0.45	0.45	0.55

2.3 Results and discussion

2.3.1 Present day

2.3.1.1 Global erosion rates based on observed data

We applied the RUSLE model with the settings mentioned in the previous sections at a 5 arcmin resolution on a global scale for present day (see time resolutions of data sets in Appendix A.1). We calculated global soil erosion rates with four different versions of the RUSLE model: (a) the unadjusted RUSLE, (b) RUSLE with only an adjusted S factor, (c) RUSLE with only an adjusted R factor, and (d) the adjusted RUSLE (all adjustments included).

We found a global average soil erosion rate for the adjusted RUSLE of $6.5\,\mathrm{t\,ha^{-1}\,year^{-1}}$ (Fig. 2.8a). When including the uncertainty arising from applying the linear multiple regression method, the mean global soil erosion rate differs between 5.3 and $15\,\mathrm{t\,ha^{-1}\,year^{-1}}$. Furthermore, the RUSLE version with only an adjusted S factor shows the highest average global soil erosion rate, while the lowest rate is found for the RUSLE version with only the adjusted R factor (Table 2.9). Figure 2.8c shows the difference between the erosion rates of the S-adjusted RUSLE and the unadjusted RUSLE versions. The erosion rates are in general increased here and mostly pronounced in mountainous regions. This feature is "dampened" when adjusting the R factor.
The difference between the R-adjusted RUSLE and unadjusted RUSLE versions (Fig. 2.8d) shows that the erosion rates are overall decreased in regions where the

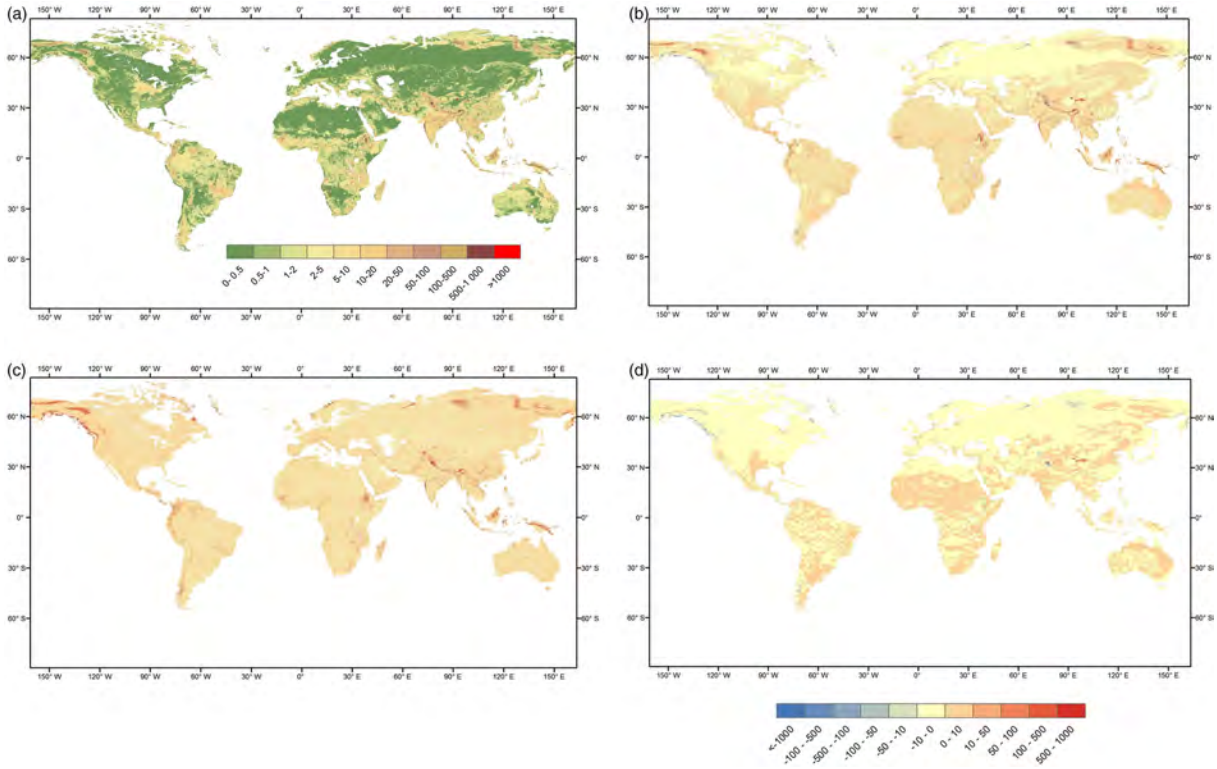

Figure 2.8: **(a)** Global yearly averaged erosion rates according to the fully adjusted RUSLE model; **(b)** a difference map between the fully adjusted and unadjusted RUSLE model; **(c)** a difference map between the adjusted S-RUSLE model and the unadjusted RUSLE model; **(d)** a difference map between the adjusted R-RUSLE model and the unadjusted RUSLE model. In panels **(b)**, **(c)** and **(d)** the reddish colours show an overestimation of the adjusted RUSLE model and yellow to bluish colours show an underestimation (resolution of all maps is 5 arcmin and all units are in $\mathrm{t\,ha^{-1}\,year^{-1}}$).

adjustments are made. When the erosion rates of the unadjusted RUSLE model are subtracted from the fully adjusted RUSLE model (Fig. 2.8b), we find that erosion rates are slightly decreased in areas where the R factor is adjusted. However, for the tropics an increase in erosion rates is found in the fully adjusted RUSLE due to the lack of adjusting the R factor there. This indicates that these two factors balance each other, and that it is important to have a correct representation of all the RUSLE factors on a global scale in order to predict reliable erosion rates.

Table 2.9: Comparison of the global erosion rates ($\mathrm{t\,ha^{-1}\,year^{-1}}$) and percentiles between different versions of the RUSLE model.

	Mean	25th percentile	50th percentile	75th percentile	90th percentile
RUSLE unadjusted	4.5	0.2	0.7	2.4	7.5
RUSLE adjusted with S	9.8	0.3	1.0	3.8	13.5
RUSLE adjusted with R	3.2	0.1	0.5	1.7	5.7
RUSLE adjusted with S and R	6.5	0.1	0.7	2.7	9.6

2.3.1.2 Comparison to observations

In this study the K and C factors are not tested and adjusted for a coarse resolution at global scale and thus validation with existing empirical databases on soil erosion is not fully justified. However, to test if the global erosion rates are in an acceptable range, they are compared to erosion estimates from the NRI database for the USA and erosion estimates from the study of Cerdan et al. (2010) for Europe. These are to our knowledge the only large-scale high resolution empirical databases on soil erosion.

Table 2.10: Statistics of the observed and modelled erosion rates from the unadjusted and adjusted versions of the RUSLE for the USA and Europe ($t\,ha^{-1}\,year^{-1}$).

Region	Source	Observations			Adjusted RUSLE			Unadjusted RUSLE		
		Range	Mean	Standard deviation	Range	Mean	Standard deviation	Range	Mean	Standard deviation
Europe (aggregation country level) no small countries	Cerdan et al. (2010)	0.1–2.6	0.9	0.7	0.1–7	2.3	2.1	0–14	2.8	3.6
USA (aggregation HUC4 level)	NRI database	0–11	1.6	2.1	0.2–13	1.6	1.9	0–14	1.4	1.8

The NRI database contains USLE erosion estimates for the year 1997, which are available at the Hydrologic Unit Code 4 (HUC4) watershed level. We aggregated the resulting erosion rates from the adjusted and unadjusted RUSLE models to the HUC4 watershed level. The results show that the average erosion rates from the adjusted RUSLE model come closer to that of the NRI database (Table 2.10, Fig. 2.9a and b). However, the maximum average HUC4 soil erosion rate from the adjusted RUSLE is somewhat higher compared to the NRI database. From these results we can conclude that the erosion rates of the adjusted RUSLE fall in the range of observed values but that there are still some local overestimations. Some of these overestimations can be found in the south-west of the USA where the adjusted RUSLE shows a slightly worse performance compared to the unadjusted RUSLE. The R factor in this region was not changed as it was already estimated well by the method of Renard and Freimund (1994), however, the S factor increased due to the hilly terrain. Without adjusting the other RUSLE factors (K and C), this resulted in an overall increase in soil erosion rates. This indicates that the other RUSLE factors may play an important role in this region. Furthermore, we see that along the west coast of the USA the erosion values are not much improved with the adjusted RUSLE model. This is mainly because some climate zones such as the temperate climate zone with a dry and warm summer (Csb) prevail in this region, for which the R factor is still difficult to estimate in a correct way (Table 2.3).

For Europe, Cerdan et al. (2010) used an extensive database of measured erosion rates on plots under natural rainfall. They extrapolated measured erosion rates to all of Europe (European Union area) and adjusted them with a topographic correction. This correction was based on the L and S factors of the RUSLE model. They also applied

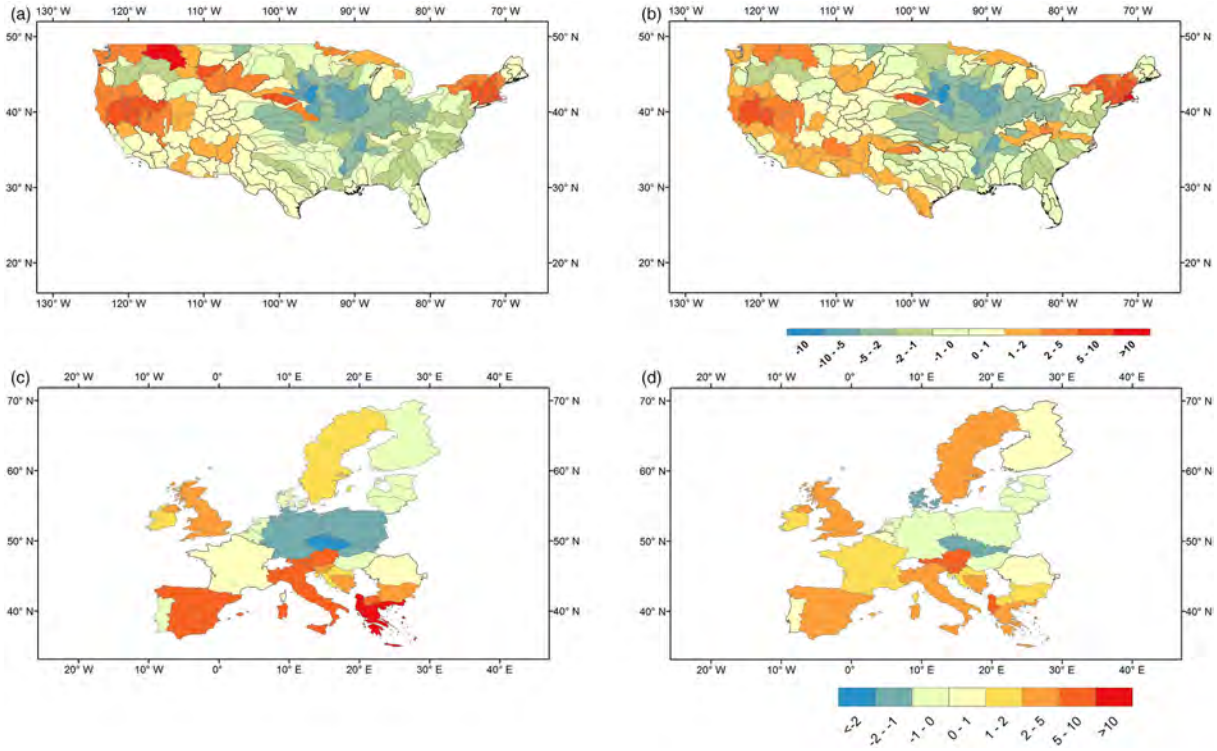

Figure 2.9: (Top) Difference plots between soil erosion estimates from the NRI database for the USA and estimates of **(a)** the unadjusted RUSLE model, and of **(b)** the adjusted RUSLE model, all aggregated at HUC4 watershed level. (Bottom) Difference plots between soil erosion estimates from the database of Cerdan et al. (2010) for Europe and estimates of **(c)** the unadjusted RUSLE model and of **(d)** the adjusted RUSLE model, all aggregated at country level. Reddish colours represent an overestimation ($t\,ha^{-1}\,year^{-1}$) while the bluish colors represent and underestimation ($t\,ha^{-1}\,year^{-1}$) compared to the erosion values from the databases.

a correction to account for soil stoniness. For comparison, the soil erosion rates from Cerdan et al. (2010) and the RUSLE estimates in our study are aggregated at country level. The performance of the adjusted RUSLE model was not as good for Europe as compared to the USA. This is not surprising as the RUSLE model is based on soil erosion data of the USA. However, also on the European scale the adjusted RUSLE model performed better than the unadjusted RUSLE model (Table 2.10, Fig. 2.9c and d). In particular, the large erosion rates in the south of Europe as observed in the results of the unadjusted RUSLE model are less extreme in the adjusted RUSLE model. Still, the overall average erosion rate for Europe is overestimated by approximately 2 times (Table 2.10).

The biases in erosion rates as seen for the south-west of the USA and southern Europe can be attributed to several factors. As mentioned before, the other RUSLE factors (K and C) and the way they interact with the R and S factors are not adjusted to the coarse resolution at global scale. We found no clear signal for the land cover types with which the adjusted RUSLE performs better or worse. In general, we can see that the

adjusted RUSLE model still overestimates erosion rates for most land cover types. A short analysis for Europe showed that the largest biases are found for shrubs and the lowest for grassland. However, a more explicit analysis is needed to find out how we can improve the contribution of land cover and land use to erosion rates in the RUSLE model. Explicitly including the interaction between the C and R factor on a monthly timescale could be crucial. This is very important for example in areas with agriculture and areas with a strong seasonal character. Another aspect related to improving the C factor is looking at the location of land use in a certain grid cell. If the land use in a grid cell is located on steep slopes, the resulting erosion in that grid cell would be higher than when it was located in the flatter areas. In this study, however, only mean fractions of land cover and the NDVI are used for each grid cell. This can lead to possible biases in the resulting erosion rates.
Furthermore, land management is not accounted for in this study, which could introduce an important systematic bias in the soil erosion rates especially for agricultural areas. Land management is represented by the P factor in the original USLE; however, it is partly also incorporated in the C factor for agricultural land use through plant residues, cover crops and tillage. A limitation of the NDVI approach to estimate the C factor lies therefore in the inability to estimate this land management effect. Applying this method also limits the interaction between the R and C factors on a monthly to seasonal scale, because this interaction is partly based on land management.
Furthermore, uncertainties in the coarse resolution land cover/land use, soil and precipitation data sets that are not accounted for can lead to the model biases. Also, better adjustment of the R factor for climate zones such as the polar climates could help improve the overall results. Some biases in the erosion rates can also be attributed to the fact that stepped relief, where flat plateaus are separated by steep slopes, is not well captured by the 150 m target resolution used in the fractal method to scale slope. In this way erosion would be overestimated in these areas. Finally, errors and limitations in the observational data sets can also contribute to the differences between model and observations. The study of Cerdan et al. (2010) on Europe, for example, used extrapolation of local erosion data to larger areas, which could introduce some biases. Also, the underlying studies on measured erosion rates used different erosion measuring techniques that can be linked to different observational errors.

2.3.1.3 Global erosion rates based on CMIP5 model data

Here the global soil erosion rates for present day from CMIP5 data are compared with those calculated with the adjusted RUSLE model from observational datasets. Here, erosion rates calculated from observational datasets are referred to as 'observed data', though it should not be confused with actual observed erosion rates. Erosion rates from observed climate and land cover fractions also contain biases and are not the real observed erosion rates, which could be different from the estimates of the adjusted RUSLE model. Additionally, The maximum soil erosion rates are limited to 1000 $\mathrm{t\,ha^{-1}\,year^{-1}}$,

to stay in a realistic range.
Result show that the CMIP5 models differ significantly among each other with respect to the average global soil erosion rates for present day. The spatial correlation between the erosion rates from CMIP5 data and observed data is overall low (Table 2.11), with MIROC-ESM showing the highest correlation and lowest RMSE. Furthermore, present-day mean and median global soil erosion rates of 9.15 and 0.53 $\mathrm{t\,ha^{-1}\,year^{-1}}$, respectively, from the CCSM4 model are found to be closest to the mean and median erosion rates of 6.07 and 0.72 $\mathrm{t\,ha^{-1}\,year^{-1}}$, respectively, from observed data (Table 2.11).
Studying the difference between the models for different regions shows that most of the models agree on the mean soil erosion rate for Europe, Africa and Australia (Fig. 2.10). For these continents the mean erosion rates from the models are also closest to the observed erosion rates. The strongest disagreement is found for Asia, North-America and Central-America. However, for North-America and Asia the uncertainty in the mean erosion rates from observed data is also large. This uncertainty is a result of the regression of the R factor for different climate zones in the adjusted RUSLE model.

Table 2.11: Statistics of present day global soil erosion rates based on CMIP5 data and observed data. The r-value represents the Pearson correlation coefficient and the RMSE is the root mean square error. Units are in $\mathrm{t\,ha^{-1}\,year^{-1}}$. NA stands for 'not available'.

model	25th percentile	50th percentile	75th percentile	90th percentile	mean	standard deviation	uncertainty range	RMSE	r-value
MPI-ESM-LR	0.10	0.43	2.32	11.18	10.15	62.58	9.97 – 10.39	63.37	0.18
IPSL-CM5A-LR	0.05	0.30	1.16	3.92	3.03	22.67	3.00 – 3.12	33.59	0.15
CCSM4	0.12	0.53	2.39	10.10	9.15	57.19	8.52 – 9.43	57.09	0.22
MIROC-ESM	0.05	0.21	0.94	3.80	3.40	24.97	2.72 – 3.79	32.93	0.26
bcc-csm1-1	0.03	0.15	0.66	2.71	3.25	28.42	3.10 – 3.42	34.02	0.23
observed	0.15	0.72	2.68	9.62	6.07	30.49	5.20 – 11.62	NA	NA

Spatial maps of the biases for CMIP5 models with respect to observed data for present day show that most models underestimate erosion rates in the entire or parts of the Amazon region (Fig. 2.11). Most models except for the CCSM4 model also underestimate erosion rates for Australia and some parts of Africa. Furthermore, erosion rates in Europe are generally overestimated. These patterns are found to be strongly correlated with biases related to precipitation rates in the models (Mehran et al., 2014). Although, the overall variability in erosion rates is always the result of an interplay between precipitation and land use, it is expected that here the estimation of precipitation rates plays the main role. In the previous sections it is shown that precipitation strongly impacts the erosion rates. Erosion is, therefore, more sensitive to precipitation changes in the adjusted RUSLE model than to changes in land cover or land use. Furthermore, as the same land cover for the CCSM4 is used as for MPI-ESM, the differences in simulated erosion rates between these models are a result of a different underlying climate representation. MPI-ESM overestimates erosion rates in West-Europe, North-America, Central-Asia and North-China. This model also underestimates erosion for Australia, and parts of Africa and South-America. These biases in erosion rates from MPI-ESM model should be kept in mind when the model will be used to estimate global sediment

redistribution in the next chapter.

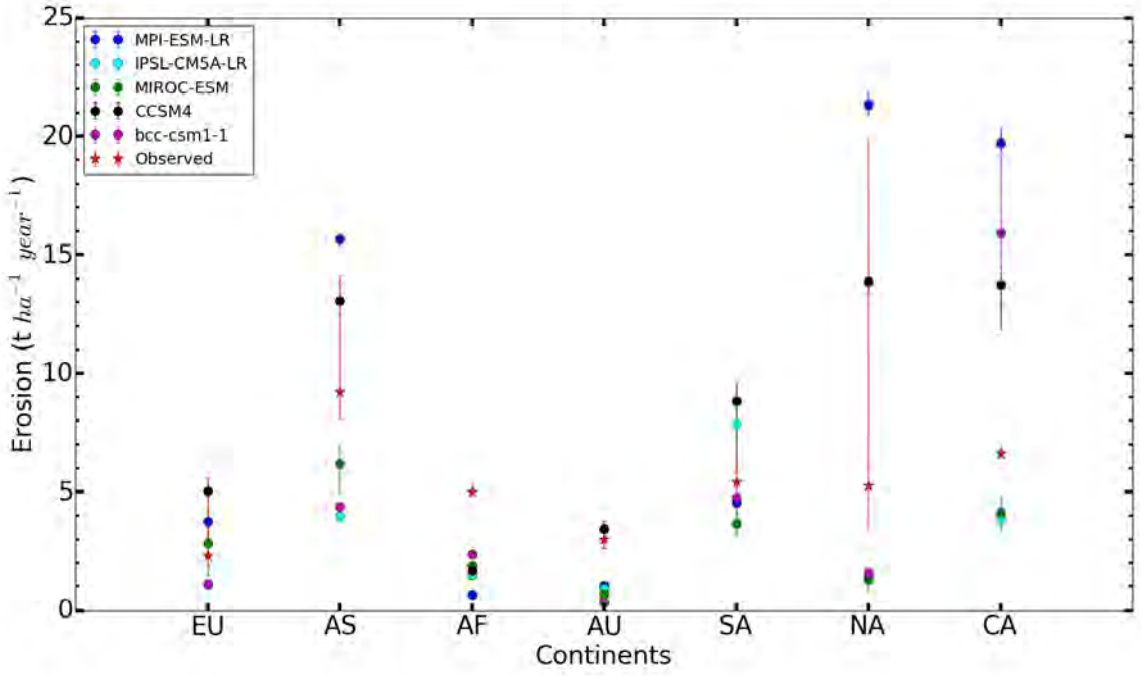

Figure 2.10: Present-day mean global soil erosion rates per region (units are in t ha^{-1} year^{-1}) as estimated based on data from CMIP5 models (circles) and on observed data (stars). The vertical bars for the CMIP5 models show the uncertainty range due to different ensemble members, while the vertical bars for the observed data show the uncertainty range due to the linear regression for the rainfall erosivity. The regions are Europe (EU), Asia (AS), Africa (AF), Australia (AU), South-America (SA), North-America (NA), Central-Americal (CA).

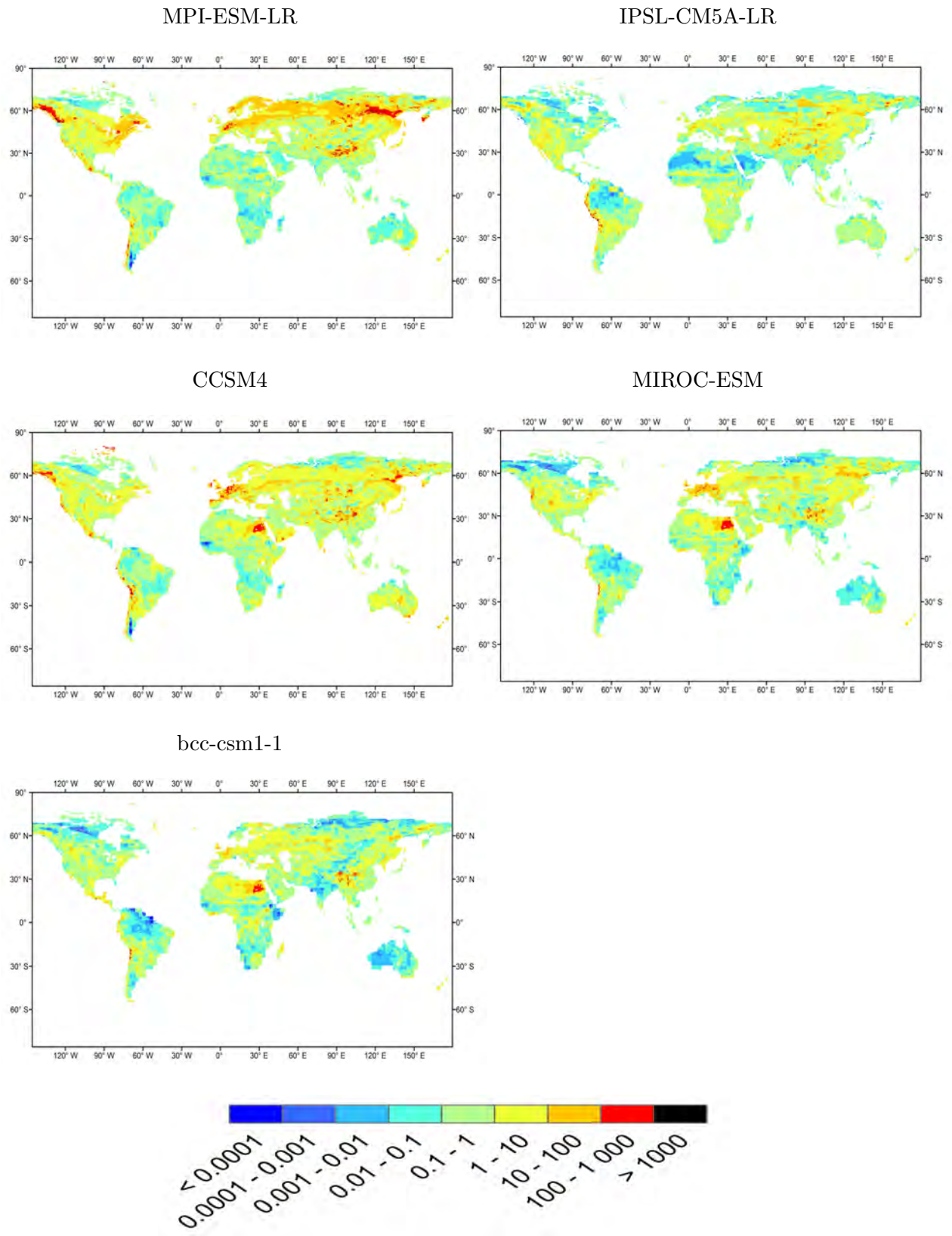

Figure 2.11: Biases (ratios) between erosion rates based on data from different CMIP5 models and the observed data for present day. Bluish colours indicate an underestimation of erosion rates from model data, while reddish colours indicate an overestimation.

2.3.2 Last millennium

2.3.2.1 Trends in global erosion rates based on CMIP5 model data

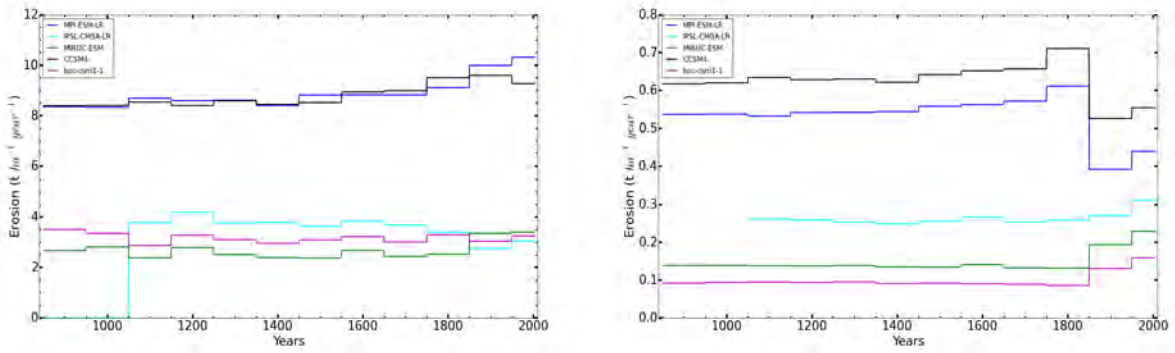

Figure 2.12: Mean (left) and median (right) global erosion rates during the last millennium based on data from different CMIP5 models.

Also for the last millennium a disagreement between the CMIP5 models on the mean and median global soil erosion rates is observed (Fig. 2.12). On the one hand, a significant increase of 2 and 0.9 t ha^{-1} year^{-1}, respectively, is found in the mean global soil erosion rates during the last millennium by MPI-ESM and CCSM4 (Fig. 2.12 and Fig. 2.13). The increasing trend is mainly a result of the strong increase in land use change simulated by these models (Fig. 2.13). Climate change contributes to this increase only after 1850AD.
On the other hand, IPSL-CM5A shows a significant decrease in the mean global soil erosion rate during the last millennium of 0.7 t ha^{-1} year^{-1} (Fig. 2.12 and Fig. 2.13). Here, climate change is the main driver behind the decreasing trend, while land use change contributes to this trend only in the period 1850-2005AD (Fig. 2.13). For the other models no significant trend during the last millennium is found.
However, from figure 2.12 one can observe significant changes in the median soil erosion trends for all models, starting from 1800AD. These signals, although not clear, can be related to the strong land use changes occuring in large regions on earth, for example in the Amazon region. These signals are not as clearly visible from the mean erosion rates in figure 2.12.
Furthermore, we found that most models agree on an increase in erosion rates during the last millennium for Europe, North- and Central-America. For the other regions the models strongly disagree among each other. This is partly due to uncertainties in the simulated land use and climate. Figures on soil erosion trends during the last millennium from CMIP5 models for the different continents are given in Appendix A.1.

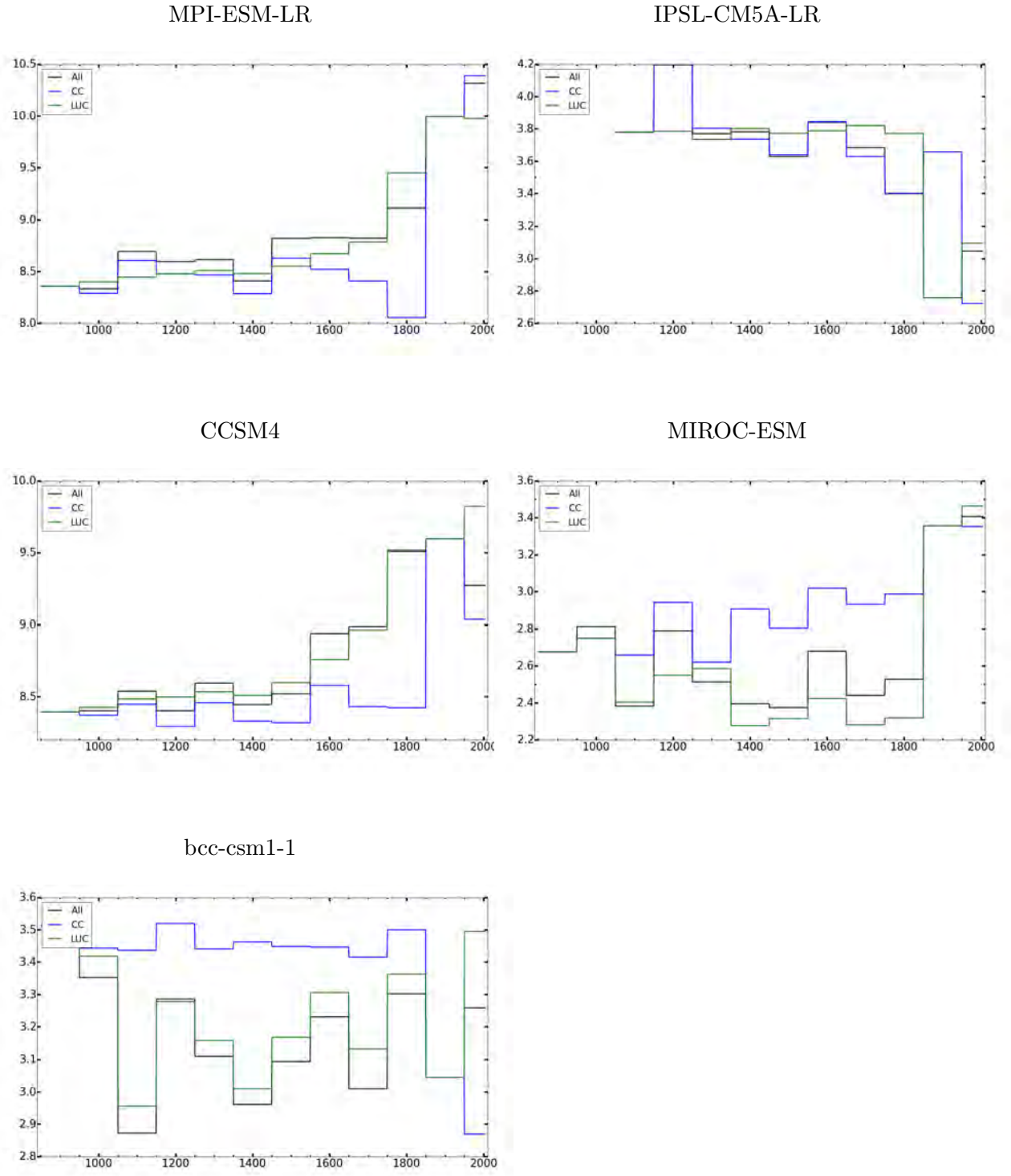

Figure 2.13: Mean global soil erosion rates for the last millennium for the climate change scenario, CC (blue), land use change scenario, LUC (green) and default scenario, All (black), based on data from different CMIP5 models. Units are in $\mathrm{t\,ha^{-1}\,year^{-1}}$.

2.3.3 Limitations of the modelling approach

As mentioned earlier, the other RUSLE factors such as the K and C factors should be adapted to a coarse resolution on global scale, and the seasonal interaction between the C and R factors should be improved. The absence of this can cause biases in regions with a strong seasonal behavior or in agricultural areas that use crop rotation techniques. Also the land management and (P factor) and slope length (L factor) should be incorporated in the global estimation of erosion rates, as these two factors play an important role for agricultural areas. The fact that we ignore these factors on the global scale can cause biases in agricultural areas and could be one of the explanations for the too high erosion rates in these areas.
The adjusted RUSLE model with the new method for C factor calculation cannot be used for estimating high resolution local scale soil erosion rates. The model has been calibrated for a large spatial scale, as the resolution of the model is 5 arcmin. The new method for C factor calculation may limit the applicability of the model in regions with a high diversity of land cover types and a complex landscape. In the latter case slope fractions may be needed to improve the estimation of the C factor. We found that on a large spatial scale the inclusion of slope fractions does not improve the overall erosion rates much.
Furthermore, the adjusted RUSLE model does not simulate extreme soil erosion events, but rather average long-term erosion rates. This means that the adjusted RUSLE model cannot be used to predict extreme soil erosion events in the past or future. Extreme soil erosion events that also include gully erosion, land slides and stream-bank erosion, that can be important on the long-term, especially in steep landscapes.
Also, in order to estimate erosion rates for time periods that go back further than 850AD, the method for calculating the R factor may not be valid anymore due to a different climate. This means that we will need to adapt the criteria for the climate classification maps for the far past.
Concerning the estimations of lateral fluxes of carbon and nutrients, the erosion estimates from the adjusted RUSLE model can only predict the gross lateral fluxes and not the overall net fluxes due to the absence of sediment deposition and transport.

2.4 Conclusions

In the first part of this study we introduced specific methods to adjust the topographical and rainfall erosivity factors to improve the application of the RUSLE model on global scale, using coarse resolution input data.
Our results show that the fractal method by Zhang et al. (1999) and Pradhan et al. (2006) can be applied on coarse resolution DEMs to improve the resulting slope. Although the slope representation improved after applying this method, the results still show a slight dependence on the original grid resolution. This is attributable to several

factors such as the underlying assumption that the standard deviation of elevation (σ) is independent of the DEM resolution and to the breakdown of the fractal method at certain scales.

We compared the rainfall erosivity calculated by the method of Renard and Freimund (1994) to available high resolution or observed erosivity data of the USA, Switzerland and the Ebro Basin. We find that this method results in overall significant biases in erosivity. Therefore, we implemented a linear multiple regression method to adjust erosivity for climate zones of the Köppen–Geiger climate classification system in the USA. Using precipitation, elevation and the simple precipitation intensity index as explaining parameters, the resulting adjusted erosivity compares much better to the observed erosivity data for the USA, Switzerland and the Ebro Basin. Not only are the mean values improved but also the spatial variability in erosivity. It was surprising to notice that using the rather coarse resolution simple precipitation intensity index in the regression analysis made it possible to explain much of the variability in erosivity. This, once more, underpins the importance of precipitation intensity in erosivity estimation.

After calculating the newly adjusted erosivity on a global scale, it is apparent that the tropical climate zones, for which erosivity was not adjusted, show strong overestimations in some areas. This shows that adjusting erosivity for the tropical climate zones should be the next step. The challenge is to find enough reliable long-term and high resolution erosivity data for those regions.

To investigate how the adjusted topographical and rainfall erosivity factors affect the global soil erosion rates, we applied the adjusted RUSLE model on a global scale. We found an average global soil erosion rate of $6.5\,\mathrm{t\,ha^{-1}\,year^{-1}}$. It is, however, difficult to provide accurate uncertainty estimates to these global erosion rates and to provide a good validation with observations. This is due to lack of high resolution data on other individual RUSLE factors such as the land cover, soil erodibility, slope length and support practice. These RUSLE factors are therefore not adjusted for application at coarse resolution on a global scale. We argue that it is important to focus on adjusting the other RUSLE factors for an improved application of the RUSLE model on global scale.

The next step would be to better capture the anthropogenic contribution to global soil erosion. This can be done by adjusting first of all the land cover factor to a coarse resolution application and focusing on the interaction of this factor with rainfall erosivity on a monthly to seasonal basis. This is important because the land cover factor has strong interactions with the rainfall erosivity factor and includes the effect of human activities on erosion through agricultural activities and land management.

To test if the soil erosion rates from the adjusted RUSLE model are in a realistic range, we compared the results to the USLE erosion estimates for the USA from the NRI database and the erosion estimates for Europe from the study of Cerdan et al. (2010). The adjusted RUSLE soil erosion rates, which we aggregated to the watershed level, show a better comparison with the NRI USLE estimates than the unadjusted

RUSLE erosion rates. For Europe, the comparison of the adjusted RUSLE soil erosion rates to the study of Cerdan et al. (2010) were not as good as for the USA. This is not surprising due to the fact that the parameterizations of the RUSLE model are based on soil erosion data of the USA. However, also for Europe, the adjusted RUSLE model performs better than the unadjusted RUSLE model.
We find overestimations by the adjusted RUSLE model for hilly regions along the west coast of the USA and for southern of Europe. We argue that, besides the reasons mentioned before, these biases are due to the fact that the topographical detail may not be enough in some regions to capture the true variability in soil erosion effects by topography. Also, erosivity could not be adjusted for some climate zones that are not present in the USA or Switzerland and needs to be further improved for climate zones such as the polar climate zones.
In the second part of this study the behavior of the adjusted RUSLE model is investigated when using coarse resolution input data from CMIP5 models. First, a new method for calculating the C factor of the RUSLE model is derived based on the land cover fractions and the LAI, as most ESMs have no data on the NDVI. Second, climate and land cover data from multiple ensemble simulations from five different ESMs of the CMIP5 experiment were selected to calculate soil erosion for present day. The different ensemble simulations provide the uncertainty in the resulting erosion rates due to uncertainty in the model data on climate and land cover. The global erosion rates based on data from the CMIP5 models were then compared with the erosion rates based on observed data of environmental factors.
With respect to the overall values of global soil erosion rates, only the mean rates calculated with the data from MPI-ESM and CCSM4 models fall into the uncertainty range of erosion rates based on observed data. Furthermore, only two models (CCSM4 and MIROC-ESM) show a similar continental variability in soil erosion rates as from observed data. However, none of the selected ESMs shows a similar grid-scale variation in global soil erosion rates as from observed data. Furthermore, we found that models and observations generally agree on the mean erosion rates for Australia, Europe and Africa, while strongly disagree for the America's and Asia. Maps showing grid-scale biases between the ESMs and observed data show that for most of the models an overestimation of erosion rates in mountainous areas, West-Europe, North-West China and North-East Africa is found. At the same time an underestimation of erosion rates is found for most models in large parts of the Amazon and some regions above 60 degrees North.
These results indicate that the adjusted RUSLE model is very sensitive to the climate and land cover data from ESMs. It is expected that especially biases in precipitation rates from models play an important role, as precipitation is the main driver of soil erosion besides topography.
In the final part of this study three simulations on soil erosion were performed for the last millennium based on data from the CMIP5 models. Here, the purpose was to investigate the contribution of land use change and climate change on soil erosion

during the last millennium. For the climate change simulation the land cover was fixed to the conditions between 850 and 950AD during the last millennium, while for the land use change simulation the climate was fixed to the conditions between 850 and 950AD. The third simulation is the default simulation where both climate and land cover were changing during the last millennium.
Results show that the models disagree on the global trend of erosion during the last millennium. MPI-ESM and CCSM4 show a significant increase in global soil erosion rates during the last millennium, which is mainly related to a strong land use change in most parts of the world. IPSL-CM5A model shows a decreasing trend mainly due to strong precipitation decrease in the tropics, especially in South-America. The other models do not show a significant increase or decrease in the mean erosion trend during the last millennium. However, the median global soil erosion trends from all models show a significant signal related to land use change starting from 1800AD.
We conclude that though there is still much improvement possible to the RUSLE model with respect to topography and erosivity, the methods proposed in this study seem to be promising tools for improving the global applicability of the model. However, when using climate and land cover data from ESMs to drive the model, we found that the performance of the model is strongly affected by the representation of the coarse resolution climate and land cover data in ESMs. In order to better estimate soil erosion with ESMs it is thus essential that precipitation, as one of the drivers of soil erosion, is represented well by the ESMs.

Chapter 3

Land use change as the main driver of the change in sediment storage during the last millennium

3.1 Introduction

An accurate quantification of large-scale soil redistribution is essential to better quantify and constrain the impact of human activities on the biogeochemical cycles. However, data on large to global scale soil redistribution rates are scarce to non-existing. There exist several modelling approaches to estimate global soil erosion rates (Yang et al., 2003; Ito, 2007; Montgomery, 2007; Doetterl et al., 2012; Naipal et al., 2015). These modelling approaches mainly address the soil detachment process only, and do not simulate the dynamics of sediment by ignoring processes such as sediment deposition and transport. There is, to our knowledge, no globally applicable model that can explicitly simulate soil redistribution, which is a result of the sediment dynamics in a landscape, for the past, present and future. The lack of such kind of large-scale models on soil redistribution substantially limits the understanding of the relative importance of the various effects of soil erosion and related processes on the global biogeochemical cycles.

The holistic understanding of the interaction and linkages between soil erosion, deposition and transport that comprise soil redistribution, can be addressed using the sediment budget approach (Walling and Collins, 2008). Slaymaker (2003) defined the sediment budget as a mass-balance-based approach where the mass of sediments, water or nutrients is conserved in the considered system so that the net increase in storage is equal to the excess of inflow over outflow of the conserved quantity. However, long-term large-scale sediment budgets are very scarce to non existing. Sediment budgets that have been constructed previously range from small catchments (Verstraeten and Poesen, 2000; Walling et al., 2001) to large river catchments (Milliman and Meade,

1983; Ludwig and Probst, 1998; Syvitski et al., 2003; Slaymaker, 2003). However, these sediment budgets are usually for present-day only as they are mostly based on measurements using methods such as sediment tracing or fingerprinting. Also, most of these studies only focus on the sediment delivery from a catchment. These studies are therefore of limited use for assessing the spatial distribution of sediment sources and storage or in predicting long-term sediment yields. Considering explicitly the spatial distribution of these variables within a catchment is not only essential for a proper land management strategy to combat land degradation, but also for a detailed assessment of how erosion and sediment transport interact with the carbon and nutrient cycles. For example, it is important to distinguish between sediment related processes in floodplain and hillslope systems (Hoffmann et al., 2013). Human activities usually lead to a stronger increase in sediment deposits on hillslopes compared to floodplains, and an overall decreased export of sediment out of a catchment, despite increased soil erosion (de Moor and Verstraeten, 2008). In this way, sediment stored in floodplains and on hillslopes over long timescales can significantly delay or alter the human induced changes to the carbon and nutrient cycles (Hoffmann et al., 2013). This indicates that there is a need for long-term sediment budgets, as they can provide essential information on the forces behind sediment, carbon and nutrient fluxes in a catchment such as human activities and climate change.

There is thus a need for spatially explicit models that can simulate long-term sediment budgets. There exist different spatial models of suspended sediment flux that also consider the soil redistribution or sediment dynamics in a catchment (Merritt et al., 2003; de Vente and Poesen, 2005; Ward et al., 2009). However, many of them are developed to simulate single events or require input data that is not available for large spatial scales (Wilkinson et al., 2009). There are also partly empirical models which can operate on catchment scale such as the WATEM/SEDEM model, which is used to predict hillslope sediment storage and sediment yields (de Moor and Verstraeten, 2008; Nadeu et al., 2015). Or such as the suspended sediment model from Wilkinson et al. (2009) that also simulates some other processes such as floodplain deposition, gully and riverbank erosion. However, these models are not compatible for a global scale application as they require parameters for which data is not available on a global scale and these type of models also need to be calibrated to measured sediment yields of the studied area (Van Rompaey et al., 2001). Pelletier (2012) proposed a global applicable model for long-term suspended sediment discharge, where he used various environmental controlling parameters to simulate soil detachment and sediment transport. However, in his study he mainly focuses on the sediment discharge and delivery of catchments and his model does not take into account the full dynamics of sediment in a catchment, which would also include the spatial distribution of sediment deposition and storage in the different reservoirs of a catchment. Furthermore, he does not consider land use change and thus his approach is limited to natural catchments only.

In this framework we present a new large-scale sediment budget model that is able to simulate spatial patterns in soil erosion, deposition and transport, according to climate

and land use. The overall objective of this study is to present and evaluate the new model for the non-Alpine part of the Rhine catchment first, and then test its applicability on a global scale using the environment of ESMs. The choice of the Rhine catchment is based on the fact that it is the only large catchment with a long land use history for which we had long-term sediment storage data available. For the validation of the model we used scaling relationships between sediment storage and catchment area found from observations for the non-Alpine part of the Rhine catchment by Hoffmann et al. (2013). The scaling relationships are an important criteria for the sediment budget model, as they represent the overall main behavior of sediment in a catchment as function of catchment area. These relationships can thus function as a simple test for the spatial variability of stored sediment that is modelled with a large-scale coarse resolution sediment budget model. We use the model to quantify the spatial variability of floodplain and hillslope sediment storage for the Rhine catchment, and its dependence on climate change and land use change during the last millennium (850-2005AD). We also apply the model on a global scale and investigate the response of 20 different large catchments to the climate and land use change during the last millennium. We also aim to investigate which catchment characteristics determine the spatial variability and the overall change of sediment storage, and how these characteristics influence the effects of land use change on soil redistribution during the last millennium.

3.2 Methods

3.2.1 Basic model concept

The main purpose of the sediment budget model presented here, is to estimate large-scale long-term floodplain and hillslope sediment storage and lateral fluxes of sediment. The model should therefore be spatially explicit and capable of estimating erosion, deposition and sediment transport processes. Furthermore, we want to differentiate between floodplain and hillslope sediment storage for a better quantification of the impact of human activities in a catchment. Therefore, we use a grid cell based approach where we assume that each grid cell contains a floodplain and hillslope reservoir. Before we can define a model that satisfies the above mentioned conditions we have to make some basic assumptions first. Firstly, as it is difficult to disentangle the floodplains and hillslopes in available soil data sets, we assume that each grid cell contains both a hillslope and a floodplain reservoir. When estimating large-scale sediment storage with the aim of predicting fluxes of carbon in the future, the focus is to get the large-scale spatial patterns right, rather than the precise estimates of sediment storage. Secondly, we assume that the deposition and sediment transport behave differently between the floodplain and hillslope reservoirs on the timescale of the last millennium. Thirdly, erosion is considered to mainly take place on hillslopes, where part of the eroded sediment is directly transported from hillslopes and deposited in the floodplains.

(a)

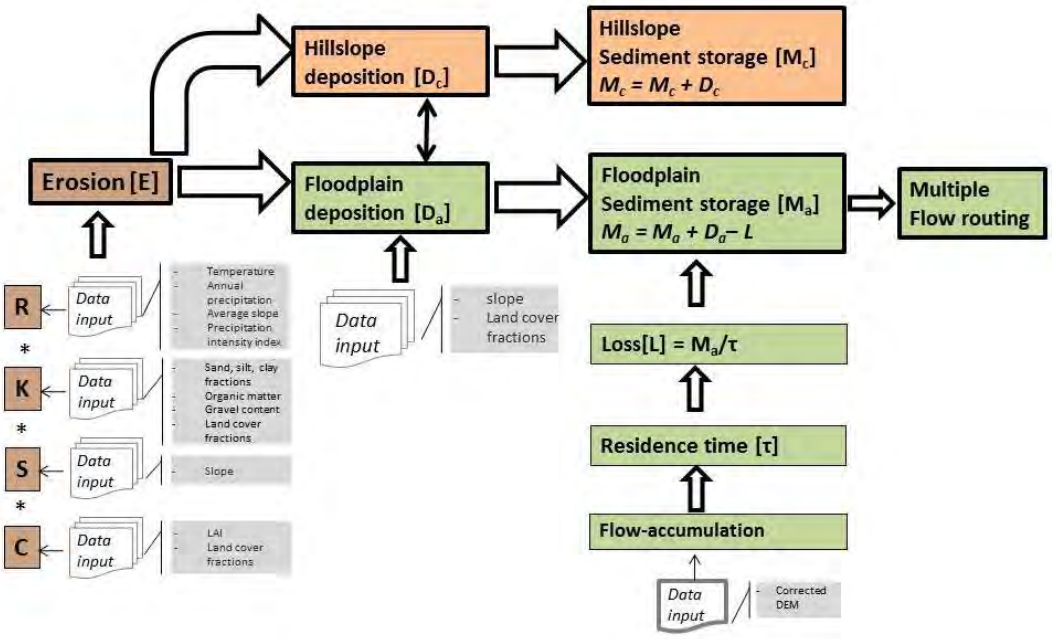

(b)

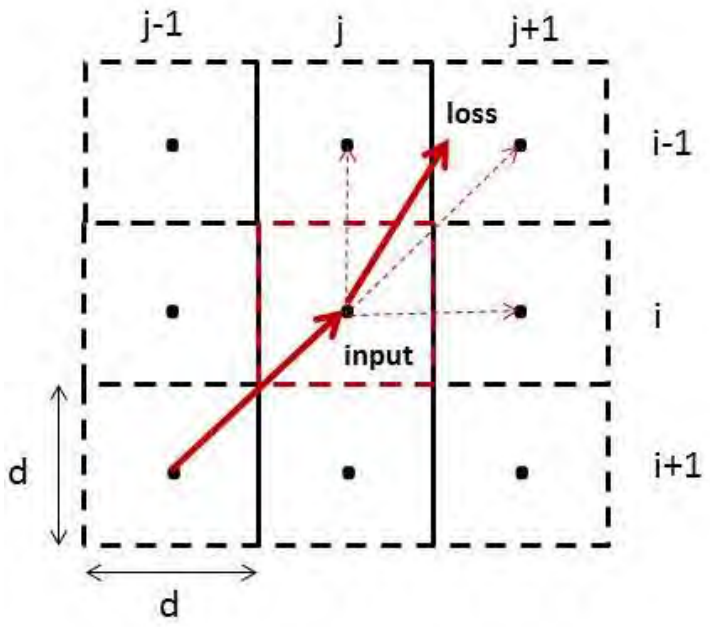

Figure 3.1: Model scheme (a) with multiple flow routing (b). d is the grid size, i counts grid cells in the latitude direction, while j counts grid cells in the longitude direction. The red arrows represent the possible sediment flow directions.

The underlying model framework (Fig. 3.1a) that consists out of the erosion, deposition and sediment transport modules, is based on the sediment mass-balance method. Here the change in sediment storage (M) within a certain unit of time and space is given by the difference between sediment input and sediment output (Slaymaker, 2003). For sediment stored in floodplains (M_a), this leads to

$$\frac{dM_a}{dt} = D_a - L \tag{3.1}$$

This can be approximated by the following as function of time:

$$\frac{dMa}{dt} = D_a(t) - k * M_a(t) \tag{3.2}$$

where $D_a(t)$ is the time-dependent input rate in the model, which is independent from $M_a(t)$. $k * M_a(t)$ is the loss term in the floodplain reservoir, and k is the specific rate for floodplains.
The specific rate is the inverse of the residence time ($1/\tau$) for floodplain sediment, which is defined as the number of years a soil particle stays in the floodplain reservoir of a certain grid cell. τ is assumed to be independent of time for timescales in the order of several thousands of years, and is assumed to increase exponentially with catchment area, where the catchment area is represented by the weighted flow-accumulation

$$\tau = e^{\frac{(FlowAcc - a_\tau)}{b_\tau}} \tag{3.3}$$

a_τ and b_τ are residence time constants and $FlowAcc$ is the flow-accumulation. Flow-accumulation is defined as the number of grid cells upstream that flow into a certain grid cell. As each grid cell represents a certain catchment area, the value of τ will be dependent on the location of the grid cell in the catchment. The presented relationship between τ and catchment area in Eq.(3.3) is based on the fact that large catchment areas are usually characterized by low slopes which mainly result in a low connectivity that makes the system capable of storing sediment for a long time. The opposite is true for small catchment areas, where the connectivity is usually high and the sediment in these systems will therefore have short residence times (Hoffmann, 2015). It should be noted that Eq.(3.3) is dependent on the grid resolution of the model.
The deposition rate (D_a) in the floodplain reservoir is defined as a certain fraction of the erosion rate in a grid cell. Eq.(3.2) can be rewritten as:

$$\frac{dM_a}{dt} = f(t) * E(t) - \frac{M_a(t)}{\tau} \tag{3.4}$$

The erosion rate, E ($\mathrm{t\,ha^{-1}\,year^{-1}}$), is computed according to the adjusted RUSLE model, which computes annual averaged rill and interril erosion rates and is formulated

as a product of a rainfall erosivity factor (R, MJ mm ha^{-1} h^{-1} year^{-1}), a slope steepness factor (S,dimensionless), a soil erodibility factor (K, t ha h ha^{-1} MJ^{-1} mm^{-1}), and a crop cover factor (C,dimensionless) (chapter 2).
Where f is the dimensionless floodplain deposition fraction ranging between 0 and 1. The floodplain deposition fraction is calculated by a simple growth function where deposition is a function of the mean topographical slope and the main land cover type in a grid cell:

$$f = a_f * e^{\{b_f * \frac{\theta}{\theta_{max}}\}} \tag{3.5}$$

where a_f and b_f are constants for deposition and dependent on the land cover type, and θ is the average percent slope on a 5 arcmin resolution grid. θ_{max} is the maximum percent slope. An increase in the overall average slope of a grid cell leads to a larger transport of eroded soil from the hillslopes to the floodplains. This results in an increase in the deposition rate to the floodplain reservoir of that specific grid cell. Hereby we consider in Eq.(3.5) that this increase is exponential. For a natural landscape we assume a good 'sediment connectivity' between hillslopes and the floodplain in a grid cell. In natural landscapes the sediment connectivity is largely based on the vegetation density and morphological structures (Gumiere et al., 2011; Bracken and Croke, 2007). To keep the model simple we do not adapt these parameters to the complexity of natural landscapes, but rather differentiate between the deposition rates in natural and agricultural landscapes, assuming that the sediment connectivity differs fundamentally between these landscapes. Several recent studies (Hoffmann et al., 2013; de Moor and Verstraeten, 2008; Gumiere et al., 2011) showed that a lot of eroded sediment is deposited and stored directly on the hillslopes where agricultural activities take place. Agricultural activities that use anthropogenic structures, reduce the sediment transport from hillslopes to the floodplain (Gumiere et al., 2011). In this way, the stored hillslope sediment is disconnected from the fluvial system on timescales of 100 to a few 1000 years. Based on this, we assume that for agricultural land (crop and pasture) and grassland the sediment connectivity is disturbed. A bad sediment connectivity will result in a larger fraction of eroded soil that stays on the hillslopes compared to the fraction that flows along the hillslopes and is deposited in the floodplain. For natural landscapes we assume a better sediment connectivity, meaning that a larger fraction of the eroded soil will be deposited in the floodplains compared to the fraction that stays on the hillslope. Here we ignore morphological conditions that can cause deconnectivity in the landscape.
After calculating erosion and deposition, the sediment is transported between the grid cells based on a multiple flow sediment routing scheme such as presented by Quinn et al. (1991) (Fig. 3.1b). In the multiple flow routing scheme the weight (W, dimensionless), which specifies the part of the flow that comes in from a neighboring grid cell, is calculated as:

$$W_{k,l}(i,j) = \frac{\theta_{k,l}(i,j) * c_{k,l}(i,j)}{\sum_{k,l=-1}^{1}[\theta_{k,l}(i,j) * c_{k,l}(i,j)]} \tag{3.6}$$

where c is the contour length and is respectively, 0.5 in the cardinal direction and 0.354 in the diagonal direction. (i,j) is the grid cell in consideration where i counts grid cells in the latitude direction and j in the longitude direction. $i+k$ and $j+l$ specify the neighboring grid cells where k and l can be either -1, 0 or 1. θ is calculated here as:

$$\theta_{k,l}(i,j) = \frac{h(i,j) - h_{k,l}(i,j)}{d} \tag{3.7}$$

where, h is the elevation in meters derived from a digital elevation model, d is the grid size in meters.
The floodplain sediment storage rate, M_a ($\mathrm{t\,ha^{-1}\,year^{-1}}$), of a grid cell (i,j) is then a function of the deposition rate in that grid cell, the loss from that grid cell and the incoming sediment from the neighboring grid cells, and is calculated at each time step t as:

$$M_a(i,j,t+1) = M_a(i,j,t) + [f(i,j,t+1) * E(i,j,t+1) - \frac{M_a(i,j,t)}{\tau(i,j)}] + \sum_{k,l=-1}^{1}[\frac{M_{ak,l}(i,j,t)}{\tau_{k,l}(i,j)} * W_{k,l}(i,j)] \tag{3.8}$$

Here t is discretized to years.
For hillslopes the change in sediment storage is assumed to be equal to the input rate, because we assume that the stored hillslope sediment has an infinite residence time on the timescale of the last millennium (Eq.3.9). This means that the hillslope sediment storage will increase linearly with time (Eq.3.10). The hillslope sediment deposition rate (D_c) is here defined as the remaining part of the eroded soil that has not be been transferred to the floodplain directly (1-f). The equations for the hillslope sediment storage rate (M_c, $\mathrm{t\,ha^{-1}\,year^{-1}}$) are represented by:

$$\frac{dM_c}{dt} = D_c = (1-f) * E \tag{3.9}$$

$$M_c(i,j,t+1) = M_c(i,j,t) + (1 - f(i,j,t+1)) * E(i,j,t+1) \tag{3.10}$$

3.2.2 Model implementation and parameter estimation

As mentioned in the introduction of this study, we first implement the sediment budget model on the Rhine catchment to investigate its behavior and validate and calibrate the model with existing data on sediment storage. After validating and calibrating the model for the Rhine catchment we apply the model on a global scale.

The resolution of the sediment budget model is 5 arcmin. We chose this particular model resolution, because we assume that this is the optimal resolution when considering that each grid cell contains a floodplain and hillslope fraction. Here, a higher resolution could lead to cases where this assumption is not met. Also, the 5 arcmin resolution fits well with the resolution of the adjusted RUSLE model. The sediment budget model uses climate and land cover data from simulations of MPI-ESM that have been performed under the CMIP5 framework (chapter 2). As this data was given at a resolution of 1.875 degrees, we had to downscale the data to the resolution of the sediment budget model. For the period 1850-2005AD three ensemble members from MPI-ESM (r1i1p1, r2i1p1, r3i1p1) were available, while for the period 850-1850AD only one ensemble member (r1i1p1) was available. This data existed on a 6 hourly, monthly or yearly time step for the last millennium.
The R factor of the adjusted RUSLE model is calculated according to the new regression equations described in chapter 2. The S, C and K factors are also estimated as described in chapter 2. For the application of the sediment budget model on the Rhine catchment we did an additional adjustment to the R factor in order reduce biases in soil erosion rates and to better test the performance of the model as a whole. When using climate data of MPI-ESM, we found that the R values for the Rhine catchment are overestimated by a factor of 5, compared to the modelled R values from observed climate data for present day. This is due to strong overestimation in precipitation rates for West-Europe by MPI-ESM. Therefore, we introduced a correction factor based on the R values calculated from observational datasets for the period 1950-2000AD. This adjustment is not performed for the global application of the model. Furthermore, due to the overestimation of erosion rates by the adjusted RUSLE model in the Alps, we defined a mean soil erosion rate of $20\,\mathrm{t\,ha^{-1}\,year^{-1}}$ for this region based on high resolution erosion data from (Bosco et al., 2008). For the global application we fixed the maximum soil erosion rates to $50\,\mathrm{t\,ha^{-1}\,year^{-1}}$.
Furthermore, we chose the floodplain deposition fraction to range between 0.5 and 0.8 for natural landscapes that consist out of mainly forest, and between 0.2 and 0.5 for agricultural lands. According to Eq.(3.5), f increases exponentially with slope. Based on this we calculated a_f and b_f to be respectively 0.5 and 0.47 for natural landscapes and 0.2 and 0.917 for agricultural land. This means that for low slopes ($<\pm 0.2\,\%$) in a natural landscape an equal amount of sediment is deposited in the floodplain as on the hillslope, while for agricultural land only 20 % of the eroded soil from the hillslope will reach the floodplain.
The floodplain residence time is made to range between the median and maximum residence time of floodplain sediment in the Rhine catchment of respectively 260 and 1500 years (personal communication with Dr.T.Hoffmann). Wittmann and von Blanckenburg (2009) found a residence time of 600 years for floodplain sediments at Rees in the Rhine catchment, which falls in the range of the floodplain residence times of our study. According to Eq.(3.3), τ increases exponentially with flow-accumulation. As the maximum flow-accumulation is different for different catchments, we used the maximum

flow-accumulation of a continent to determine the a_τ and b_τ (Eq.3.3) for catchments in that continent. The exact values for a_τ and b_τ are given in Appendix A.2.
Finally, to get accurate flow directions we used the digital elevation model (DEM) and flow-accumulation on 30 arcsec from the HydroSHEDS (Hydrological data and maps based on SHuttle Elevation Derivatives at multiple Scales) database (Lehner et al., 2006). The HydroSHEDS DEM is based on SRTM and GTOPO30 data. The HydroSHEDS flow-accumulation data for the Rhine catchment was aggregated to 5 arcmin, and the inverted upscaled flow-accumulation values were then used as input for the multiple flow routing scheme. It should be mentioned that using a coarser resolution DEM for the sediment routing results in strongly biased flow directions.

3.2.3 Criteria for model evaluation

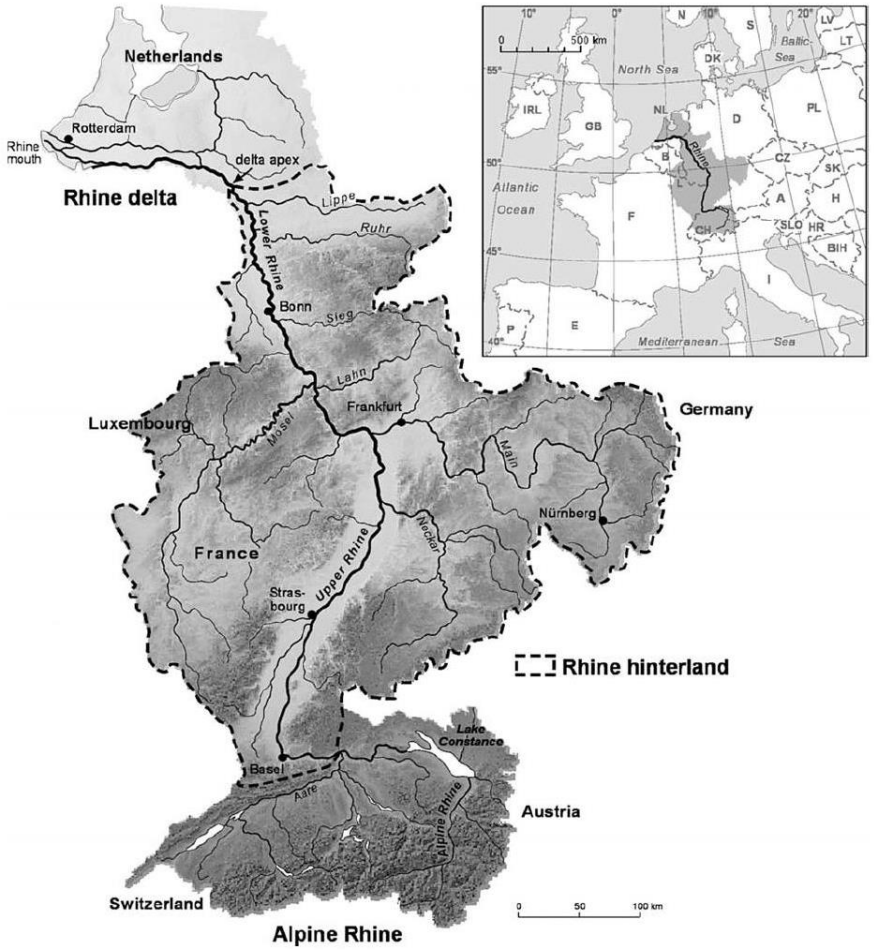

Figure 3.2: The Rhine catchment (Hoffmann et al., 2013)

A large-scale spatial model like the one we presented is difficult to validate due to the lack of large-scale and long-term observational data. Hoffmann et al. (2013) compiled published data on sediment storage for regions in Central Europe, mainly for the Rhine

catchment, where human induced soil erosion took place in the past 7500 years. Combined with a long land use history, where agricultural activities go back till about 7500 years ago (Houben et al., 2006; Hoffmann et al., 2007), the Rhine catchment serves as a good case study to investigate the impact of human activities on erosion and sediment yields through history. The Rhine catchment (Fig. 3.2) has a size of ($\sim 185000\,\mathrm{km}^2$) with a main river channel length of ($\sim$ 1320) km and drains large parts of the area between the European Alps and the north sea. It has a complex topography where the elevation ranges between -180 and 1967 m with a mean topographical percent slope of 0.07, where percent slopes can go up to 1.2. It consists out of two large sedimentary catchments (ie, upper Rhine Graben and the lower Rhine Embayment-Southern North Sea Basin) that serve as large floodplain sinks for sediment, and some upland areas, such as the Black Forest and the European Alps that serve as major sediment production areas.

From the observed sediment storage Hoffmann et al. (2013) derived scaling relationships between storage S ($10^9\,\mathrm{kg} = 1\,\mathrm{Mt}$) and catchment area A (km^2) for floodplains and hillslopes. They found that for floodplains the sediment storage increases exponentially with catchment area, while hillslope sediment storage shows a different behavior and increases almost linear with catchment area. The scaling relationships, given by Eq.(3.11) for hillslopes and Eq.(3.12) for floodplains, will be used as the main validation for our sediment budget model.

$$S = (364 \pm 168)10^6 (A/A_{ref})^{(1.06\pm0.07)} \tag{3.11}$$

$$S = (184 \pm 24)10^6 (A/A_{ref})^{(1.23\pm0.06)} \tag{3.12}$$

Here, A_{ref} is an arbitrary chosen reference area, in this case $10^3\,\mathrm{km}^2$. The observation data contains 41 hillslope and 36 floodplain sediment storage values, derived from a large number of auger and bore holes that are used to measure sediment thickness related to human induced soil erosion.

Furthermore, Hoffmann et al. (2007) established a Holocene sediment budget for sediments in the floodplains and the delta of the non-Alpine part of the Rhine catchment. They derived sediment thickness of Holocene deposits from borehole data that consists out of 563 drillings and available geological maps. This was then multiplied with floodplain areas to calculate floodplain volumes. Sediments on hillslopes were not addressed in this study. A total floodplain sediment mass of $53.5 \pm 12.4 \times 10^9$ t was found for the whole Rhine catchment, of which 50 % is stored in the Rhine Graben and the delta. The spatial variability of the observed sediment storage will be a second validation test for out model.

Finally, Hoffmann et al. (2007) found an average erosion rate of $0.55 \pm 0.16\,\mathrm{t\,ha^{-1}\,year^{-1}}$ for the last 10000 years, with extreme minimum and maximum values of 0.3 and $2.9\,\mathrm{t\,ha^{-1}\,year^{-1}}$. However, Hoffmann et al. (2013) included also hillslope sediment

storage and calculated a total sediment storage of 126 ± 41 Gt for the Rhine catchment, which requires a minimum Holocene erosion rate of approximately $1.2 \pm 0.32\,\mathrm{t\,ha^{-1}\,year^{-1}}$. This shows that hillslopes are not only the main sources of eroded sediment but can be major millennial-scale sinks for eroded sediment from agriculture. We will compare erosion rates for the Rhine catchment from our sediment budget model also with the above presented values from the studies of Hoffmann et al. (2007) and Hoffmann et al. (2013).

3.2.4 Simulation setup

In order to model the sediment storage for a certain catchment, an initial state has to be assumed. Here we assume the initial state to be the equilibrium state of a catchment, defined as the state of a catchment where the sediment input is equal to the sediment output, and thus the sediment yield at the outlet of the river should be constant in time. External forces working on a catchment such as land use activities or deglaciation can bring the catchment out of equilibrium in a transient state. In the case of the Rhine catchment the period directly after the Last Glaciation Maximum (LGM) could be of importance due to strong erosion that was triggered by the retreating ice sheets. From today's observations on sediment budgets or erosion rates we cannot determine when the Rhine catchment was in an equilibrium state. Additionally, there are no observations of sediment storage before the start of agricultural activities in the Rhine catchment, which date back to 7500 years ago. This poses a problem in simulating and interpreting the present-day absolute values of sediment storage and yields with our sediment budget model.
In order to still being able to interpret the simulated sediment storage for the Rhine catchment and globally, we will not focus on the absolute values of sediment storage. We will only focus on the change in sediment storage due to land use and climate change since 850AD. An exception is made in section 3.3.2.4, where we will use the absolute values of simulated sediment yields, and not the change during the last millennium, to validate the sediment budget model with observed yields on a global scale. Considering mainly the changes induced by external forcing, it is not necessary to know if the system was in an equilibrium or transient state at 850AD. Based on this reasoning, we take the environmental conditions of 850AD to determine the equilibrium state of the model.
In the rest of this study, we will refer to 850AD as the 'default equilibrium state' that we define based on the mean climate and land cover conditions at 850AD, while one should keep in mind that this is not the 'real' equilibrium state of the catchment. 850AD is used here as the equilibrium state due to reasons related to data availability, and because human impact in this time period is still small compared to present day. Hence, our simulation setup structure is generally defined by an equilibrium simulation based on the conditions of 850AD, followed by a transient simulation for the last millennium (850-2005AD).

We used climate and land cover data from different simulations of MPI-ESM that were

Table 3.1: Simulation specifications for the application of the sediment budget model for the Rhine catchment and globally. For each experiment with the sediment budget model the type of simulation (equilibrium or transient), the time period, and the initial conditions on which the simulation is based on, are given. Furthermore, we also provide the number of simulations we made with the model for a certain type of simulation, and the experiment from MPI-ESM that we used to derive the input data to force the sediment budget model.

Application	Experiment	Simulation	Time period	Initial conditions	Experiment MPI-ESM-LR	number of simulations
Rhine-cathment		equilibrium		850-950AD	last millennium	1
		equilibrium		6000 BP	mid-Holocene	2
	default	transient-part1	850-1850AD	850-950AD	last millennium	1
	default	transient-part2	1850-2005AD	transient-part1	historical	3
	default	transient-part1	850-1850AD	6000 BP	last millennium	2
	default	transient-part2	1850-2005AD	transient-part1D	historical	2
	climate change	transient-part1	850-1850AD	850-950AD	last millennium	1
	climate change	transient-part2	1850-2005AD	transient-part1	historical	1
	land use change	transient-part1	850-1850AD	850-950AD	last millennium	1
	land use change	transient-part2	1850-2005AD	transient-part1	historical	1
Global		equilibrium		850-950AD	last millennium	1
	default	transient-part1	850-1850AD	850-950AD	last millennium	1
	default	transient-part2	1850-2005AD	transient-part1	historical	1
	climate change	transient-part1	850-1850AD	850-950AD	last millennium	1
	climate change	transient-part2	1850-2005AD	transient-part1	historical	1
	land use change	transient-part1	850-1850AD	850-950AD	last millennium	1
	land use change	transient-part2	1850-2005AD	transient-part1	historical	1

available from the CMIP5 experiment to force the sediment budget model. For the global application of the sediment budget model we performed one equilibrium simulation based on the mean climate and land cover conditions of the period 850-950AD from the last millennium experiment of the MPI-ESM. For the Rhine catchment we performed three equilibrium simulations, one based on the mean climate and land cover conditions of the period 850-950AD, and the two others based on the mean climate and land cover conditions of the mid-Holocene period (6000 years ago) from the mid-Holocene experiment of the MPI-ESM (Table 3.1). The reason for performing an equilibrium simulation for the mid-Holocene period is to investigate how different initial conditions for climate and land cover would influence the overall sediment storage change during the last millennium. In the equilibrium simulations the erosion and deposition rates are kept constant and the model is run with a yearly time step till the total floodplain sediment storage of a catchment does not change more than 1 ton per year.

The floodplain and hillslope sediment storage at equilibrium were then used as a starting point for the transient simulation that covers the period 850 - 2005AD. In the transient simulation erosion and deposition rates are averaged over time steps of 100 and 50 years, based on the time resolution of the rainfall erosivity factor (R) that is part of the erosion module.

For the global application we performed three main transient simulations, to investigate the individual contribution of land use change and climate change on sediment storage (Table 3.1). In the 'default' transient simulation both land cover and climate

were variable throughout the last millennium. In the climate change simulation we kept the land cover conditions fixed to the period 850-950D throughout the last millennium, while in the land use change simulation we kept the climate conditions fixed to the period 850-950D.
For the Rhine catchment we performed 5 'default' transient simulations, two based on the mid-Holocene equilibrium states, and three others based on the equilibrium state of the period 850 - 950AD. The different ensemble simulations were used to investigate the uncertainty in the resulting sediment storage due to the input data of MPI-ESM. Additionally, we also performed a climate change and land use change simulation based on the equilibrium state of the period 850 - 950AD (Table 3.1).

3.3 Results and discussion

3.3.1 The Rhine catchment

3.3.1.1 Scaling test

In order to validate the sediment budget model we tested if the model can reproduce the scaling relationships found by Hoffmann et al. (2013) for the non-Alpine part of the Rhine catchment (Eq.3.11 and 3.12). For this we chose the grid cells in the Rhine catchment that correspond to the observation points from Hoffmann et al. (2013). Observation points that fell outside the Rhine catchment, were not considered. When considering only the selected grid cells and applying the same scaling approach as in the study of Hoffmann et al. (2013), we found an average scaling exponent for floodplains of 1.2 ± 0.04 and for hillslopes of 1.05 ± 0.07 (Table 3.2). These values fall in the range of floodplain and hillslope scaling exponents of 1.23 ± 0.06 and 1.08 ± 0.07 respectively found by Hoffmann et al. (2013). The uncertainty in the scaling exponents is mainly due to the regression, while the uncertainty due to different ensemble simulations is very small (Table 3.2). Our model also reproduces the characteristic differences in scaling between floodplains and hillslopes as found by Hoffmann et al. (2013) (Fig. 3.3a and b). One should note that the grid resolution of the model limits the prediction of sediment storage to grid points with a catchment area $\geq 10^2\,\mathrm{km}^2$.
When considering all the grid cells of the Rhine catchment we derived a scaling exponent for floodplain storage of 1.33 ± 0.02, (Table 3.3), which is somewhat higher than the value found when only the selected grid cells are used. This may be due to the inclusion of grid cells that lie in the Alpine region of the Rhine catchment. Including the Alpine region leads then to a stronger gradient in sediment storage and catchment area between the Alps and the Rhine delta. In the Alpine region the model predicts much less sediment storage due to the low residence time and high sediment connectivity, while for the Rhine delta the sediment storage is large due to the high flow-accumulation and high residence times. For hillslope storage the scaling exponent

(a) Floodplains

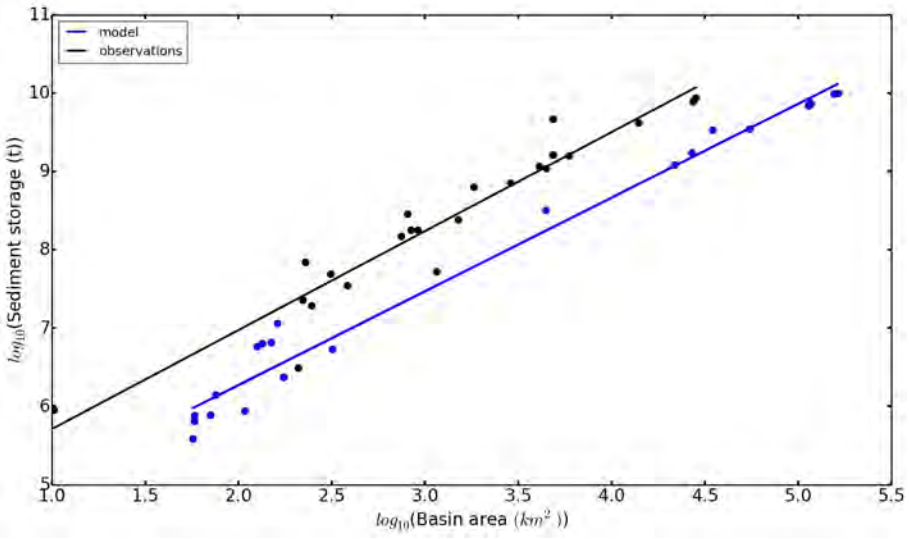

(b) Hillslopes

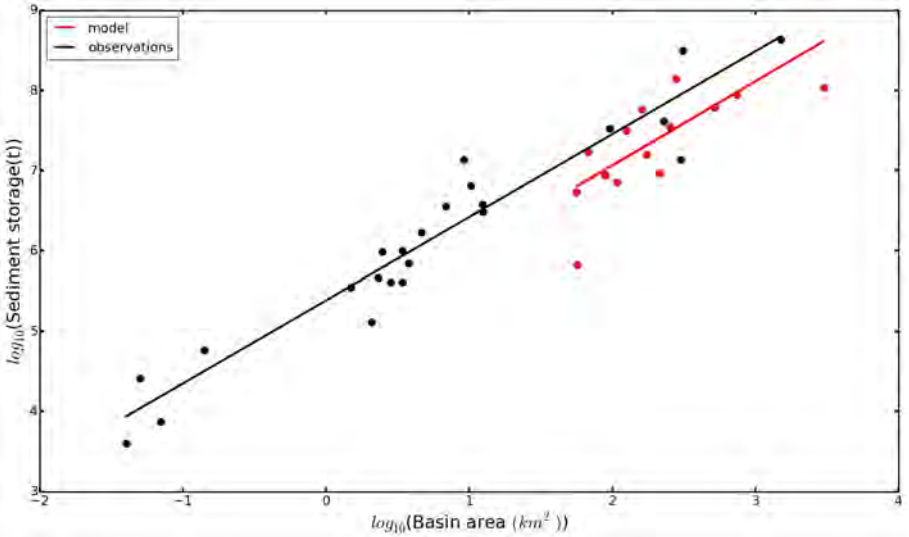

Figure 3.3: Scaling of floodplain (a) and hillslope (b) sediment storage from the transient simulation in the non-Alpine part of the Rhine catchment. The black dots and black trend line correspond to the observed sediment storage values from Hoffmann et al. (2013). The blue dots and blue trend line correspond to modelled sediment storage values that correspond to the observation points from Hoffmann et al. (2013) and fall into the borders of the Rhine catchment.

is also slightly higher when including all grid cells in the scaling approach (Table 3.3). This can also be explained by including the Alpine region, where the model predicts more sediment storage on hillslopes, compared to the rest of the Rhine catchment due to the high erosion rates in this region.
Furthermore, when including all grid cells in the scaling approach there is more spread in the data, which is clear from the lower r-value of the regression. The small difference

between the scaling exponents when considering all grid cells and the scaling exponents when considering only selected grid cells indicates that the selected observation points from Hoffmann et al. (2013) are robust and representative for the catchment. The relatively small difference can be partly attributed to biases in simulated erosion and deposition rates and the floodplain residence times.

Table 3.2: Summary of regression results of sediment storage scaling at the end of the equilibrium and transient simulations. Here we consider only the grid cells that correspond to the observation points from Hoffmann et al. (2013) and fall into the borders of the Rhine catchment. The r-value is the Pearson correlation coefficient, and the slope and intercept are the scaling parameters.

	Floodplains			Hillslopes		
	slope	intercept	r-value	slope	intercept	r-value
Equilibrium	1.659 ± 0.037	3.123 ± 0.130	0.99	1.085 ± 0.060	6.429 ± 0.180	0.94
Transientensemble1	1.198 ± 0.038	3.877 ± 0.133	0.98	1.050 ± 0.064	4.963 ± 0.193	0.93
Transientensemble2	1.202 ± 0.038	3.853 ± 0.133	0.98	1.048 ± 0.065	4.971 ± 0.194	0.93
Transientensemble3	1.203 ± 0.038	3.85 ± 0.133	0.98	1.048 ± 0.065	4.972 ± 0.194	0.93
Hoffmann et al. (2013)	1.230 ± 0.060	4.450	0.96	1.080 ± 0.070	5.380	0.96

Table 3.3: Summary of regression results of sediment storage scaling after the equilibrium and transient simulations. Here we consider all grid cells in the Rhine catchment area. The r-value is the Pearson correlation coefficient, and the slope and intercept are the scaling parameters.

	Floodplains			Hillslopes		
	slope	intercept	r-value	slope	intercept	r-value
Equilibrium	1.685 ± 0.015	2.827 ± 0.039	0.80	1.118 ± 0.016	6.327 ± 0.040	0.62
Transient ensemble 1	1.330 ± 0.017	3.406 ± 0.042	0.67	1.111 ± 0.015	4.741 ± 0.039	0.63
Transient ensemble 2	1.332 ± 0.017	3.401 ± 0.042	0.67	1.112 ± 0.015	4.740 ± 0.039	0.63
Transient ensemble 3	1.332 ± 0.017	3.400 ± 0.042	0.67	1.112 ± 0.015	4.741 ± 0.039	0.63

Finally, we found that keeping either the climate or land cover constant throughout the last millennium had very little impact on the scaling exponent for floodplains. Here, the climate change simulation resulted in a slightly higher and the land use change simulation in a slightly lower scaling exponent. The different forcings had a stronger impact on the scaling for hillslopes, as hillslope sediment storage is only dependent on erosion and deposition rates. For the climate change simulation the scaling exponent for hillslopes increased by 3.8 %, while for the land use change simulation a small decrease of 0.1 % was found. This decrease could result from the fact that most land use change took place in the lower parts of the Rhine catchment resulting in an increased sediment storage there. In contrast, the conditions in the Alpine region did not change that rapidly, resulting in a decreased difference in sediment storage on hillslopes between the upper and lower areas in the catchment.

The above results indicate that the scaling relationships are a general feature for the entire Rhine catchment and are independent of the selected observation points. As the

Rhine catchment is a large catchment with a complex topography, this result indicates that the scaling relationships might be also applicable for other large river catchments.

3.3.1.2 Origin of scaling between sediment storage and catchment area

We also performed a sensitivity study to test the robustness of the scaling relationships of the model. For this we investigated the dependence of the scaling on the three main variables of the model, namely, the residence time, erosion and deposition. First, we investigated the dependence of the scaling exponent of floodplains on the residence time. To do this we chose different median residence times of floodplain sediment in the Rhine catchment, while keeping the maximum residence time fixed. Changing the median residence time by a factor of 10, from 50 to 500 years, results in a decrease of 21.8 % in the scaling exponent for floodplain storage for the transient simulation (Table 3.4). When the median floodplain residence time is increased, the range in the residence time decreases. This leads to less difference between grid cells with small and large catchment areas in terms of the sediment loss, and consequently to a decrease in the scaling exponent. We found that when the residence time is increased by 5.2 % (from 50 to 260 years) the scaling exponent decreases by 18.2 %, while an increase in the residence time of 1.9 % (from 260 to 500 years) results only in a decrease of the scaling exponent of 4.4 %. This indicates that the scaling exponent of floodplain storage does not change linearly with the residence time, and points out that the model shows a non-linear behavior. The equilibrium simulation shows the same behavior for the scaling exponent when the residence time is changed. However, here the 10 fold change in the residence time leads to a slightly larger change in the scaling exponent.
Next, we investigated the dependence of the scaling exponents of floodplains and hillslopes on erosion. We substituted the correction factor for the R values (see section 3.2.2) by a non-constant variable, which changed the spatial distribution of erosion in the Rhine catchment. We estimated this correction factor by dividing the R values based on data from MPI-ESM by the R values based on observational datasets. The new correction factor increased the R values in the Alpine region and decreased the R values in the rest of the catchment. This resulted in a larger difference between the sediment storage in small catchment areas and sediment storage in large catchment areas. Although the resulting scaling exponent for floodplains was still much higher than the scaling exponent for hillslopes, both scaling exponents increased significantly. For the deposition we found a minor to neglecting effect on the scaling parameters.
Overall we found that changing erosion and residence time does not change the basic property of the scaling, which is that floodplain storage grows strongly with catchment area while hillslope storage shows a linear scaling with catchment area. As the residence time is determined by flow-accumulation and flow-accumulation determines the spatial variability of floodplain sediment storage, we expect that the scaling parameters of floodplain sediment storage are also mainly determined by flow-accumulation. Erosion is mainly determined by the slope, and slope determines the spatial variability of

hillslope sediment storage. We expect, therefore, that the slope determines the scaling parameters of hillslope sediment storage. Based on this we speculate that the scaling for both floodplain and hillslope storage is an emergent property of the model and that the scaling parameters are controlled by the underlying topography.

Table 3.4: Summary of regression results of the sensitivity analysis on floodplain sediment storage scaling. Here we consider only the previously mentioned selected grid cells in the Rhine catchment area. The r-value is the Pearson correlation coefficient, and the slope and intercept are the scaling parameters.

	slope	intercept	r-value
Equilibrium			
τ median = 50 years	1.787 ± 0.041	2.143 ± 0.143	0.99
τ median = 260 years	1.659 ± 0.037	3.123 ± 0.130	0.99
τ median = 500 years	1.616 ± 0.037	3.496 ± 0.128	0.99
Transient			
τ median = 50 years	1.464 ± 0.055	2.59 ± 0.193	0.97
τ median = 260 years	1.198 ± 0.038	3.877 ± 0.133	0.98
τ median = 500 years	1.145 ± 0.035	4.128 ± 0.122	0.98

3.3.1.3 Last millennium sediment storage change

We estimated an average soil erosion rate of $2.8 \pm 0.002\,\mathrm{t\,ha^{-1}\,year^{-1}}$ for the last millennium (850 - 2005AD) for the entire Rhine catchment. We find that this value is twice as high as the $1.2 \pm 0.32\,\mathrm{t\,ha^{-1}\,year^{-1}}$, which was estimated as the minimum average soil erosion rate for the Holocene by Hoffmann et al. (2013).
The average soil erosion rate for the last millennium resulted in a mean floodplain and hillslope sediment storage change of 11.95 ± 0.01 and 29.68 ± 0.03 Gt, respectively, for the last millennium (Table 3.5). Altogether, floodplain and hillslope storage result in 41.63 ± 0.02 Gt of sediment, which can be considered as the contribution of climate and land use change to sediment storage in the last millennium. It is, however, hard to say what the range in the change of sediment storage should be for this period, as there are no related studies for this specific time period. Hoffmann et al. (2007) found a total sediment storage of 126 ± 41 Gt for the Holocene in the Rhine catchment. Our values are lower than this range found by Hoffmann et al. (2007), due to the fact that we only consider the impact of last millennium on the sediment storage and not the last 7500 years. Our results show that the sediment storage of the last millennium form 25 to 50 % of the total sediment storage of the last 7500 years. This indicates that the average sediment storage rate during the last millennium is higher than the average rate during the last 7500 years. This supports the findings from previous studies (Bork, 1989; Notebaert et al., 2011), which show that land use change has a significant and long-term impact on erosion and sediment mobilization.

Table 3.5: Summary of sediment storages M (Gt), erosion (E) and deposition (D) rates in $t\,ha^{-1}\,year^{-1}$, and the related uncertainty ranges for the Rhine catchment for the period 850-2005AD. The uncertainty values represent the range in the mean values due to different ensemble simulations.

	Mean M	Ensemble uncertainty M	Mean E	Ensemble uncertainty E	Mean D	Ensemble uncertainty D
Floodplains	11.95	0.01	2.787	0.0015	1.296	0.0005
Hillslopes	29.68	0.03	2.787	0.0015	1.491	0.0015
Whole Rhine catchment	41.63	0.02	2.787	0.0015	2.787	0.0015

Furthermore, Hoffmann et al. (2013) found a floodplain to hillslope ratio of about 0.88, indicating that during the Holocene more sediment was stored on hillslopes than in floodplains. We find with our model a floodplain to hillslope ratio of about 0.46, confirming that more sediment is stored on hillslopes.
We also analyzed the spatial variability of the modelled sediment storage, and found that the model reproduces the spatial variability well when compared to the observed values from Hoffmann et al. (2007) for the Holocene (Fig. 3.4). Here we found a correlation coefficient of 0.76, where sediment storage in floodplains increased with the catchment area. Furthermore, we found that most floodplain sediment is stored in the Mosel sub-catchment, in contrast to the observations that show that most of the sediment is stored in the Upper-Rhine sub-catchment (Table 3.6). This can be related to the fact that different dynamical processes play a role in the Upper-Rhine catchment, which are triggered by the Alps. Melting ice sheets for example can produce a lot of erosion that is not captured by our model and in this way the total stored sediment in the catchment could be underestimated. Furthermore, the Mosel sub-catchment has a highly complex topography, which can indicate that our sediment budget model is too coarse for an accurate representation of floodplain storage for this catchment.
For hillslope sediment storage we found a similar spatial trend as for the floodplain sediment storage, with some more variation between the minimum and maximum values (Table 3.6).

Also here, the Mosel catchment has the most sediment stored. Furthermore, when comparing floodplain to hillslope sediment storage we find that the floodplain to hillslope ratio varies significantly between the various sub-catchments. The highest ratio of 0.48 is found for the Lower Rhine sub-catchment, while the lowest ratio of 0.14 is found for the Emscher sub-catchment. The ratios seem not to be correlated with slope or catchment area and can be assumed as independent features of the model.

The sediment budget model presented here, has been developed to simulate long-term historical trends and to determine the main drivers behind these trends. Figure 3.5 shows the land use change and the 10 year-mean precipitation timeseries averaged over the Rhine catchment for the last millennium. There are two interesting periods, respectively, 1350-1400AD and 1750-1950AD that show increased precipitation amounts correlating with a sudden increase in land use change (increase in crop and pasture). Both periods lead to maxima in the erosion timeseries of $2.8\,\mathrm{t\,ha^{-1}\,year^{-1}}$

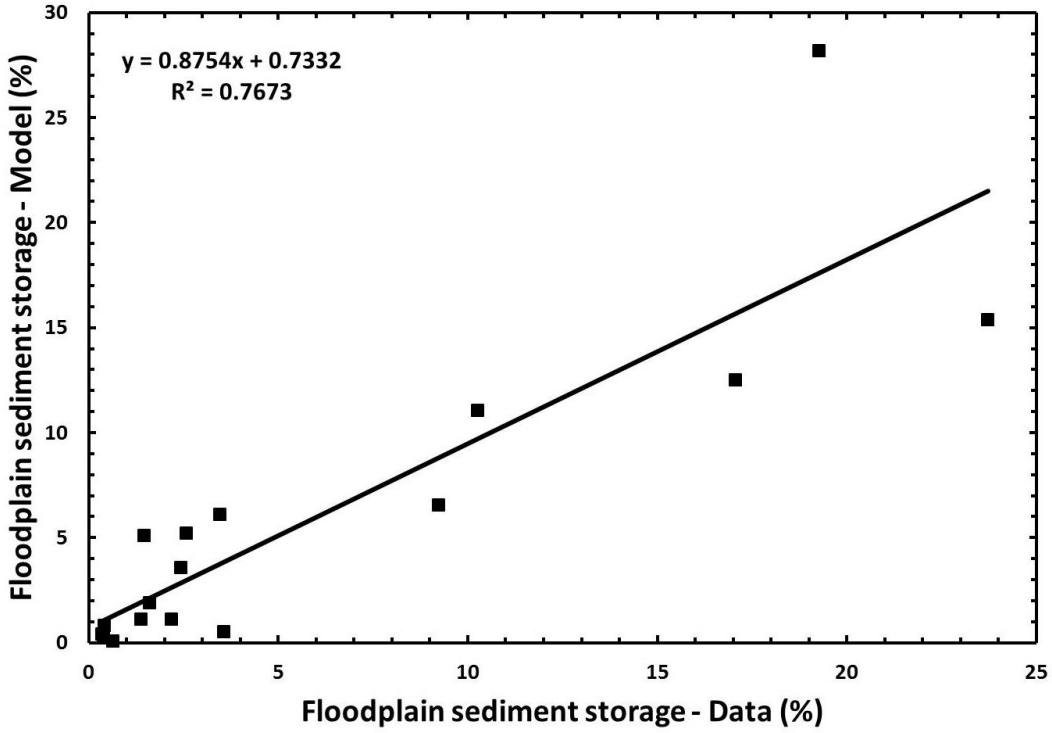

Figure 3.4: Observed versus modelled relative floodplain sediment storage change for Rhine sub-catchments. The observed sediment storage change is with respect to 7500 years ago, while the modelled sediment storage change is with respect to 850AD. Data on the observed sediment storage is taken from Hoffmann et al. (2007).

Table 3.6: Observed versus modelled sediment storage change (Gt) for Rhine sub-catchments. The catchment area is given in km^2. Data on the observed sediment storage is taken from Hoffmann et al. (2007).

Catchment	Catchment area	Observed floodplain storage	Modelled floodplain storage	Modelled hillslope storage
Lippe	4858	1.62	0.03	0.07
Lower Rhine	404	0.99	0.07	0.14
Emscher	806	0.29	0.005	0.03
Ruhr	4477	1.10	0.21	0.68
Wupper	838	0.18	0.02	0.06
Erft	1819	0.63	0.07	0.22
Sieg	2870	0.73	0.11	0.38
Lahn	5916	1.57	0.36	1.15
Wied	745	0.16	0.02	0.13
Ahr	911	0.19	0.05	0.15
Middle Rhine	1046	0.66	0.30	0.87
Main	27307	7.75	0.73	2.66
Mosel	28227	8.75	1.64	4.93
Nahe	4070	1.17	0.30	1.11
Upper Rhine	3006	10.77	0.90	2.69
Neckar	13971	4.19	0.38	1.93
Ill	4858	4.66	0.65	2.28

and $4.3\,t\,ha^{-1}\,year^{-1}$, respectively (Fig. 3.6a and 3.6b). This corresponds to increased erosion rates during the 14th and 18th century found by (Bork, 1989; Lang et al., 2003)

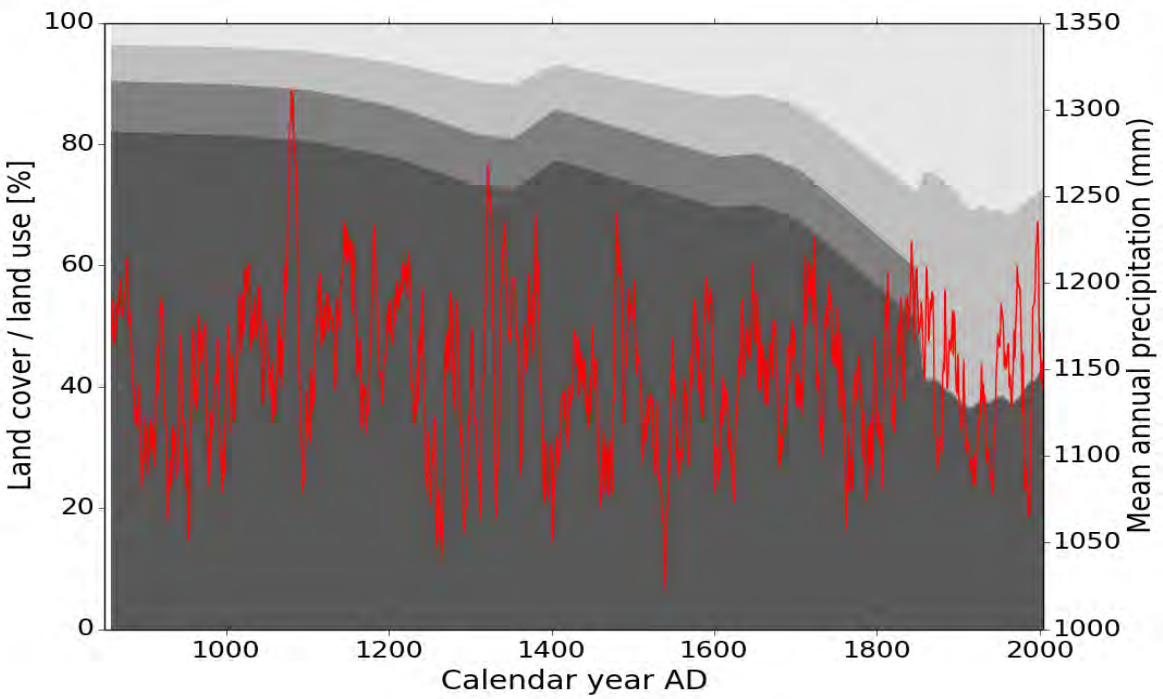

Figure 3.5: Land cover and precipitation variability averaged over the Rhine catchment for the last millennium. The red line is the 10 year mean total precipitation for the Rhine catchment. The background colors are land cover types, starting from the darkest grey to the lightest: forest, bare soil, grass, crop and pasture. Land cover and precipitation data is from MPI-ESM.

for Germany.

We find the strongest increase in the sediment storage rate for floodplains during the period 1750-1850AD, while for hillslopes during the period 1850-1950AD. For hillslopes this maximum sediment storage rate corresponds to a maximum increase in the deposition rate, which is a result of a maximum increase in land use change and a high erosion rate.

Land use change leads to a sediment disconnectivity in the landscape, which prevents the sediment stored on hillslopes of reaching the fluvial system on the timescale of the last millennium. In contrast to hillslopes, the maximum sediment storage rate for floodplains is a result of the interplay between deposition and sediment loss from the catchment. In the period 1750-1850AD land use change started to increase in the Alpine region, which did not experience such a strong change in land-use as the lower parts of the catchment before this time period. During this period, the deposition to floodplains increased significantly due to the increased erosion rates as a result of land use change. Also, land use change started to impact the Alpine region, where areas with steep slopes and short residence times lead to a strong sediment flux downstream. However, due to the long residence time of the areas located downstream, the sediment loss from the catchment did not increase as much, leading to an increased sediment

storage in the floodplains. This is in accordance with the findings of Asselman et al. (2003), who found that due to an inefficient sediment delivery, an increase in soil erosion in the Alps will have a little effect on sediment load downstream the Rhine catchment. Furthermore, if we disentangle the effects of land use and climate on the sediment storage for floodplains and hillslopes, we can see that land use change explains most of the change in sediment storage. For floodplains climate change also has a non-negligible impact on the temporal variability of sediment storage. For example in the periods 1350-1400AD and 1750-1950AD, the sediment storage rate is increased due to increased precipitation that leads to a strong sediment flux downstream from upstream areas. If the land use change conditions of the period 850 and 950AD were kept constant, the total change in sediment storage in floodplains and hillslopes during the last millennium would be 2.9 and 15.4 Gt, respectively. This is four and two times, respectively, less than the change in floodplain and hillslope sediment storage when land use change is variable (Fig. 3.7a and 3.7b). When the land cover is kept constant, the overall sediment storage still increases for the climate change scenario due to the overall increased trend in precipitation during the last millennium. If only the climate change conditions are kept constant, the resulting change in sediment storage in floodplains and hillslopes would be 10 and 27.4 Gt, respectively.

(a) Floodplains

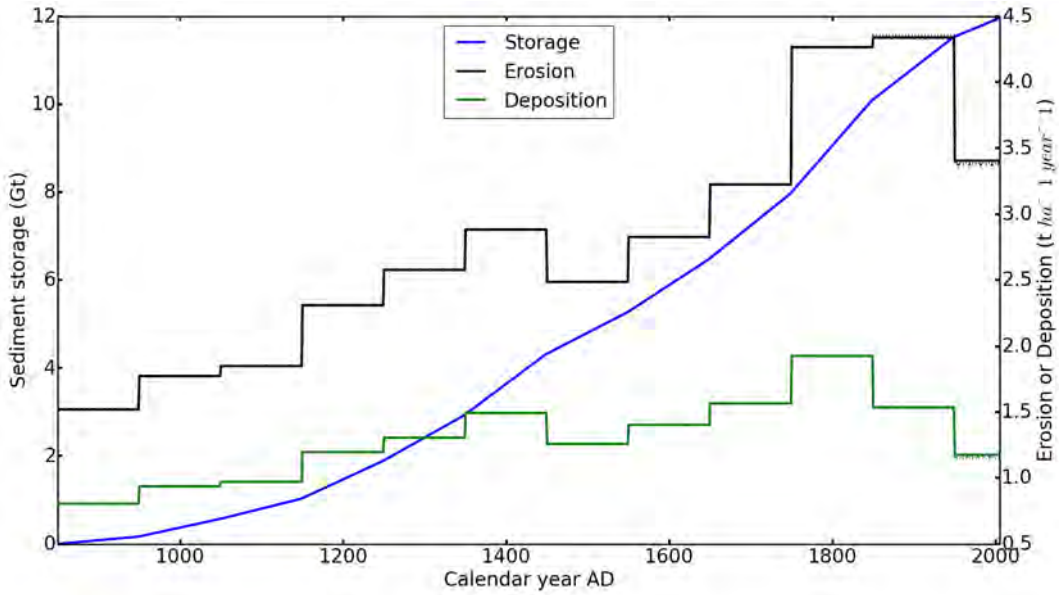

(b) Hillslopes

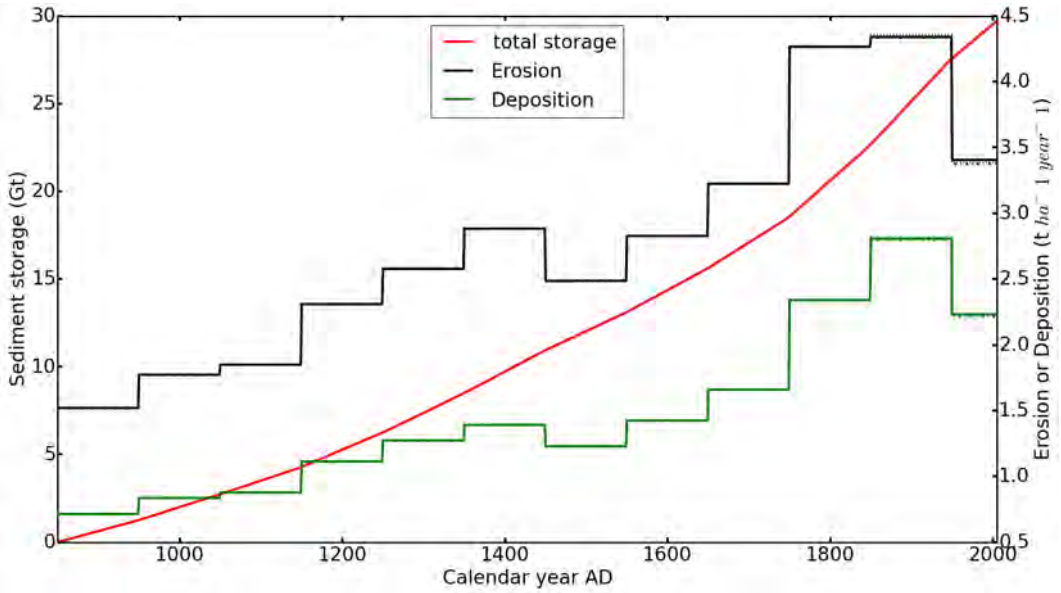

Figure 3.6: (a) Timeseries of simulated average erosion (black line), average deposition (green line) and the total change in sediment storage (blue line) with respect to 850AD for floodplains in the last millennium in the Rhine catchment. (b) Timeseries of simulated average erosion (black line), average deposition (green line) and the total change in sediment storage (red line) with respect to 850AD for hillslopes in the last millennium in the Rhine catchment.

(a) Floodplains

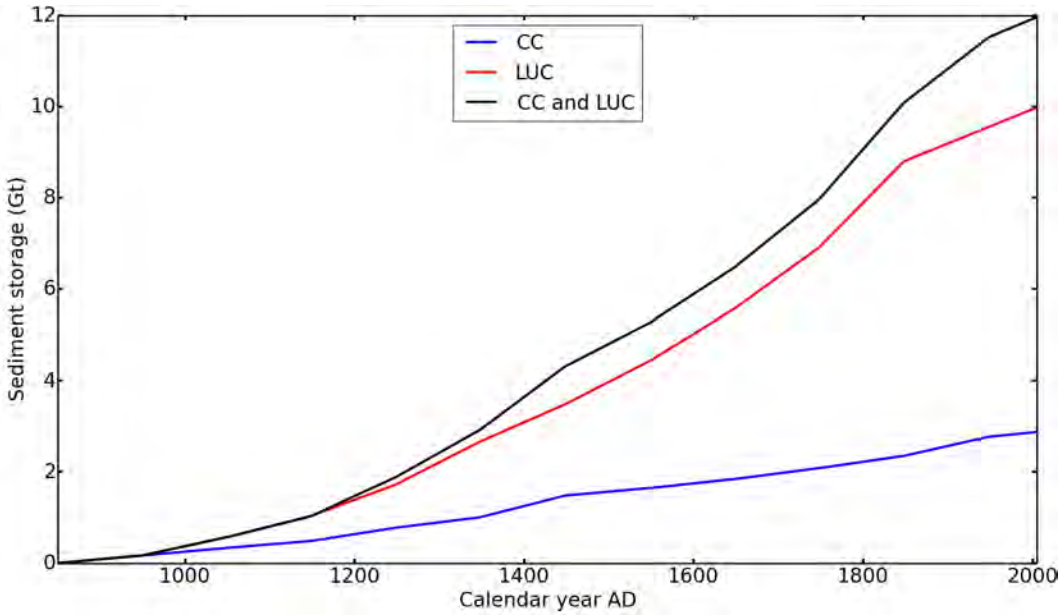

(b) Hillslopes

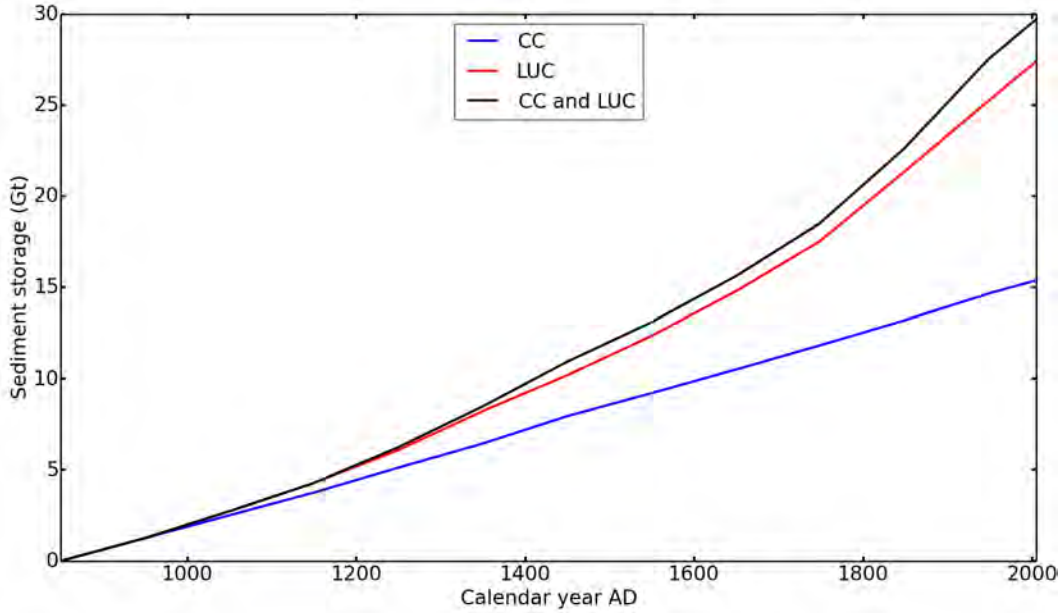

Figure 3.7: Simulated change in (a) floodplain and (b) hillslope sediment storage for the Rhine catchment during the last millennium. Shown are the sediment storage for the climate change scenario, where land cover is set to the conditions of the period 850-950AD (CC - blue line), the sediment storage for the land use change scenario, where the climate is set to the conditions of the period 850-950AD (LUC - red line), and the sediment storage where both climate and land cover change during the last millennium (CC and LUC - black line).

3.3.1.4 Uncertainty assessment

As shown in the previous sections, the average erosion rate for the Rhine catchment is found to be overestimated when compared to the erosion rate for the Holocene from the study of Hoffmann et al. (2013). As we consider in this study only the last millennium, where human impacts through land use change are strongest pronounced, it is logical that our estimated average soil erosion rate is higher. For present day, we found an average soil erosion rate of $3.3\,\mathrm{t\,ha^{-1}\,year^{-1}}$ for the non-Alpine part of the Rhine catchment, which is also overestimated when compared to other studies. Cerdan et al. (2010) found for the non-Alpine part of the Rhine catchment a value of $1.5\,\mathrm{t\,ha^{-1}\,year^{-1}}$, while Auerswald et al. (2009) found for Germany a value of $2.7\,\mathrm{t\,ha^{-1}\,year^{-1}}$.
Comparing the spatial variability of erosion rates for present day with the high resolution estimates from Cerdan et al. (2010), we find that erosion is overestimated for the whole Rhine catchment. We expect that the overestimation in the modelled erosion rates is mainly due to uncertainties related to the coarse input datasets on climate and land cover, and biases in the adjusted RUSLE model.
As discussed before, precipitation is overestimated by MPI-ESM for the Rhine catchment. Even after introducing a correction factor, which partly adjusted the R value estimation to values from observational datasets, biases related to the R factor remain. Additionally, coarse resolution land cover fractions and LAI from MPI-ESM also affect the total erosion rates. Using coarse resolution data to calculate the C factor of the adjusted RUSLE model results in discrepancies between the C and S factors. For example, consider a large grid cell with a complex topography where cropland is allocated in flat areas and forest in the steeper areas. Even though the C factor is calculated correctly as combination of cropland and forest fractions, it is applied to the whole grid cell. This leads to an overestimation of erosion rates for flat areas, as erosion is in the first order controlled by the slope through the S factor. We attempted to correct this by introducing slope classes for each coarse grid cell with resolution of MPI-ESM (1.875 degrees). The cropland was then allocated to the flatter areas, while in the steeper areas more of the other land cover types was allocated. However, this only had a minor effect on the overall erosion rates, indicating that this is not the major source for the overestimated erosion rates.
Neglecting the support practice (P) and slope-length (L) factors also affect the erosion rates as described in chapter 2. As the Rhine catchment has a long land use history, land management strategies were implemented historically, to decrease soil erosion rates. We partly captured the effects of land management in the C factor, however, we expect that introducing the P and L factors in the model will reduce the soil erosion rates in cropland.
Finally, biases in the adjusted RUSLE model, such as the unadjusted C and K factors and the low performance of the model in mountainous areas, have an equally important effect on the total erosion rates.
Another large uncertainty in our sediment budget model, besides the biases in erosion

rates, is the choice of the equilibrium state. We found a decreasing trend in the floodplain sediment storage in the transient simulation when using the equilibrium state based on the mean conditions of 6000 BP. This can be attributed to the different spatial distribution of erosion and the average high erosion rate for the mid-Holocene of $7.8\,\mathrm{t\,ha^{-1}\,year^{-1}}$. When switching from the equilibrium state to the transient state, the erosion rates drop and the spatial distribution changes significantly. This leads to a decreased sediment flux from upstream areas and overall decreased sediment production rates that result in a drop in sediment storage in the floodplains. For the hillslopes we found that the equilibrium state has minimal to no influence on the total sediment storage for the last millennium.
The initial conditions determine the amount and spatial distribution of erosion in the catchment during the time that the model runs to equilibrium. Therefore, the equilibrium state that is then reached, largely determines the spatial distribution, trend, and amount of the sediment storage during the transient period.
Finally, the different ensemble simulations for the period 1850-2005AD do not differ strongly in precipitation and land cover/land use change, and therefore do not contribute much to the uncertainty in the overall erosion rates and sediment storage. This period is also too short to find significant effects on the sediment storage from different ensemble simulations.

3.3.2 Global application

3.3.2.1 Scaling test

For the global application of the sediment budget model we chose to investigate 20 large river catchments spread over different regions in the world (Table 3.7). The main reason behind the choice of these catchments, is the fact that they belong to the largest catchments of the world. This is important in order to minimize biases due to the structure of our model that operates on a coarse resolution and uses coarse resolution input data from ESMs. Also, it facilitates our aim, which is to capture the large-scale variability in sediment storage and yields. Additionally, we made sure that we include catchments with a strong human impact and others that are more or less in a pristine condition. Finally, for a global assessment we chose catchments from all continents of the world, with different underlying environmental parameters such as climate, topography, soils, and vegetation.

For each of the catchments we performed the same scaling exercise as for the Rhine catchment, including all grid cells in a catchment in the analysis of the scaling parameters. Table 3.8 shows the results for the scaling parameters for hillslopes and floodplains for each catchment. We found that the scaling exponent for floodplains varies between 1.41 and 1.81 with an average r-squared value of 0.92. For hillslopes we found that the scaling exponent ranges between 1.0 and 1.32 with an average r-squared value of 0.83. The high r-squared values show that the scaling relationships are valid

Table 3.7: Selected global river catchments and their properties. The climate is divided into the following types (1) polar: Tmean $< 0°C$, (2) cold temperate: $0 \leq$ Tmean $< 10°C$ and latitude > 30 degrees, (3) warm temperate: $10 \leq$ Tmean $< 25°C$ and latitude > 30 degrees, (4) tropics: latitude < 30 degrees. Here, 'Tmean' is the catchment average temperature. 'Land use 850AD' is the percentage area of the catchment classified as crop and pasture in the year 850AD, as simulated by MPI-ESM. 'LUC strength' is the increase in crop and pasture area during the last millennium as percentage of the total catchment area.

Catchment	Continent	Climate	Land use 850AD (%)	LUC strength (%)	Catchment area (km^2)	Mean slope ($m\ km^{-1}$)
Amazon	South-America	tropical	0.31	9	5912482	40
Congo	Africa	tropical/warm temperate	1.36	14	3705035	30
Mississippi	North-America	warm/cold temperate	0.01	74	3179211	33
Nile	Afric	tropical	3.85	35	2916242	39
Parana	South-America	warm temperate/tropical	0.06	45	2593919	28
Niger	Africa	tropical	2.93	39	2098311	16
Ganges	Asia	warm temperate/tropical	12.25	35	1574326	137
Volga	Europe	cold temperate	2.54	50	1404073	28
Nelson	North-America	cold temperate	0	51	1004359	36
Orinocco	South-America	tropical	0.04	25	938370	57
Danube	Europe	cold temperate	11.25	47	786434	81
Murray-Darling	Australia	warm temperate	0.48	49	774914	28
Mekong	Asia	tropical	2.29	19	774141	92
Yellow	Asia	cold temperate	6.4	53	761182	65
Ob	Asia	cold temperate/polar	0.88	22	704370	37
Mackenzie	North-America	cold temperate/polar	0	11	596699	90
Dnieper	Europe	cold temperate	3.62	67	509776	0.9
Don	Europe	cold temperate	3.58	82	437290	15
Rhine	Europe	cold temperate	5.79	44	163029	99
Elbe	Europe	cold temperate	5.37	46	138370	28

for all the catchments. The results of the scaling exponents indicate that the scaling behavior between sediment storage and catchment area are indeed a global feature. Although, we found for the Rhine catchment that for hillslopes the sediment storage scales linearly with catchment area, the global analysis for hillslopes indicates that this relationship can change to a power relationship in certain cases. However, we noticed that if the sediment storage increases stronger with catchment area for hillslopes, this will be also the case for floodplains. In this way sediment storage in floodplains always increases stronger with catchment area compared to sediment storage on hillslopes.
We also derived the overall global scaling exponents considering each of the selected river catchments as a whole catchment rather than a collection of grid cells. We found a scaling exponent of 1.46 ± 0.26 for floodplains with an r-squared value of 0.64, and a scaling exponent of 1.22 ± 0.21 for hillslopes with an r-squared value of 0.66 (Fig. 3.8a and 3.8b). For floodplains there are clearly two outliers, the Dnieper and the Don catchments which can be considered as flat catchments and show a lower gradient in sediment storage between small and large sub-catchments in the respective catchments.

To investigate why the scaling properties differ between the catchments and why in some cases the sediment storage does not scale linearly with catchment area for hillslopes, we group the catchments based on their relief and catchment area. The classification is described in figure 3.14 in section 3.3.2.3.

We find for small flat areas the lowest scaling exponents on average (1.58 for floodplains and 1.1 for hillslopes), as expected, due to the high residence time of floodplain sediment

(a) Floodplains

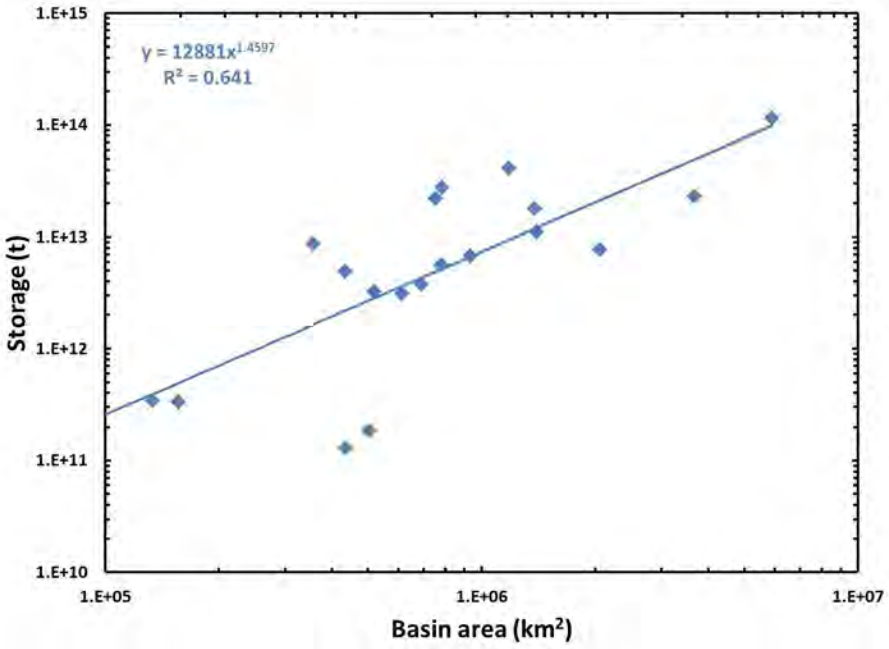

(b) Hillslopes

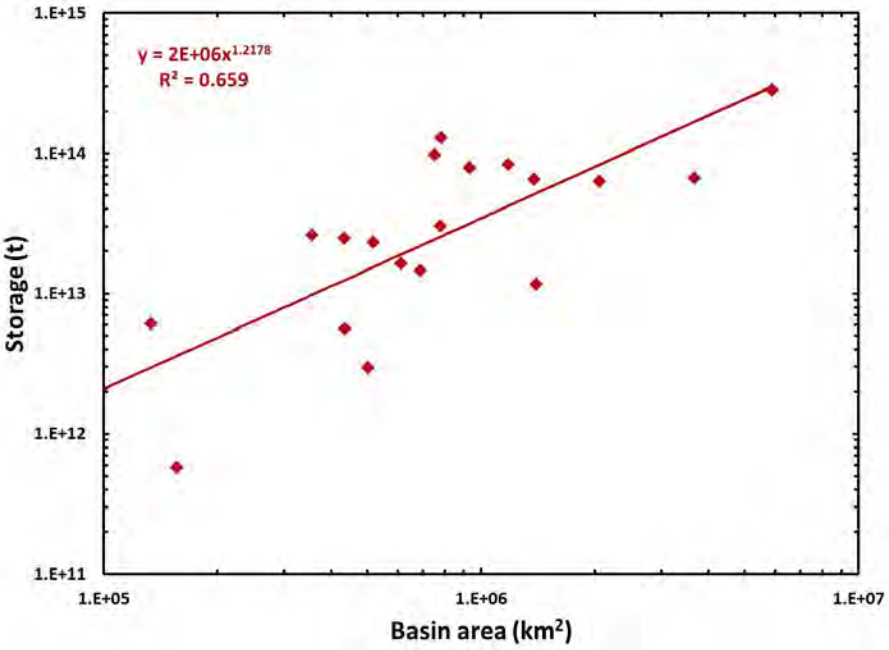

Figure 3.8: Scaling relationships between sediment storage and catchment area for (a) floodplains and (b) hillslopes, using selected global catchments.

and lower sediment connectivity. The largest scaling exponents we find for small steep areas (1.68 for floodplains and 1.16 for hillslopes), which have in general better sediment connectivity. We find not much difference in the scaling exponents between small steep catchments or large steep catchments. This is partly due to the fact that we have only

Table 3.8: Parameters of the scaling relationships between catchment area and sediment storage for floodplains and hillslopes for selected global catchments. The r-value represents the Pearson correlation coefficient, and the slope and intercept are the scaling parameters.

	Floodplains			Hillslopes		
Catchment	exponent	intercept	r-value	exponent	intercept	r-value
Amazon	1.67	2.62	0.94	1.13	6.88	0.87
Congo	1.56	2.80	0.95	1.07	6.78	0.86
Mississippi	1.53	3.27	0.95	1.07	7.28	0.90
Nile	1.81	1.94	0.84	1.32	5.86	0.64
Parana	1.59	2.81	0.92	1.09	6.97	0.83
Niger	1.61	2.47	0.89	1.09	6.50	0.68
Ganges	1.61	3.67	0.84	1.16	7.10	0.70
Volga	1.54	2.85	0.96	1.04	6.73	0.92
Nelson	1.65	2.43	0.93	1.13	6.53	0.87
Orinoco	1.75	2.80	0.92	1.16	7.20	0.86
Danube	1.65	3.16	0.93	1.13	7.06	0.88
Murray-Darling	1.70	2.37	0.93	1.15	6.72	0.85
Mekong	1.77	2.87	0.91	1.23	6.68	0.82
Yellow	1.64	3.39	0.89	1.18	7.15	0.81
Ob	1.75	2.28	0.90	1.22	5.98	0.81
Mackenzie	1.78	2.58	0.88	1.19	6.61	0.78
Dnieper	1.42	2.96	0.98	1.02	6.52	0.91
Don	1.41	3.02	0.97	1.00	6.98	0.93
Rhine	1.52	4.16	0.95	1.09	7.80	0.89
Elbe	1.62	3.33	0.93	1.13	7.16	0.88

one large steep catchment, but it could also indicate that the catchment area is of lesser importance than the relief or steepness of the landscape for the scaling relationships. The catchments for which storage on hillslopes does not scale linearly with catchment area are usually small steep catchments such as the Yellow catchment, or large flat catchments such as the Nile catchment. Again, this is strongly related to the sediment connectivity in a catchment and the spatial variability of slopes. To have a nonlinear scaling relationship between sediment storage and catchment area for hillslopes, it is required that a lot of sediment is stored in small steep areas, while less sediment is stored in large flat areas. This can happen if agriculture for example is abundant in steeper areas, trapping a large part of the eroded sediment on the hillslopes and reducing the sediment connectivity in the catchment. Most of the catchments that show a nonlinear scaling relationship for hillslopes have abundant land use change and a strong land use history (Yellow, Nile, Mekong catchments). However, sediment can also be trapped on hillslopes in small catchments when the topography is very complex and reduce the sediment connectivity.

3.3.2.2 Last millennium sediment storage change

Figure 3.9 shows the mean erosion rates during the last millennium, while figure 3.10 shows the resulting sediment storage change during the last millennium for the selected global catchments. We find that the Ganges catchment has the highest mean erosion rate of about 16.8 t ha^{-1} year^{-1}, and also the highest total sediment storage of 1777 Gt. However, we can see that high mean erosion rates do not always lead to a large sediment storage change and otherwise, a large sediment storage change is not always a result of high erosion rates. This is due to the fact that sediment storage is a result of a combination of factors such as, the extend of the catchment area, the complexity of topography and the intensity of external forces such as land use change or climate change.

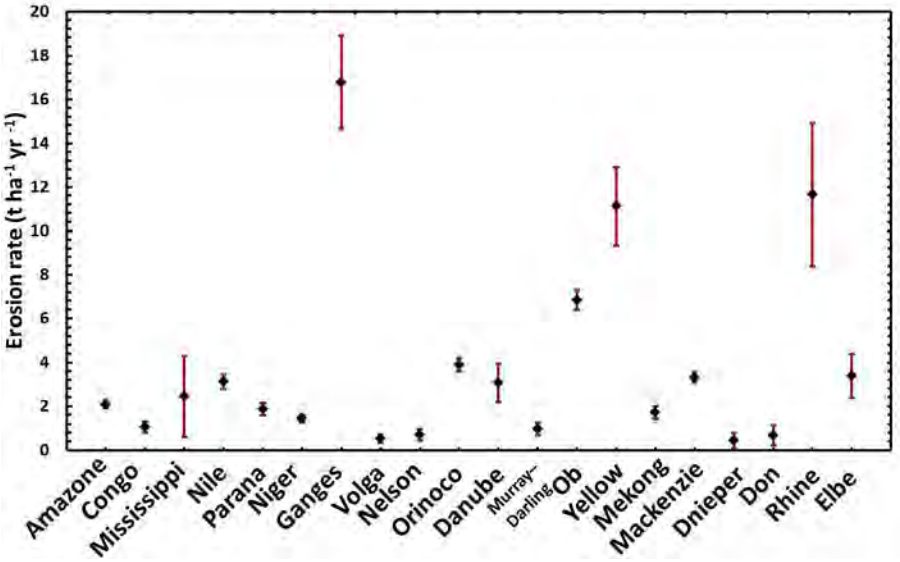

Figure 3.9: Catchment mean soil erosion rates averaged over the last millennium for selected global catchments. The uncertainty in the erosion rates (red bars) are due to different ensemble simulations of the MPI-ESM.

We find that for most catchments land use change is the main driver behind the change in sediment storage (Fig. 3.12). For example, land use change explains most of the sediment stored in the Ganges catchment, leading to increased sediment storage on hillslopes and in floodplains during the last millennium (Fig. 3.11). Although, the erosion rates in this catchment are naturally high due to the steep topography and intense precipitation, human activities have strongly accelerated these erosion rates across the whole catchment. In combination with a large catchment area, accelerated erosion rates resulted in the large change in hillslope and floodplain sediment storage during the last millennium.
For a small percentage of the catchments climate change plays an equal or even larger role as land use change in explaining the total change in sediment storage during the last millennium (Fig. 3.12). A clear example is the Amazon catchment, which has

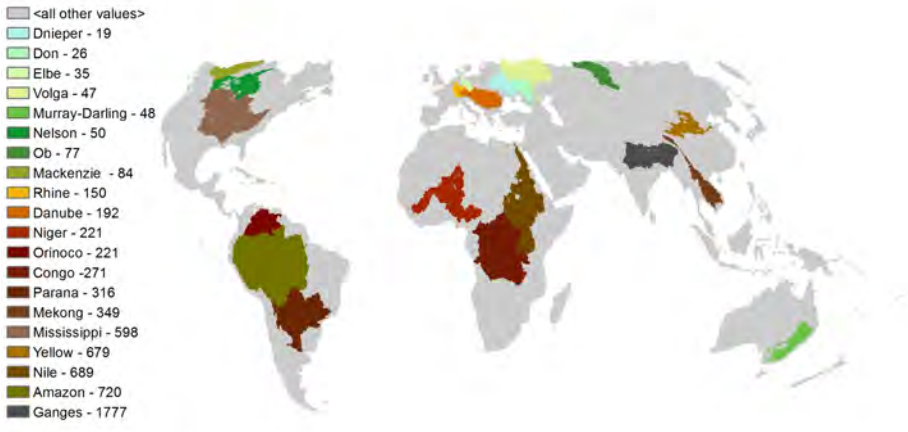

Figure 3.10: The total change in sediment storage (Gt) during the last millennium for selected global catchments.

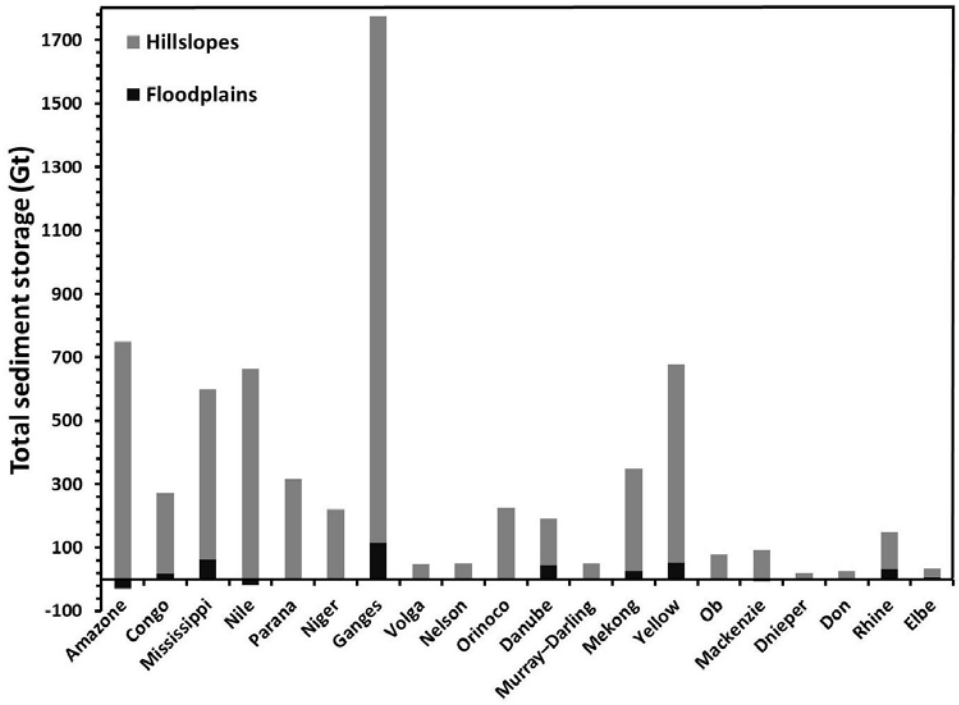

Figure 3.11: Total sediment storage change in floodplains (black) and on hillslopes (gray) during the last millennium for selected global basins.

the second largest total sediment storage of 720 Gt (Fig. 3.10 and 3.11). The large change in sediment storage is mainly due to the fact that the Amazon catchment has the largest catchment area globally. The high precipitation rates in the tropics and the mountainous area in the west of the catchment add to this large amount of sediment storage. The land use change, however, plays a much less important role here. Figure 3.12 shows that climate change results in more sediment storage than land use change

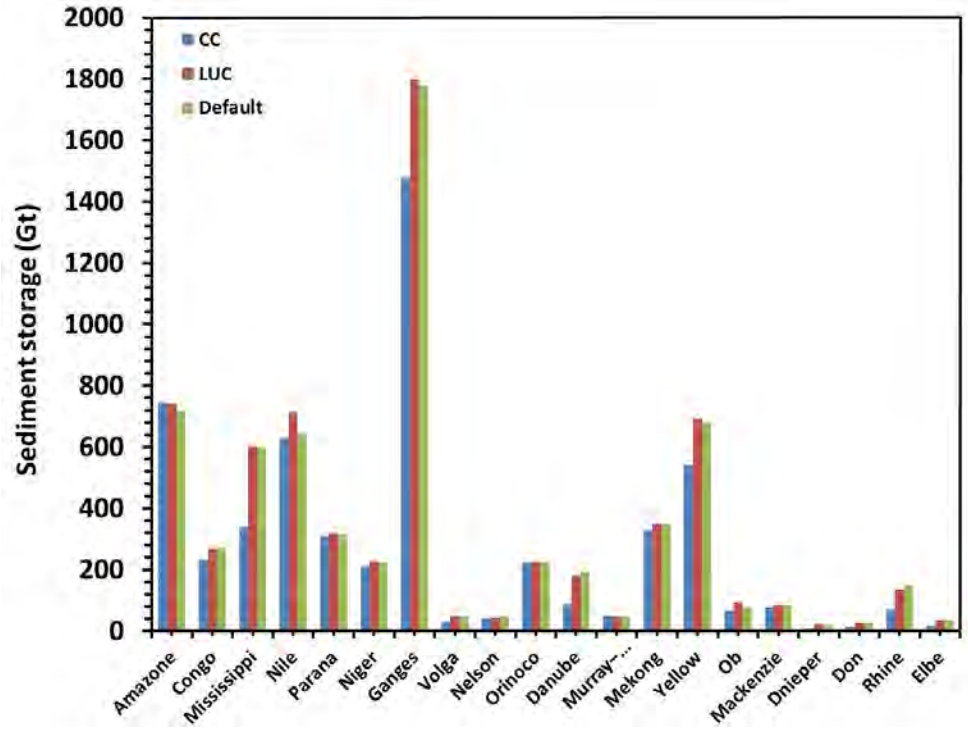

Figure 3.12: Total sediment storage change due to climate change only (blue), due to land use change only (red), and due to climate and land use change (green) during the last millennium for selected global catchments.

in this catchment, confirming that climate change explains most of the sediment storage. Figure 3.11 shows that the total sediment storage in floodplains of the Amazon during the last millennium decreased (negative values) compared to the year 850AD, which indicates that the overall erosion rates during the last millennium decreased. This decreased erosion is due to the decrease in precipitation and at the same time the absence of significant land use change till some few centuries ago.

It should be noted that the results we found are also dependent on the way climate and land cover is simulated by MPI-ESM. For example, erosion rates are sensitive to the climate and land cover data as has been shown in chapter 2.

As we found that land use change is the main driver behind the change in sediment storage for most catchments, we investigated how the land use change strength effects the sediment storage in the catchments. We defined the land use change strength in a catchment as the total increase of crop and pasture area relative to the total area of a catchment. The land use change strength during the last millennium for the different catchments is given in table 3.7.

We found no significant correlation between the land use change strength in the catchments and the sediment storage change per unit area. We expect this to be due to the influence of catchment characteristics, such as slope, sediment connectivity, climate and the spatial distribution of land use in a catchment. For example, land use change intensifies most on areas with low slopes. On the one hand, low slopes result in lower

sediment production by erosion and thus a lower sediment storage overall. On the other hand, sediment storage increases if land use change intensifies. However, this intensification is again dependent on the slope, as steep slopes are stronger affected by land use change in comparison to low slopes. Furthermore, sediment connectivity plays an important role in the transport of the stored sediment to the outlet of the basin (Hoffmann, 2015; Gumiere et al., 2011). If the sediment connectivity is high, land use change intensification will not have a strong impact on the change in sediment storage, but rather on the sediment yield. Additionally, the spatial distribution of land use is also essential in buffering or intensifying the effects of land use on sediment storage. If land use takes place on steep slopes this can result in substantial erosion and subsequently in more sediment storage depending on the sediment connectivity of a catchment. Finally, all these effects could be buffered or intensified by climate change. To see if we can still find a signal between the land use change strength and the sediment storage, we look at the ratio of sediment storage versus total erosion. This makes it possible to partially get rid of the effects of slope mentioned before. By doing this we find a significant increasing trend in the ratio of sediment storage versus erosion with increasing land use change strength (Fig. 3.13). This shows that overall more sediment is stored relative to the total erosion in a catchment if the land use change intensifies. This relation can be strengthened or weakened depending on the catchment characteristics such as slope, sediment connectivity, climate and the spatial distribution of land use.

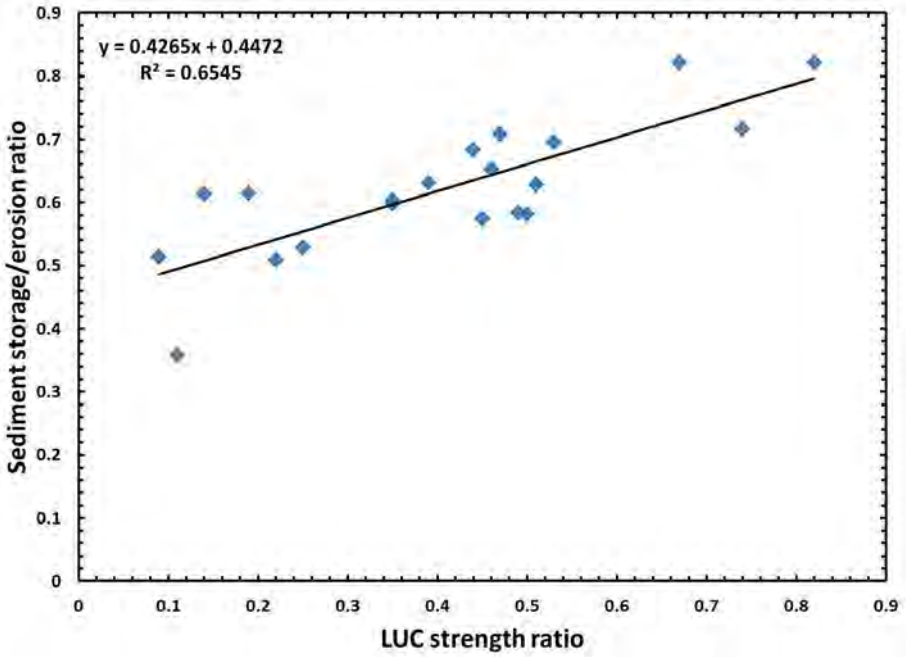

Figure 3.13: The ratio between sediment storage and erosion versus the land use change (LUC) strength for the selected global river catchments.

3.3.2.3 Catchment characteristics

As seen in the previous section, catchment characteristics play an important role in buffering or amplifying the change in erosion due to climate change or land use change on the resulting sediment storage.
Therefore, we investigated the dependence of sediment storage on catchment characteristics, such as the mean topographical slope and catchment area. For this purpose we classified the catchments based on the mean slope and total catchment area, according to Syvitski et al. (2003). When the area of a catchment is equal or larger than 10^6 km^2 the catchment is classified as large, otherwise the catchment is classified as small. When the mean slope of a catchment is equal or larger than 5 percent, the catchment is classified as steep, otherwise the catchment is classified as flat.
Although, we investigate only 20 catchments, of which only one catchment falls into the category of large and steep catchment, we find that catchments with a small area and steep slopes show a comparable sediment storage as catchments with a large area and low slopes (Fig. 3.14). This can be explained by the fact that slope mainly controls the rate of sediment storage, while catchment area controls the total sediment storage (Appendix A.2). This indicates that low slopes usually encompass large areas that can result in an equal or even larger total soil erosion and related sediment storage in comparison to steep areas. This is in accordance with the findings of Syvitski et al. (2003) and Willenbring et al. (2013), where they show similar results for sediment yields and the total sediment production by denudation.

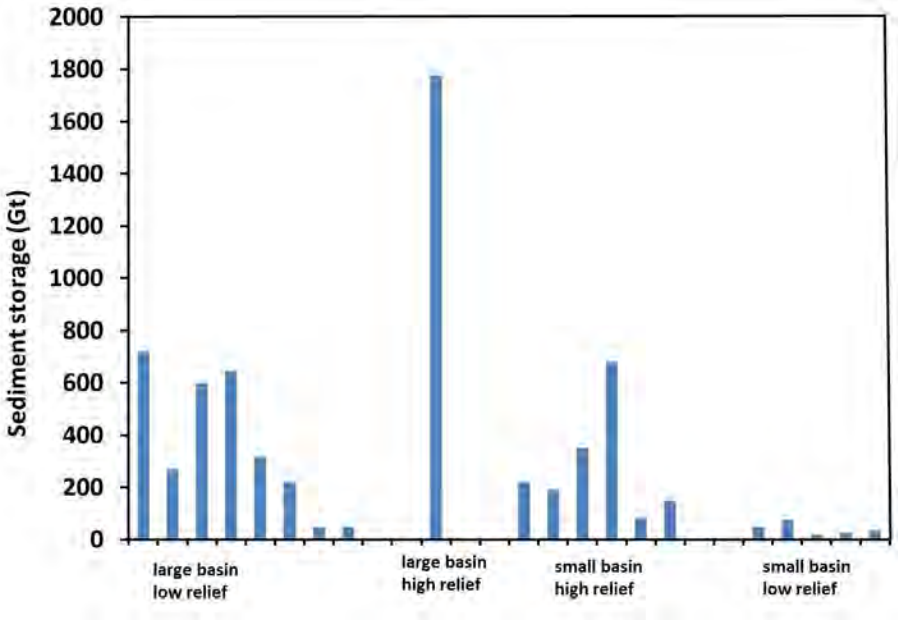

Figure 3.14: Sediment storage categorized based on the catchment properties area and relief. Small & flat: area $< 10^6$ km^2 and slope $< 5\%$, small & steep: $area < 10^6$ km^2 and slope $\geq$ 5 %, large & flat: area $\geq 10^6$ km^2 and slope $< 5\%$, large & steep: area $\geq 10^6$ km^2 and slope $\geq$ 5 %.

3.3.2.4 Comparison to observed sediment yields

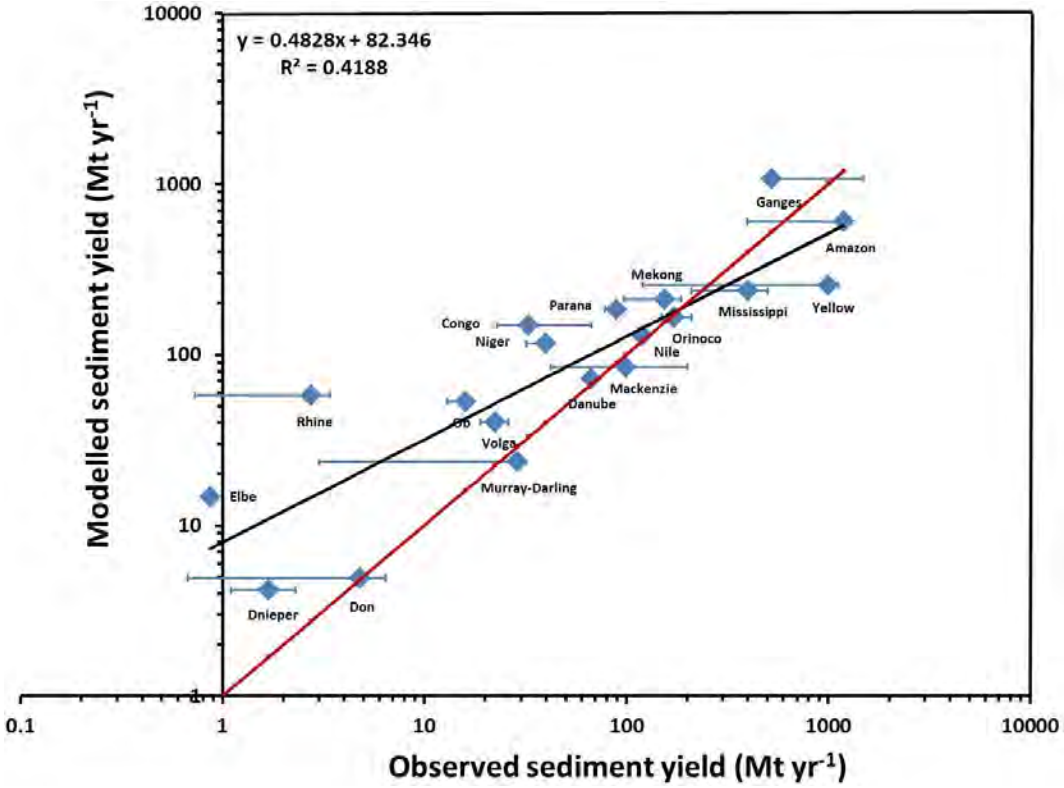

Figure 3.15: Present day observed versus modelled sediment yields for the selected global catchments. The horizontal bars respresent the uncertainty range in observed sediment yields from the Land2Sea database (Peucker-Ehrenbrink, 2009). The red line is the 1 to 1 line, and the black line is the trend line.

It is difficult to validate the model on global scale due to the absence of data on sediment storage globally. One possible way to investigate if the model shows a valid behavior is to compare the modelled sediment yields to observed suspended sediment yields from global rivers. It should be noted however, that a fair comparison is not possible here as the equilibrium state in the model is based on the conditions of 850AD and we only model sediment redistribution during the last millennium. In order to be able to derive the real sediment yields we need to look at a much longer period, and we need to know approximately when and if the different river catchments were in an equilibrium state. As this is currently not feasible we instead investigate if the global variability in modelled large scale sediment yields is in the right order.
For this, we used the Land2Sea database (Peucker-Ehrenbrink, 2009) which provides data on the sizes of 1519 exorheic river drainage catchments (79 % of the exorheic land area), annual suspended sediment fluxes (593 rivers, 63 % of the exorheic land area), and water discharges (1272 rivers, 76% of the exorheic land area) that have been compiled from a variety of sources. We compare here our modelled sediment yields from the default scenario with predam estimates (Fig. 3.15).

We find that our model generally overestimates the sediment yields when compared to the observed median sediment yields from the Land2Sea database (Fig. 3.15). The overestimation of sediment yields by our model is, first of all, a result of the fact that we used the conditions from the period 850-950AD as an equilibrium state in the model. As in this period land use change already started in most catchments (Table 3.7), the modelled sediment yields will be usually higher than normal. For example, in the Ganges catchment where land use change already occupied 12% of the total area around 850AD, the sediment yield is significantly overestimated by the model.
Secondly, overestimation of erosion rates by the adjusted RUSLE model in mountainous regions also contribute to the overestimation of sediment yields from steep catchments, such as the Ganges and the Rhine catchments.
Thirdly, the sensitivity of the erosion rates and resulting sediment dynamics to the climate and land cover data from MPI-ESM, significantly affects the overall sediment yields. For example, we find a strong underestimation of the sediment yield for the Amazon catchment by the sediment budget model, although, the land use was minimum in 850AD and the catchment is for a large part flat. We expect this underestimation to be a result of the underestimation in precipitation by MPI-ESM (Joetzjer et al., 2013). The other example is the Rhine catchment, discussed in the previous sections, where the precipitation rates are overestimated by MPI-ESM, resulting in high erosion rates and an overestimated sediment yield. This is also the case for the Elbe catchment, as these catchments have a similar climate. For the African catchments, such as the Congo and Niger, we also find overestimated sediment yields by the sediment budget model. Although, observations on sediment yield (Peucker-Ehrenbrink, 2009) and erosion (Stocking, 1984) show that these parameters are quite low for these catchments due to the low relief. We expect that the overestimated erosion rates and the resulting sediment yields in these catchments are due to the high precipitation rates simulated by MPI-ESM (Mehran et al., 2014).
Another possible reason for the biases in sediment yields is the fact that the parameters of the sediment budget model are calibrated based on data from the Rhine catchment. The Rhine catchment can be categorized as a warm temperate region. This can lead to biases for catchments with different environmental parameters, such as catchments with a different climate.
Furthermore, although, we find a low correlation (correlation coefficient of 0.42) between the modelled and observed median sediment yields, the correlation is significant (Fig 3.15). This indicates that the sediment budget model is capable of reproducing the spatial variability in sediment yields for large catchments globally. One should notice that the range in observed sediment yields for several catchments (Amazon, Yellow, Mississippi, Ganges) is quite large. When we compare the minimum observed sediment yields with our estimates we find an improved correlation coefficient of 0.8. When we compare our estimates to the maximum observed sediment yields we find an even more improved correlation with a coefficient of 0.9. This indicates that it is hard to compare the modelled yields with the observed ones due to the large uncertainty in observed

sediment yields.
Finally, we found that the contribution of climate and land use change during the last millennium has a minimal effect on the total sediment yield in the catchments we investigated. This is mainly due to the long residence time of sediment in floodplains, which is especially true for large catchments with a low relief. These large catchments thus buffer the effect of land use change on the sediment yield. Additionally, land use change results in more sediment storage on hillslopes than in floodplains, leading to a reduced sediment yield on the timescale of the last millennium. This result is in accordance with the findings of Syvitski et al. (2005), where they pointed out that humans have increased the sediment transport by global rivers, but reduced the flux of sediment reaching the world's coasts.
Furthermore, the change in sediment yield at the outlet of the catchments is an interplay between the intensity of land use or climate change and the sediment connectivity. The catchments for which we found a clear increase in sediment yield during the last millennium are the Congo, Mekong, Yellow, Elbe and Ganges catchments. It is difficult to disentangle the effect of climate or land use change and the sediment connectivity on the sediment yield change. However, for all the catchments with a significant change in sediment yield the land use change plays an important role. Combined with a good sediment connectivity this leads to a substantial change in sediment yields during the last millennium.

3.3.3 Limitations of the modelling approach

Firstly, the model is designed to simulate large-scale sediment fluxes and its spatial variability, and not to calculate the exact sediment storage values and sediment yields on a local scale. Due to this fact, and the fact that spatial resolution of input data on climate and land cover on centennial to millennial timescales is coarse, the model is limited to catchments larger than 100 km^2.
Secondly, the current setup of the model is limited in estimating sediment storage for a few thousands of years. This is due to the fact that the residence time does not change with time in our model. In reality, the residence time should change temporarily due to changes in the surface slope after sediment redistribution. We assume in our model that the changes to the surface slope on the timescale of the last millennium are minimal.
Thirdly, the present-day sediment yield cannot be estimated correctly when the initial state of a catchment is unknown. The sediment budget model can only provide the change in sediment storage and yields compared to a reference state.
Furthermore, the sediment budget model does not take into account soil redistribution due to landslides, gullying, glacial retreat and tectonic uplift. These processes can have a significant impact on the soil redistribution on different timescales, from short timescales related to extreme events, to millennial and longer timescales. Finally, all limitations mentioned in chapter 2 for the estimation of global soil erosion rates with the adjusted RUSLE model are also valid for the global sediment budget model.

3.4 Conclusions

In this study we introduced a new model to simulate long-term, large-scale soil redistribution based on the sediment mass-balance approach. The main objective here was to develop a sediment budget model that is compatible with Earth System Models (ESMs), to simulate large-scale spatial patterns of soil erosion and redistribution for floodplains and hillslopes following climate change and land use change. We applied this sediment budget model on the Rhine catchment as a first attempt to investigate its behavior and validated the model with observed data on sediment storage and erosion rates.

We show that the model reproduces the scaling relationships between catchment area and sediment storage found in observed data from Hoffmann et al. (2013). These scaling relationships show that the floodplain storage increases significantly with catchment area while the hillslope storage scales linearly with catchment area. The scaling exponents can be modified by changing the spatial distribution of erosion or by changing the residence time for floodplains. However, the main feature of the scaling relationships, which is that floodplain storage increases stronger with catchment area as hillslopes, is not changed. Based on this we conclude that the scaling relationships are an emergent feature of the model and mainly dependent on the underlying topography.

We found a mean soil erosion rate of $2.8 \pm 0.002\,\mathrm{t\,ha^{-1}\,year^{-1}}$ for the last millennium (850 - 2005AD). This is an overestimation when compared to the minimum Holocene erosion rate of $1.2 \pm 0.32\,\mathrm{t\,ha^{-1}\,year^{-1}}$ from Hoffmann et al. (2013). Also for present day the erosion rates from our model are overestimated. We argue that this is mainly due to the coarse resolution input data on climate and land cover, and the fact that the land cover factor of the erosion model is not adjusted for a coarse resolution application. Biases of the adjusted RUSLE model and the neglection of other factors, such as land management and slope-length for agricultural areas, also play a role. Based on this, we conclude that the most important step in improving global soil erosion rates in a coarse resolution model is by adjusting the R factor for a large-scale coarse resolution application. And if possible, add seasonality in the C factor to improve the interaction with the R factor. However, we aim with the sediment budget model to distinguish between the floodplain and hillslope sediment storage, simulate their long-term behavior, and more specifically estimate the spatial distributions rather than the total amounts. For this objective a coarse estimation of erosion is sufficient.

The erosion rates we found resulted in a change in floodplain and hillslope sediment storage during the last millennium of 11.95 ± 0.03 and 29.68 ± 0.01 Gt, respectively. Based on this and the observed data we estimate that the climate and land use changes during the last millennium contribute between 25 - 50% to the total sediment storage for the past 7500 years.

Disentangling the contribution from climate change and land use change on the change in sediment storage during the last millennium for the Rhine catchment, we find that in the climate change only scenario, the total change in sediment storage in floodplains

and hillslopes is 2.9 and 15.4 Gt, respectively. While in the land use change only scenario, the total change in sediment storage in floodplains and hillslopes is 10 and 27.4 Gt, respectively. This shows that land use change contributes most to the change in sediment storage during the last millennium for the Rhine catchment.
Furthermore, the model is capable of reproducing the overall spatial distribution of floodplain sediment storage of the last millennium. However, there are some outliers, such as the Mosel catchment for which the model simulates a too high sediment storage. This could be a result of biases in the erosion rates and the fact that our model is limited to the last millennium. We also found that the hillslope storages of the sub-catchments show a similar spatial pattern as the floodplain storage.
When analyzing the timeseries of erosion rates during the last millennium we found that the model reproduces the timing of the maxima in erosion rates as found in the study of Bork (1989). We also find that land use change is the main driver behind the trends in erosion and sediment storage for both floodplains and hillslopes. For floodplains, however, climate change has a non-negligible impact on the temporal variability of sediment storage. When keeping the land cover constant to the conditions in the period 850 to 950AD, we find that the sediment storage still increases due to an increased trend in precipitation in the last millennium.
A global application of the model indicates that the scaling behavior between sediment storage and catchment area for floodplains and hillslopes is a global feature. The hillslope sediment storage can in some occasions also scale exponentially with catchment area if the catchment consists out of an complex relief or if land use change is significant in steep areas. We conclude that the scaling exponents are mainly determined by the flow-accumulation for floodplains and by the slope distribution for hillslopes.
Furthermore, we found that for most of the investigated catchments in this study land use change is the main driver behind the change in sediment storage during the last millennium. Additionally, intensification of land use change results in a larger change in sediment storage relative to the change in the total erosion in a catchment.
For some catchments, such as the Amazon catchment, where land use change was small during the last millennium, climate change was the main driver behind the change in sediment storage during the last millennium.
However, these results may also depend on the way climate and land cover is simulated by MPI-ESM. Therefore, a comparison with data from other ESMs should be performed in the future.
The difference between the catchments in the sediment storage change during the last millennium is also controlled by the catchment characteristics. Catchments with steep slopes and small areas show a similar change in sediment storage as catchments with low slopes and large areas. The steepness of the landscape proves thus to be as important as the size of the catchment with respect to sediment storage.
In order to test the validity of the model on global scale, we used data on observed sediment yields from global river catchments. We found that although the sediment budget model cannot simulate the absolute present-day sediment yields based on data

of the last millennium, the spatial distribution of the sediment yields was comparable to the observed ones when the uncertainty in the observed yields was taken into account.

We conclude that our sediment budget model is a promising tool for estimating large-scale long-term sediment redistribution. An advantage of this model is its capability to use the framework of ESMs to predict trends in sediment storage and yields for the past, present and future.

There are also some limitations to the model. The sediment yield cannot be reproduced for catchments where the initial state of the catchment is uncertain. However, with correct data input on climate and land cover, the model can be made applicable for tropical catchments on the timescale of the last millennium, after adjusting the model parameters for these catchments. This is because we expect the effect of the last glaciation to be minimal on tropical catchments. In combination with low human activities in 850AD assuming an equilibrium state for these catchments in 850AD seems reasonable.

Furthermore, a more concrete parameterization for the residence time and deposition of floodplain sediment, and a possible new parameterization for the residence time of hillslope sediment could lead to an improvement of the model. Finally, more validation with long-term sediment storage from other catchments, especially tropical catchments, would be an important contribution in making the model better applicable on a global scale.

Chapter 4

Significant lateral fluxes of carbon and nutrients due to soil erosion: Outlook

4.1 Introduction

The interaction between soil redistribution and the global biogeochemical cycles is a new aspect in climate science and not many studies have been performed to quantify this interaction and the anthopogenic modifications to the biogeochemical cycles due to soil redistribution.
Studies on the effect of soil erosion on the carbon cycle indicate that soil erosion can result in significant lateral fluxes of soil organic carbon (SOC). Ito (2007), for example, coupled an empirical erosion model to a terrestrial carbon cycle model to estimate lateral displacement of SOC due to soil erosion. He estimated a significant lateral flux of $1.6 \pm 0.1\,\mathrm{Pg\,C\,year^{-1}}$ for the period 1900 - 2100AD. Doetterl et al. (2012) coupled estimates of global soil erosion to SOC concentrations in the soil, and calculated a SOC flux of $0.4 \pm 0.2\,\mathrm{Pg\,C\,year^{-1}}$ for the period 2000-2050AD on agricultural areas globally. Chappell et al. (2015) derived a relation between soil erosion and SOC erosion rates for agricultural lands and extrapolated this relation to other regions on the global scale. They found a total global SOC erosion flux between 0.35 and $1.27\,\mathrm{Pg\,C\,year^{-1}}$. However, these studies discuss that estimating lateral fluxes of carbon due to soil erosion only is not sufficient to quantify the net effects on the carbon budget. Instead, the integrated effect of the interacting processes behind soil redistribution should be studied and quantified.
A large part of the laterally displaced SOC is emitted as CO_2 during all stages of soil redistribution. The total global carbon emissions due to soil redistribution were estimated to range between 0.8 - $1.2\,\mathrm{Pg\,C\,year^{-1}}$ globally, which is already 10 to 15 % of the yearly global fossil fuel emission (Lal, 2003). This rate is comparable to the

$1.8 \pm 0.25\,\mathrm{Pg\,C\,year^{-1}}$ that is outgassed by streams and rivers globally (Raymond et al., 2013). This indicates that although large amounts of displaced SOC are buried in floodplains and on hillslopes (Hoffmann et al., 2013; Doetterl et al., 2012), CO_2 emissions due to soil erosion can be substantial. However, the above mentioned rates of CO_2 emission due to soil redistribution are uncertain, as it is not clear how decomposition rates of SOC will change at sites of deposition as a result of land use change, climate change, re-excavation by accelerated soil erosion, and dynamics of SOC replacement at eroding sites (Van Oost et al., 2007).

The interplay between soil erosion and deposition can also be a sink for atmospheric CO_2 as indicated by several studies (Harden et al., 1999; Liu et al., 2003; Van Oost et al., 2007; Berhe et al., 2007). This is not only a result of the dynamic replacement of carbon, but also due to the fact that soil erosion exposes low carbon-bearing soils that have a greater potential for carbon uptake (Van Oost et al., 2012). Berhe et al. (2007) estimated that soil erosion can lead to a yearly carbon sink that offsets up to 10 % of the global fossil fuel emissions. This is in the same order as the estimated carbon emissions due to soil redistribution. Van Oost et al. (2007) used caesium-137 and carbon inventory measurements from 10 watersheds in Europe and the USA, together with available global maps on SOC and environmental parameters, to estimate the net effect of soil erosion on the carbon cycle for agricultural soils. They found a global carbon sink of $0.12\,\mathrm{Pg\,C\,year^{-1}}$.

Considering the results of the above mentioned and other recent studies on the net flux of SOC due to soil redistribution we find a range from a source of 0.37 to $1\,\mathrm{Pg\,C\,year^{-1}}$ to a net uptake or sink of 0.56 to $1\,\mathrm{Pg\,C\,year^{-1}}$ (Van Oost et al., 2007). There exists thus a large uncertainty in the role of soil redistribution in the present-day global carbon budget. Furthermore, although, these studies have increased the understanding of the present-day short-term response of carbon dynamics to soil redistribution, past and future long-term effects have not been quantified yet (Van Oost et al., 2012).

Regarding other biogeochemical cycles such as the phosphorus and nitrogen cycles, studies on the global scale related to soil redistribution are very scarce. Quinton et al. (2010) estimated fluxes of nitrogen and phosphorus due to soil erosion on agricultural areas on a global scale for present day. They found yearly lateral fluxes of about 23-42 Tg of nitrogen, 2.1-3.9 Tg of organic phosphorus and 12.5-22.5 Tg of inorganic phosphorus.

Present-day river fluxes of total nitrogen to the world oceans are estimated to range between 45 Tg per year (Mayorga et al., 2010) and 60 Tg per year (Howarth, 2008), of which a large part can be explained by the strong fertilizer use. The total lateral flux by soil erosion for agricultural areas only, estimated by Quinton et al. (2010), is close to these riverine fluxes of nitrogen.

Few recent studies exist on the total phosphorus flux from the world's rivers. Mayorga et al. (2010) found a total yearly phosphorus flux of 9 Tg, while other studies found higher yearly estimates (11 Tg by Seitzinger et al. (2005), 20 Tg by Howarth et al. (1995)). The lateral fluxes of total phosphorus found by Quinton et al. (2010) are

larger than the estimated phosphorus export from the world's rivers to the ocean. This indicates that soil erosion on agricultural areas has a significant effect on the lateral fluxes of nitrogen and phosphorus. However, also other land cover types should be taken into account to estimate the global effect of soil redistribution on the lateral fluxes of carbon and nutrients. Furthermore, other processes such as mineralization or burial of these nutrients during soil redistribution should be considered as they can strongly influence these lateral fluxes.
The objective of this study is to provide an outlook on the significance of laterally displaced carbon and nutrients due to soil erosion, and to identify the main processes that should be modelled in order to quantify the overall effects of soil redistribution on the biogeochemical cycles. For this purpose we couple the global erosion rates from the adjusted RUSLE model to concentrations of carbon, nitrogen and phosphorus in the soils from a global soil database to estimate present-day lateral fluxes of carbon, nitrogen and phosphorus. This study does not only take into account agricultural areas, but provides a global picture of laterally displaced carbon and nutrient fluxes due to soil erosion. Additionally, we compare SOC erosion rates derived from data of ESMs with those derived from observational datasets on environmental parameters.

4.2 The global carbon cycle

4.2.1 Lateral displacement of soil organic carbon due to soil erosion for present day based on observed data

SOC data from the gridded 30 arcsec GSDE and soil erosion rates from the adjusted RUSLE model are used to estimate the lateral displacement of SOC for present day. The SOC percentage in the soil was available up to 2.3 m depth. Here, we only used the SOC content (%) for the top 0.2 m of the soil as soil erosion usually operates on the first few centimeters of the soil (Van Oost et al., 2007; Doetterl et al., 2012). The amount of soil erosion was then converted into carbon erosion by multiplying the total area-weighted SOC content (%) with the erosion rate. To estimate carbon erosion for different land cover types we multiplied the total area-weighted SOC content (%) with the land cover area (% of the area of a grid cell) and the erosion rate.
We found a global mean SOC erosion rate for present-day of 37.3 $\mathrm{g\,m^{-2}\,year^{-1}}$, with an uncertainty range of 32.9 to 61.4 $\mathrm{g\,m^{-2}\,year^{-1}}$ based on the uncertainty in the estimated erosion rates. This corresponds to a total amount of eroded SOC of 5.1 $\mathrm{Pg\,year^{-1}}$ with an uncertainty range of 4.7 to 7 $\mathrm{Pg\,year^{-1}}$ (Table 4.1). This global SOC flux is five times larger than the maximum global flux of 1.2 $\mathrm{Pg\,year^{-1}}$ found by (Chappell et al., 2015). In their study they estimated the total global soil erosion to be much lower than our estimates. Furthermore, Chappell et al. (2015) extrapolated the relationship they found between soil erosion and SOC erosion for agricultural lands on the global scale. As agricultural lands have a much lower erosion and SOC erosion rate than for

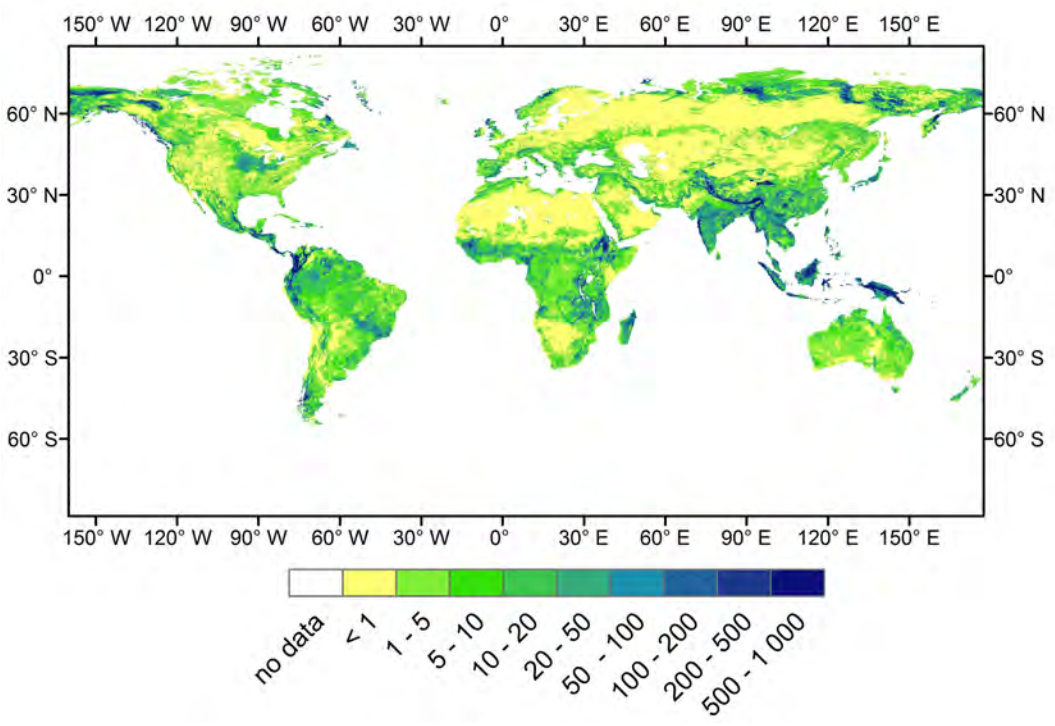

Figure 4.1: Present-day global SOC fluxes ($g\,m^{-2}\,year^{-1}$) due to soil erosion.

example mountainous regions, it is expected that their estimation will be lower than the findings of this study.

For agricultural land we found a mean SOC erosion rate of 34.8 $g\,m^{-2}\,year^{-1}$, with an uncertainty range of 32.9 to 38.4 $g\,m^{-2}\,year^{-1}$. Our estimates for agricultural land are up to two times higher than the 15.5 $g\,m^{-2}\,year^{-1}$ from Van Oost et al. (2007) and the 23.3 $g\,m^{-2}\,year^{-1}$ from Doetterl et al. (2012). This difference is related to the different soil database used in comparison to the other studies, and to uncertainties in the erosion rates related to the unadjusted factors in the RUSLE model, such as the C factor. Estimates of eroded SOC for other land use/ land cover types is provided in Appendix A.3.

Figure 4.1 shows the global SOC erosion rates for present day showing the highest rates in mountainous areas, which is related to the high erosion rates. Furthermore, significant SOC erosion rates (> 50 $g\,m^{-2}\,year^{-1}$) can be found in the tropics and in agricultural areas (China and India) where SOC stocks in the topsoil are large. Looking at the difference between the regions, we find the highest total eroded SOC for Asia and South-America (Table 4.1). This is in agreement with the total exported river particulate organic carbon (POC) from Mayorga et al. (2010) simulated by the Global Nutrient Export from Watersheds 2 (NEWS 2) model.

The eroded SOC reaches the rivers and streams mainly in the form of particulate organic carbon (POC). The POC flux to the global ocean is estimated at 0.157 Pg $year^{-1}$ (Galy et al., 2015), while our total estimated accelerated SOC erosion is in the order of 5.1 Pg $year^{-1}$ (Table 4.2). This makes the POC flux only 3 % of the total eroded

SOC, indicating that most of the eroded SOC is either emitted to the atmosphere or buried on hillslopes or in floodplains. Assuming that approximately 20% of the total eroded SOC is emitted to the atmosphere (Lal, 2003; Chappell et al., 2015), we find that about 1 Pg year^{-1} of carbon is emitted as CO_2 to the atmosphere due to soil redistribution (Table 4.2). This value is similar to the range of 0.8 – 1.2 Pg carbon year^{-1} found by Lal (2003), and the range of 0.3 – 1 Pg carbon year^{-1} found by Chappell et al. (2015). Furthermore, the estimated emissions of CO_2 due to soil redistribution are 13% of the total global fossil fuel emissions (7.8 Pg year^{-1}). However, we can conclude that most of the eroded SOC is buried and stored in terrestrial deposition zones, such as wetlands, reservoirs, floodplains and colluvial soils (Doetterl et al., 2012). Additionally, soil erosion also results in an extra uptake of CO_2 from the atmosphere by dynamic replacement, which is unquantified on the global scale.

Table 4.1: Estimates of global soil erosion (E) and linked SOC fluxes for present day per region. Erosion and SOC fluxes are in Pg year^{-1}.

	E mean	E uncertainty	SOC mean	SOC uncertainty
Europe	4.00	3.39 – 8.18	0.16	0.12 – 0.42
Asia	35.02	31.44 – 43.90	2.14	1.95 – 2.49
Africa	14.48	13.83 – 15.41	0.60	0.58 – 0.63
Australia	2.09	1.82 – 2.45	0.05	0.04 – 0.06
North-America	7.39	5.09 – 24.10	0.46	0.34 – 1.15
South-America	9.44	9.08 – 10.70	1.18	1.13 – 1.53
Central-America	1.99	1.93 – 2.06	0.20	0.19 – 0.20
Global average	81.12	72.62 – 120.28	5.14	4.70 – 7.00

Table 4.2: Global carbon fluxes (Pg year^{-1}) from (Ciais et al., 2014) in relation to our estimates of displaced and mineralized carbon due to soil erosion.

Flux	Mean carbon gains (+) and losses (-)
Fossil fuels	(-) 7.8
Net land use change	(-) 1.1
Gross photosynthesis	(+) 123
Total respiration + fire	(-) 118.7
Volcanism	(-) 0.1
Freshwater outgassing	(-) 1
Rock weathering	(+) 0.3
Burial in lakes	(+) 0.2
River flux land to ocean (POC+DOC+DIC)	(-) 0.9
POC river flux (Galy et al., 2015)	(-) 0.16
Eroded SOC	5.1
Erosion induced SOC mineralization	(-)1.0

4.2.2 Lateral displacement of soil organic carbon due to soil erosion for present day from CMIP5 model data

The same ESMs from CMIP5 as presented in chapter 2 are used here to investigate the SOC erosion rates from ESMs for present day. First we test how the models perform with respect to the total SOC stocks and the spatial variability in the SOC content in soils. For this purpose, data on the SOC content from the historical simulations of the models, and SOC data from GSDE for three different soil depths are used. The carbon stocks in the soil were calculated according to Batjes (1996):

$$SOC_d = \sum_{n-1}^{k} OC_i * BD_i * D_i * (1 - GRAV_i) * A \tag{4.1}$$

where SOC_d is the total amount of organic carbon (t) above a certain depth (d), OC_i represents the concentration of organic carbon (%) in layer i, BD_i is the bulk density of layer i (g cm^{-3}), D_i is the thickness of this layer (cm), $GRAV_i$ is the volume (%) of gravel in layer i, and A is the grid cell area (ha).
As the models do not report the depth of SOC in the soil profile, it is assumed that the SOC simulated by the models represent the SOC content in the upper 0.2 m of the soil. It should be mentioned that many soil models were originally developed to simulate carbon dynamics to a soil depth of 0 to 0.2 m (Todd-Brown et al., 2013).
Results show that the global total SOC stocks differ significantly between the models (Table 4.3). MPI-ESM overestimates the observed SOC stocks for all soil depths. The SOC stocks from the other models are comparable to the observed SOC stocks for one of the three soil depths. When considering the 0.2 m soil depth, the total SOC stock from the CCSM4 model is closest to the observed SOC stock, while all other models strongly overestimate the total SOC stock for this depth.

Table 4.3: Observed versus modelled present-day total SOC stocks (Gt). The observed SOC data is given for three soil depths (0.2 m, 1 m and 2.3 m).

	SOC_d total	SOC_d uncertainty
MPI-ESM-LR	2767	2736 – 2799
IPSL-CM5A-LR	1385	1365 – 1406
CCSM4	561	556 – 566
MIROC-ESM and bcc-csm1-1	2097	2042 – 2153
observed (0.2 m)	471	-
observed (1 m)	1450	-
observed (2.3 m)	1897	-

With respect to the spatial correlation between the models and the observations for the different depths, the highest correlation coefficients and lowest RMSE errors are

found for the 0.2 m soil depth (Table 4.4). However, the general performance of the models with respect to the spatial variability and overall values of the observed SOC content is poor. The largest biases are found for MPI-ESM, and the smallest biases are found for the MIROC-ESM. This is in accordance with the findings of Todd-Brown et al. (2013), who examined similar models, however, used higher resolution versions of the models. They concluded that most ESMs cannot reproduce the grid-scale spatial variation in SOC and maybe be missing key processes.
The resulting global mean SOC erosion rates using data from the CMIP5 models on climate, land use and SOC content are presented in figure 4.2. SOC erosion rates calculated using data derived from observation databases on climate, land use and soil, will be referred to as observed SOC rates. If SOC erosion is calculated using soil erosion estimates from CMIP5 data and SOC content from observations, we find that the resulting mean global SOC erosion rates from CMIP5 data come closer to the mean observed SOC erosion rate. However, if both the soil erosion and SOC estimates are used to compute SOC erosion rates, we find that the models show an overestimation by two to ten times in the mean SOC erosion rate. These biases in the SOC erosion rates are a result of uncertainties in the climate, land cover, and the SOC content of the selected CMIP5 models. Therefore, future studies on estimating SOC erosion rates and other effects of soil redistribution on the carbon cycle using ESMs need to take these uncertainties into account.

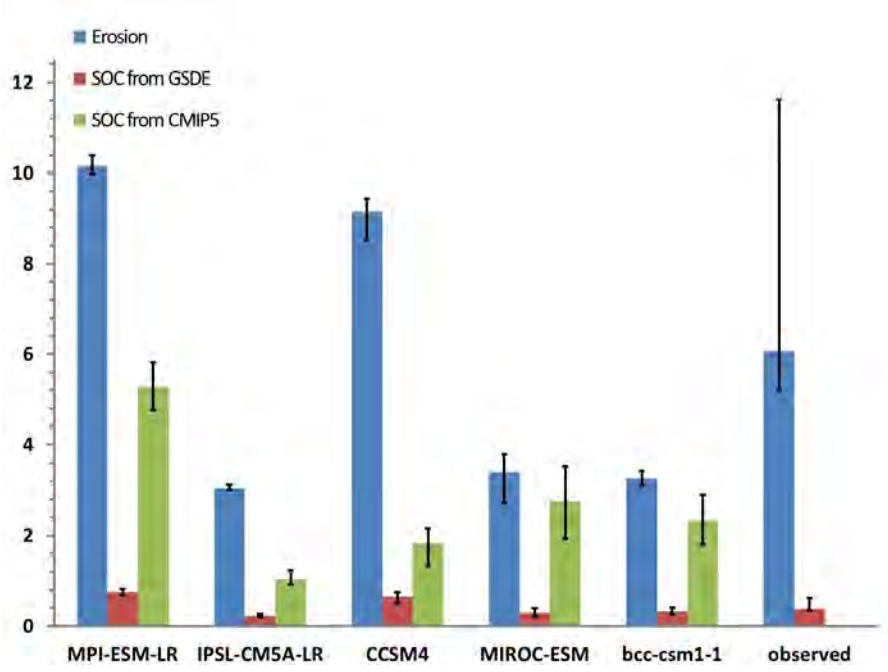

Figure 4.2: Present-day mean global soil erosion rates from observed data and CMIP5 data (blue bars), and related SOC erosion rates based on SOC data from GSDE (red bars) and CMIP5 models (green bars). All units are in $\mathrm{t\,ha^{-1}\,year^{-1}}$.

Table 4.4: Statistics of modelled versus observed present-day SOC content (t ha^{-1}) for three soil depths (0.2 m, 1 m and 2.3 m). The r-value is the Pearson correlation coefficient and RMSE is the root mean square error.

	Observed (0.2 m)		Observed (1 m)		Observed (2.3 m)	
	RMSE	r-value	RMSE	r-value	RMSE	r-value
MPI-ESM-LR	229	-0.05	246	-0.04	292	-0.03
IPSL-CM5A-LR	86	0.39	164	0.34	241	0.31
CCSM4	51	0.12	204	0.07	279	0.07
MIROC-ESM and bcc-csm1-1	199	0.44	187	0.39	234	0.36

4.3 The global nitrogen and phosphorus cycles

Data on the total nitrogen and phosphorus content in the soils from the gridded 30 arcsec GSDE and soil erosion rates from the adjusted RUSLE model are used to estimate the lateral displacement of these nutrients for present day. This includes both organic and inorganic nitrogen and phosphorus. Also here, only the nitrogen and phosphorus contents in the top 0.2 m of the soil are used. The same approach as for the SOC was applied to convert soil erosion into nitrogen and phosphorus erosion.
We found a global mean nitrogen erosion rate for present day of 2.4 $g\,m^{-2}\,year^{-1}$ with an uncertainty range of 2.1 to 3.9 $g\,m^{-2}\,year^{-1}$. This corresponds to a total amount of eroded nitrogen of 336 Tg $year^{-1}$, with an uncertainty range of 306 to 444 Tg $year^{-1}$ (Table 4.5). For phosphorus erosion we found a global mean rate of 0.8 $g\,m^{-2}\,year^{-1}$, with an uncertainty range of 0.7 to 1.1 $g\,m^{-2}\,year^{-1}$. This corresponds to a total amount of eroded phosphorus of 94 Tg $year^{-1}$, with an uncertainty range of 84 to 120 Tg $year^{-1}$ (Table 4.5).
For agricultural land we found a total flux of eroded nitrogen of 50 Tg $year^{-1}$, with an uncertainty range of 47.9 to 54.8 Tg $year^{-1}$. The total flux of eroded phosphorus on agricultural land was estimated at 16.6 Tg $year^{-1}$, with an uncertainty range of 15.6 to 18.1 Tg $year^{-1}$. The total flux of nitrogen on agricultural land is somewhat higher compared to the flux found by Quinton et al. (2010), while the total flux of phosphorus lies in the range found by Quinton et al. (2010). Estimates of eroded nitrogen and phosphorus for other land use/land cover types are provided in Appendix A.3.
Results show that the present-day spatial distribution of SOC, nitrogen and phosphorus erosion rates are comparable on the global scale, with the highest rates in the mountains, tropics and agricultural areas (Fig. 4.1, 4.3a and b). This indicates that the spatial variability in soil erosion, which is mainly affected by the precipitation, runoff, relief and human activities, determines the spatial distribution of SOC, nitrogen and phosphorus erosion rates.

The spatial distribution of the SOC, nitrogen or phosphorus contents in the soils is of secondary importance. This is consistent with the findings of Mayorga et al. (2010),

(a)

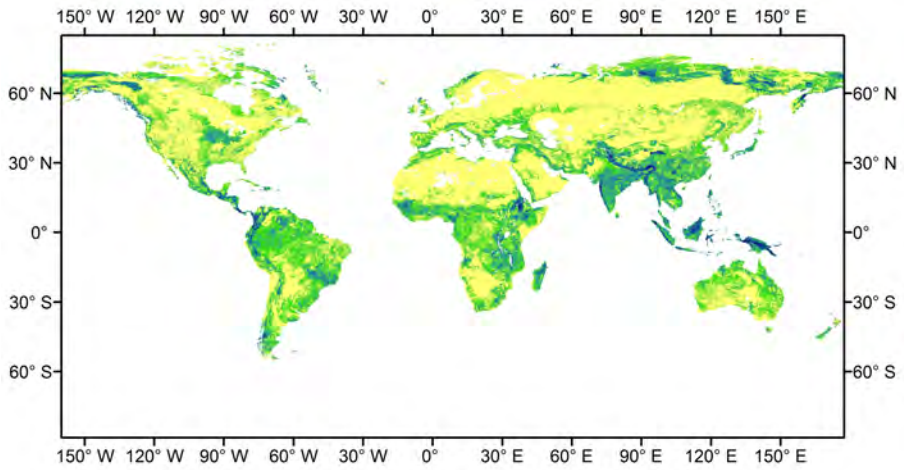

(b)

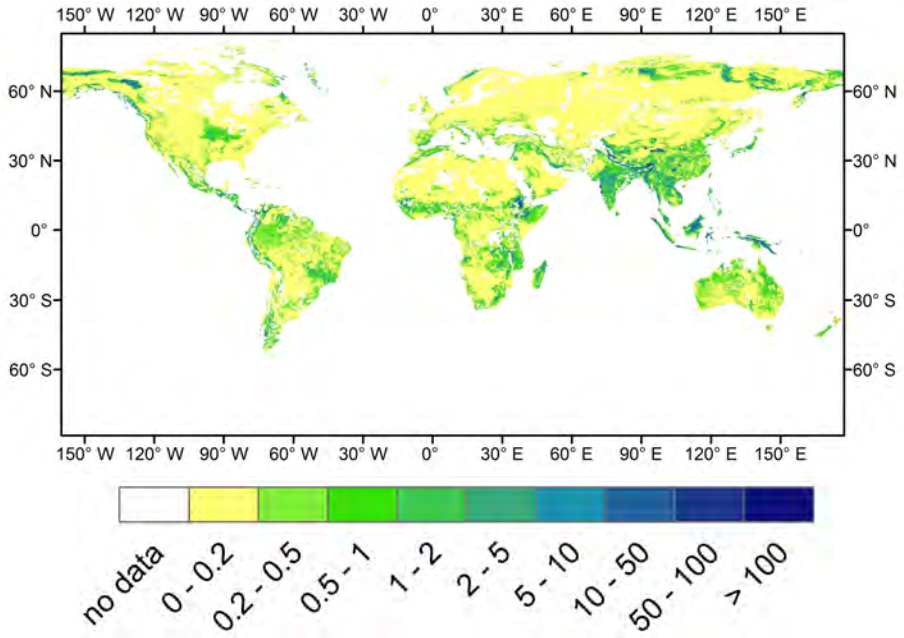

Figure 4.3: Present-day (a) global nitrogen and (b) phosphorus fluxes ($\mathrm{g\,m^{-2}\,year^{-1}}$) due to soil erosion.

where they show that the river export of total organic carbon, nitrogen and phosphorus are mainly determined by a combination of runoff, relief and human activities. They also point out that areas with a high runoff, such as the humid tropics, can lead to high exports of carbon and nutrients even though the human pressures in these areas can be low and depletion of nutrients can be substantial. For example, it is well-known that tropical areas are extremely phosphorus limited (Goll, 2013). Still, the phosphorus erosion rates in some tropical regions, such as the Amazon, are high due to the strong soil erosion rates (Fig. 4.3b).

Looking at the difference between the regions, the highest eroded nitrogen and phosphorus erosion fluxes are found for Asia, followed by Africa and South-America (Table 4.5). The lowest fluxes are found for Australia. This is mostly in agreement with the findings of Mayorga et al. (2010), where they found the highest export of particulate nitrogen and phosphorus for Asia, and the lowest for Australia.
Although, the difference in the export of nitrogen and phosphorus between South-America and Africa is relatively small, Mayorga et al. (2010) found a higher export for South-America, in contrast to our findings for the total eroded nitrogen and phosphorus. This difference can be attributed to multiple factors. First of all, erosion of nutrients in a catchment is not always correlated to the export of nutrients from the catchment, due to deposition and mineralization of these nutrients on the way to the catchment outlet. This indicates the importance of investigating the spatial organization of erosion and deposition of sediment and nutrients in a catchment, rather than concentrating only on the export of these elements from the catchment Steegen et al. (2001).

Table 4.5: Estimates of global soil erosion (E) and linked nitrogen (N) and phosphorus (P) fluxes for present day per region. Erosion fluxes are in $\mathrm{Pg\,year^{-1}}$, while nitrogen and phosphorus fluxes are in $\mathrm{Tg\,year^{-1}}$.

	E mean	E uncertainty	N mean	N uncertainty	P mean	P uncertainty
Europe	4.0	3.4 – 8.2	10.3	8.5 – 24.4	4.2	3.7 – 6.8
Asia	35.0	31.4 – 43.9	165.0	149.2 – 194.9	45.1	40.0 – 51.9
Africa	14.5	13.8 – 15.4	50.9	48.6 – 54.1	17.3	16.4 – 18.5
Australia	2.1	1.8 – 2.5	4.5	3.9 – 5.4	2.6	2.2 – 3.0
North-America	7.4	5.1 – 24.1	19.4	14.0– 61.2	6	4.4 – 16.2
South-America	9.4	9.1 – 10.7	45.6	43.8 – 53.2	9.4	9.0 – 11.3
Central-America	2.0	1.9 – 2.1	15.2	14.9 – 15.6	2.8	2.7 – 2.9
Global average	81.1	72.6 – 120.3	336.0	306.5 – 444.1	93.8	84.4 – 119.9

On a global scale, this can be done by modelling the internal dynamics of sediment and nutrients in a catchment. Secondly, Mayorga et al. (2010) included the effect of sediment trapping behind dams and the effect on the total river export of carbon and nutrients. In our study this is not taken into account. Also, biases in erosion rates from the adjusted RUSLE model and biases in the simulated carbon and nutrient export as mentioned in the study of Mayorga et al. (2010) could play a role here.
Our estimates of total mobilized nitrogen and phosphorus by soil erosion on a global scale are in the order of respectively 336 and 94 Tg $\mathrm{year^{-1}}$ (Table 4.6 and Table 4.7). The total mobilized nitrogen is in the same order as the sum of nitrogen deposition, fertilizer supply and natural and anthropogenic fixation by biomass. The total mobilized phosphorus exceeds by far the production of phosphorus by weathering and the supply of phosphorus to the soils by fertilizers. This confirms the very large lateral fluxes of these nutrients due to soil erosion as previously indicated by Quinton et al. (2010). However, our findings also show that other areas, except for agricultural areas, can have an equally or even larger contribution to the total global eroded nitrogen and

phosphorus. This indicates the importance of a global assessment of the effects of soil erosion on the nutrient cycles.

Table 4.6: Global nitrogen fluxes (Tg year^{-1}) in relation to our estimates of displaced nitrogen by soil erosion.

Flux	Mean nitrogen gains (+) and losses (-)	Reference
Denitrification	(-) 109	Ciais et al. (2014)
Atmospheric deposition	(+) 63	Ciais et al. (2014)
Fertilizer supply	(+) 160	Food and of the United Nations (2015)
Natural and anthropogenic fixation by biomass	(+) 118	Ciais et al. (2014)
Eroded nitrogen	(-) 336	this study
Riverine flux	(-) 45-60	(Mayorga et al., 2010; Howarth, 2008)

Table 4.7: Global phosphorus fluxes (Tg year^{-1}) in relation to our estimates of displaced phosphorus by soil erosion.

Flux	Mean phosphorus gains (+) and losses (-)	Reference
Mining	(-) 161	Goll (2013)
Weathering	(+) 1.6	Goll (2013)
Fertilizer supply	(+) 48	Food and of the United Nations (2015)
Eroded phosphorus	(-) 94	this study
Riverine flux	(-) 9-20	(Mayorga et al., 2010; Seitzinger et al., 2005) (Howarth et al., 1995)

The total flux of nitrogen and phosphorus to the global ocean is estimated at respectively 45 to 60 and 9 to 20 Tg year^{-1} (Table 4.6 and 4.7), of which respectively about 14 and 7 Tg year^{-1} is in the form of particulate nitrogen (PN) and (PP) Mayorga et al. (2010). We expect that soil erosion will lead mostly to PN and PP, as in the case of SOC erosion. This makes the total nitrogen flux only 13 to 18 % and the PN flux only 4 % of the total eroded nitrogen. While the total phosphorus flux is 10 to 21 % of the total eroded phosphorus and the PP flux is 7 %. These numbers indicate that, similar to SOC erosion, most of the nutrients are either mineralized or buried on hillslopes are in floodplains. The mineralization and burial of nutrients due to soil erosion is largely unknown on the global scale.

4.4 Limitations of current approaches

One of the limitations of implementing the adjusted RUSLE model to estimate lateral fluxes of carbon and nutrients by soil erosion is the fact that this model does not include other soil erosion processes, such as, glacial erosion and erosion by tectonic uplift, coastal erosion, landslides and gully erosion. Regions where such forms of soil

erosion prevail can show a very different net effect of soil erosion and consequently of soil redistribution on the fluxes of carbon and nutrients. Zhao et al. (2015) showed for the Chinese Loess Plateau, that the strength of the erosion induced carbon sink can be up to four times lower when sediment and SOC mobilization by gully erosion and landslides is taken into account. Present-day glacier retreat and tectonic uplift lead to increased continental soil erosion rates that not only result in the burial of fast amounts of carbon and nutrients, but also in increased weathering that promotes the uptake of CO_2 from the atmosphere (Chaopricha and Marín-Spiotta, 2014; Galy et al., 2007; Goudie and Viles, 2012). Coastal erosion of the thawing Arctic permafrost leads to the activation of old carbon and contributes to the export of large amounts of organic carbon export from this region (Vonk et al., 2012). In other areas coastal erosion due to sea level rise as a result of global warming can also lead to increased amounts of carbon and nutrient export to the oceans.
Other limitations of the approach in this study are related to the uncertainty in erosion estimates in mountainous areas, and uncertainty in SOC, nitrogen and phosphorus contents estimates in certain regions.

4.5 Next steps

As shown in the previous sections of this study, soil erosion can mobilize substantial amounts of SOC and nutrients on a global scale. However, export of the eroded carbon and nutrients from rivers is only a small part of the total mobilized amount. This shows that it is essential to understand the dynamics of the carbon and nutrients in a landscape itself, before these elements are exported by the rivers. These dynamics are strongly coupled to the dynamics of sediment, which consists out of soil erosion, sediment deposition and transport by runoff. Therefore, the next step would be to explicitly model the sediment redistribution in a landscape, and couple the processes such as mineralization, burial and transport of the biogeochemical elements to the sediment redistribution processes. In order to estimate the temporal variability of the change in stocks, lateral and vertical fluxes of carbon and nutrients due to soil redistribution, an interactive simulation with the main sources and sinks of the biogeochemical elements would be required.
Additionally, the other forms of soil erosion such as, continental erosion, coastal erosion, landslides and gully erosion should also studied and quantified in the future in order to have a full picture of the effects of soil redistribution on the biogeochemical cycles.

4.6 Conclusions

In this study present-day global soil erosion rates from the adjusted RUSLE model were coupled to the carbon, nitrogen and phosphorus contents in the soil, to estimate mobilization of carbon and nutrients by soil erosion. The results show that soil erosion can lead to significant lateral fluxes of carbon and nutrients, especially in mountainous regions, agricultural areas and the humid tropics. Emissions of CO_2 from mineralization of mobilized SOC by soil erosion are 13% of the total global fossil fuel emissions ($7.8\,\mathrm{Pg\,year^{-1}}$). The total mobilized nitrogen by soil erosion is in the same order as the inputs of nitrogen in the soil by deposition, fertilizer supply, and natural and anthropogenic fixation by biomass. While, the total mobilized phosphorus by soil erosion exceeds by far the production of phosphorus by weathering and the supply of phosphorus to the soils by fertilizers.

Comparing the estimate of the lateral flux of eroded SOC found for agricultural areas to those from Doetterl et al. (2012) and Van Oost et al. (2007) shows that the mean global SOC erosion rate in this study is up to two times higher than the mean rates from these studies. We expect that this is mainly due to the fact that a different version of the RUSLE model and different global empirical databases on soil, land cover/land use and climate are used. Furthermore, biases related to the estimation of global soil erosion with the adjusted RUSLE model as described in chapter 2 also play a role here. Furthermore, the estimated total nitrogen flux due to erosion on agricultural areas was slightly higher than the range of lateral nitrogen fluxes found by Quinton et al. (2010). The total phosphorus flux due to erosion on agricultural areas was in the range of the lateral phosphorus fluxes found by Quinton et al. (2010).

This study also shows that only a small amount of the total mobilized SOC, nitrogen and phosphorus is exported from the terrestrial biosphere by rivers globally. For the SOC, the total exported POC is only about 3% of the mobilized amount, while for the nitrogen and phosphorus the total exported PN and PP are respectively 4% and 7% of the total mobilized amounts. This indicates that the dynamics of the biogeochemical cycles in the landscape play an important role and much of the mobilized carbon and nutrients by soil erosion is either mineralized or buried on hillslopes, in floodplains, and man-made reservoirs.

It can be concluded that in order to quantify the net global effects of soil redistribution on the carbon and nutrient cycles a spatially explicit model is needed where processes related to the biogeochemical cycles such as, mineralization, burial and transport are tightly coupled to the sediment processes in a landscape. Additionally, interactive simulation with all the main sources and sinks of the biogeochemical elements will be required to simulate the temporal variability in the stocks, lateral and vertical fluxes of these elements due to soil redistribution. Finally, other soil erosion processes such as, continental and coastal erosion, landslides and gully erosion should be quantified in order to have a full picture of the effects of soil erosion on the biogeochemical cycles.

Chapter 5

Summary and Conclusions

The primary objective of this study was to simulate soil redistribution on a global scale, and investigate the effects of external forces such as, land use change and climate change, on the soil redistribution rates. The focus was the development of methods and tools that are compatible with Earth System Models (ESMs) and can simulate long-term soil erosion rates and sediment fluxes. In this context an attemption is made to gain insight into the drivers behind the spatial and temporal change of soil erosion rates and the resulting soil redistribution for the last millennium (850-2005AD) on a global scale. Also, the scaling behavior of characteristics of river catchments, such as slope and area, and their impact on the effect of external forces is investigated.
In the following an overview and summary of the main results and the main conclusions is provided in Section 5.1. Recommendations for future work are given in Section 5.2.

5.1 Summary of findings

5.1.1 Global soil erosion

5.1.1.1 How can realistic global soil erosion rates be derived for present day, and what are the main uncertainties?

This study presents an adjusted version of the Revised Universal Soil Loss Equation (RUSLE) model, compatible with the coarse resolution of ESMs, that includes improvements made to the computation of the topographical- and rainfall erosivity factors. Using obervational datasets on environmental parameters, the model simulates accelerated soil erosion rates for many regions with a mean global erosion rate of $6.5\,\mathrm{t\,ha^{-1}\,year^{-1}}$ for present day. These erosion rates are comparable to the high-resolution rates from Europe (Cerdan et al., 2010), and the USA (NRI database). The factors of the adjusted RUSLE model that were not improved, such as the land cover and the soil erodibility factors, and the neglection of the land-management factor, are

identified as the main uncertainties in estimating present-day global soil erosion rates with this model. Also the rainfall erosivity factor can be further improved for tropical climates.

5.1.1.2 Can global soil erosion rates that are derived from observational datasets be reproduced with climate and land cover data from Earth System Models?

Out of the five ESMs that are investigated, only two models (CCSM4 and MIROC-ESM) show a similar continental variability in soil erosion rates as the ones based on observed data. However, none of the selected ESMs show a similar grid-scale variation in global soil erosion rates as the ones from observed data. This is mainly due to the sensitivity of the adjusted RUSLE model to data on land cover and climate.

5.1.1.3 How did soil erosion change during the last millennium and what were the main drivers behind this change?

The ESMs that were used in this study disagree on the global trend of erosion for the last millennium. MPI-ESM and CCSM4 show a significant increase in global soil erosion rates during the last millennium, which is mainly related to the strong land use change simulated by these models for most parts of the world. IPSL-CM5A shows a decreasing trend mainly due to the simulated precipitation decrease in the tropics, especially in South-America. The other models do not show a significant change in the mean erosion trend during the last millennium. However, the median soil erosion trends from all models show a non-negligible signal related to land use change for the last two centuries.

5.1.2 Global soil redistribution

5.1.2.1 How to simulate large-scale sediment storage and fluxes for the long-term (centennial to millennial timescales)?

In order to simulate soil redistribution, a new large-scale sediment budget model was developed that is compatible with the coarse resolution of ESMs. This new model builds on the adjusted RUSLE model and simulates beside soil erosion, also sediment deposition in floodplains and on hillslopes, as well as sediment transport. After being calibrated based on data from the Rhine catchment, the new model was forced with climate and land cover data from the MPI-ESM for the last millennium. The model reproduces the spatial distribution of sediment storage in floodplains when compared to observations from the Rhine catchment (Hoffmann et al., 2007). Also, the scaling relationships between sediment storage and catchment area for the non-Alpine part of the Rhine catchment (Hoffmann et al., 2013) are correctly reproduced.

5.1.2.2 How did sediment storage change during the last millennium and what were the main drivers behind this change?

Application of the model for 20 global river catchments shows that the change in erosion rates during the last millennium modified the sediment budgets, resulting in a significant increase in sediment storage for the different catchments. Globally, land use change turned out to be the main driver behind this increase for most of the catchments during the last millennium. This is consistent with the findings of other studies, such as the study of Hoffmann et al. (2013) on measured sediment storage in the Rhine catchment, and the study of Syvitski et al. (2005) on simulated and observed sediment yields for global catchments. Furthermore, the global spatial distribution of present-day sediment yields simulated by the model for different river catchments is comparable to the distribution from observed sediment yields, when the uncertainty in the observations is taken into account.

5.1.2.3 How do catchment characteristics influence the change in sediment storage on the long-term?

This study shows that catchments with steep slopes and small areas show a similar change in sediment storage during the last millennium as catchments with low slopes and large areas. The steepness of the landscape proves thus to be as important as the size of the catchment with respect to change in sediment storage. Additionally, all investigated global catchments show that sediment storage in floodplains scales exponentially with the catchment area, while for hillslopes this scaling is mostly linear. Based on these results the scaling behavior between sediment storage and catchment area is identified as a global feature, which is a result of the topography.

5.1.3 Carbon and nutrient cycles

5.1.3.1 How large are present-day lateral fluxes of carbon and nutrients due to soil erosion only?

This study shows that soil erosion can lead to significant lateral fluxes of carbon and nutrients, especially in mountainous regions, agricultural areas and the humid tropics. Soil erosion leads to total global fluxes of 5 Pg year^{-1}, 336 Tg year^{-1}, and 94 Tg year^{-1} for soil organic carbon (SOC), nitrogen and phosphorus respectively. The flux of SOC due to soil erosion results in emissions of CO_2 that are 13% of the total global fossil fuel emissions. The total mobilized nitrogen by soil erosion is in the same order as the total input of nitrogen in the soil. While, the total mobilized phosphorus by soil erosion exceeds by far the production of phosphorus by weathering and the supply of phosphorus to the soils by fertilizers.

5.1.3.2 How does soil redistribution impact these lateral fluxes of carbon and nutrients?

This study shows that the total mobilized fluxes for carbon, nitrogen and phosphorus by soil erosion comprise 3%, 4% and 7% of the total particulate organic carbon (POC), particulate nitrogen (PN) and particulate phosphorus (PP) respectively, that are exported by global rivers. This indicates that the dynamics of the biogeochemical cycles in the landscape play an important role and much of the mobilized carbon and nutrients by soil erosion is either mineralized or buried on hillslopes, in floodplains, and man-made reservoirs (Van Oost et al., 2012; Quinton et al., 2010). These dynamics of biogeochemical cycles in a landscape are tightly linked to the sediment dynamics or soil redistribution.

5.1.3.3 Which approach should be taken to quantify the main effects of soil redistribution on the carbon and nutrient cycles?

The next step is to simulate the main processes of biogeochemical cycles after soil erosion takes place, such as mineralization, burial and transport. In order to quantify the main effects of soil redistribution on the carbon and nutrients cycles, these processes should be coupled to the sediment dynamics of a spatially explicit model such as the global sediment budget model presented in this study. This approach should be compatible with ESMs in order to run an interactive simulation with the biogeochemical components of ESMs in the future. This is needed to simulate the temporal variability of the change in the stocks, and the lateral and vertical fluxes of carbon and nutrients due to soil redistribution.

5.2 Conclusions

This study is, to my knowledge, the first one to model soil redistribution on a global scale on centennial to millennial timescales, taking into account the large-scale spatial variability in soil detachment, deposition and transport. This study shows that the erosion component of the newly developed sediment budget model, is applicable on a coarse resolution on the global scale, and can reproduce the spatial variability in soil erosion rates for Europe and the USA. Despite the fact that the deposition and transport components of the new model are calibrated based on data from the Rhine catchment, the new model still reproduces the global features of soil redistribution.
The findings in this study indicate accelerated rates of soil erosion for present day in most parts of the world. These erosion rates are a result of the combination of climate change and intensified land use change. The change in erosion rates during the last millennium modified the sediment budgets globally and resulted in a significant increase in sediment storage in floodplains and on hillslopes for different global catchments.

This study identifies that land use change turned out to be the main contributor to the change in sediment storage for most global catchments during the last millennium. Catchment characteristics, such as catchment area, slope, and sediment connectivity, play an important role in buffering or amplifying the effect of external forces on the change in erosion and sediment storage. It should be noted that the results presented in this study are affected by the sensitivity of the new model to climate and land cover data, and biases in the estimation of model parameters. A general limitation in simulating historically realistic soil redistribution and resulting sediment yields with the new model arises from the unknown initial state of a river catchment.
Finally, this study shows that soil erosion can result in significant fluxes of carbon and nutrients globally. However, only a small part of the mobilized carbon and nutrients due to soil erosion is exported by rivers. This indicates the importance of including sediment dynamics in ESMs to estimate the overall impact of soil redistribution on the biogeochemical cycles, and quantify the human impact, for the past, present and future. With the newly developed sediment budget model a first step is made in this direction.

5.3 Recommendations for future work

5.3.1 Future model developments with respect to global soil redistribution

In this study erosion rates are calculated without taking into account the effects of land management and slope length. Both factors are important for agricultural areas, which occupy a large part of the land surface globally. It is expected that in the future land management will play an even more important role, especially in combating soil degradation. Therefore, future studies on global soil erosion rates should especially focus on simulating the effects of land management on erosion.
Furthermore, in this study the seasonal interaction between land cover or land use with rainfall erosivity is ignored. The interaction between these factors is very important in areas with agriculture and areas with a strong seasonal character. This is another important point to focus on in future studies on global soil erosion.
To improve the application of the sediment budget model on a global scale, validation with long-term sediment storage and yields from other large catchments should be performed. Model parameters related to the sediment residence time and deposition are calibrated based on data for the Rhine catchment, as this catchment was one of the only catchments with observed long-term sediment storage data. The model parameters should also be adjusted for catchments with different environmental conditions, such as tropical catchments.
In order to apply the sediment budget model on timescales longer than the last millennium additional changes to the parameterization of the residence time of sediment

in floodplains and hillslopes should be implemented. In the current setup of the model it is assumed that the residence time for floodplains is only dependent on the catchment area. However, the change in surface slope due to sediment storage on a timescale longer than the last millennium can impact the residence time (Hoffmann, 2015). Also, it is assumed that the residence time for hillslopes is in the order of the timescale of the last millennium. Therefore, to simulate soil redistribution for longer timescales, a residence time for hillslopes needs to be parameterized that includes the long-term interaction of sediment between hillslopes and floodplains.
Currently, the model has a simple parameterization for the sediment deposition factors for floodplains and hillslopes. Sediment deposition is mainly calculated as a function of land use and slope, which does not explicitly take into account the effect of surface roughness. Surface roughness influences the capacity of flow to carry sediments downhill. This effect of surface roughness is partly captured by differentiating between agricultural and natural landscapes, but the representation of surface roughness should be further improved in the model.
Finally, including other types of soil erosion, such as landslides, gully erosion, glacial erosion and erosion due to tectonic uplift, is essential to capture the full dynamics of soil redistribution on the global scale.

5.3.2 Coupling soil redistribution to the biogeochemical cycles on a global scale

Even though this study mainly addresses sediment dynamics, it is relevant for further research related to the biogeochemical cycles. As shown before, soil redistribution can significantly impact the biogeochemical cycles through lateral transport of carbon and nutrients, and the on-site disruption of soil aggregates and burial of sediment. Therefore, future studies that aim to investigate and quantify the human impact on the global biogeochemical cycles should also focus on the coupling of soil redistribution to the biogeochemical cycles. This can be done by using the ESM framework in combination with the new sediment budget model.

A Appendices

A.1 Appendix of Chapter 2

Table A.1: List of data sets used in this study.

Category	Data set	Source	Spatial resolution	Temporal period	Variables
DEM	GTOPO elevation model	USGS (1996), Gesch et al. (1999)	30 arcsec		elevation
	ETOPO1 elevation model	Amante and Eakins (2009)	1 arcmin		elevation
	ETOPO2 elevation model	US Department of Commerce and NOAA (2001)	2 arcmin		elevation
	ETOPO5 Elevation Model	National Geophysical Data Center/ NESDIS/NOAA (1995)	5 arcmin		elevation
Climate	GPCC 0.5 degree data set	Schneider et al. (2011)	0.5 degree	Years 1989–2010	total yearly precipitation
	GPCC 0.25 degree data set	Meyer-Christoffer et al. (2011)	0.25 degree	years 1951–2000	total yearly precipitation
	GHCNDEX data set	CLIMDEX; Donat et al. (2013)	2.5 degree	years 1951–present	simple precipitation intensity index (SDII)
	Köppen–Geiger data set	Peel et al. (2007)	5 arcmin		Köppen–Geiger climate classifications
Soil	Global Soil Data set for use in Earth System Models (GSDE)	Shangguan et al. (2014)	30 arcsec		sand, silt and clay fractions, organic matter %, gravel %
	Harmonized World Soil Database (HWSD) version 1.2	Nachtergaele et al. (2009)	30 arcsec		volcanic soils
Land cover	GIMMS data set	ISLSCP II; Tucker et al. (2005), Hall et al. (2006)	0.25 degree	year 2002	normalized difference vegetation index (NDVI)
Land use	MODIS data set	ISLSCP II; Friedl et al. (2010), Hall et al. (2006)	0.25 degree	year 2002	land use fractions

MPI-ESM-LR	IPSL-CM5A-LR	CCSM4	MIROC-ESM	bcc-csm1-1
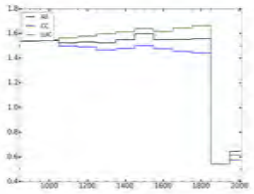	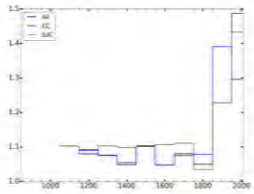	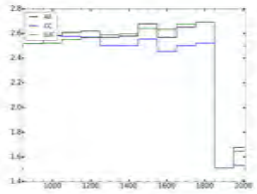	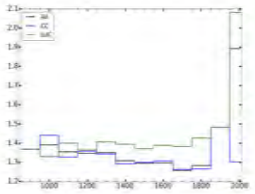	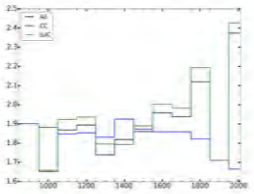
Africa				
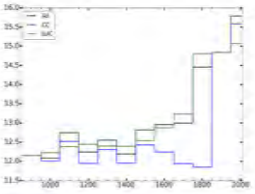	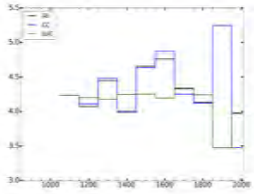	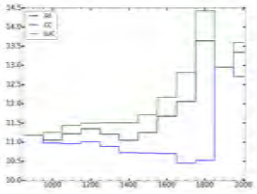	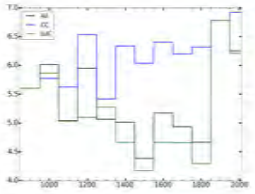	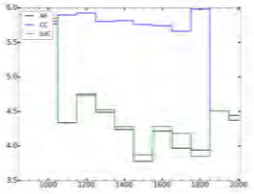
Asia				
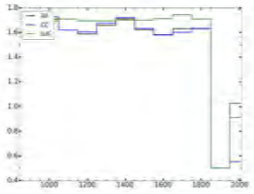	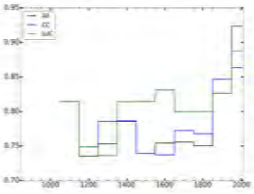	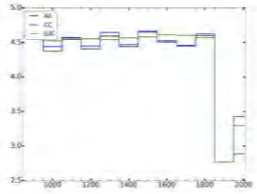	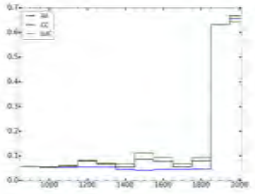	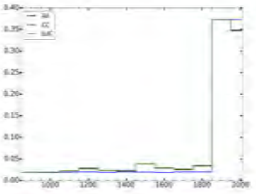
Australia				
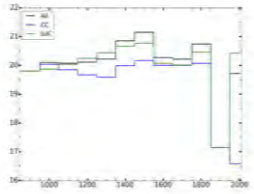	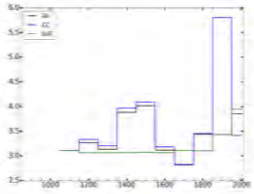	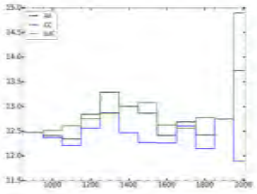	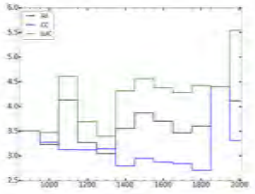	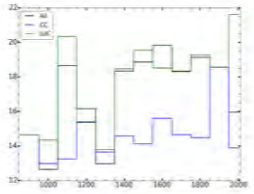
Central-America				

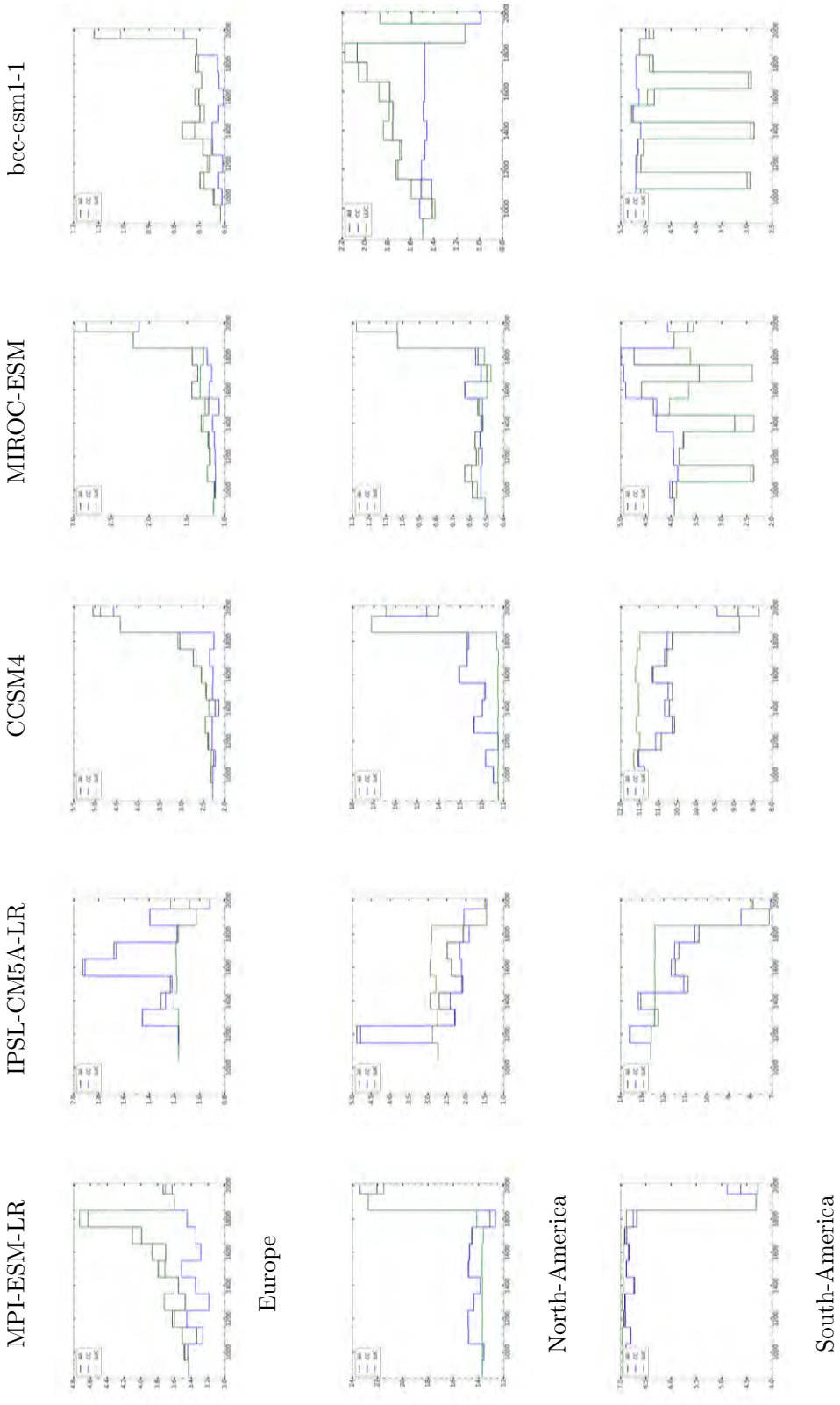

Figure A.1: Mean continental soil erosion rates for the last millennium for the climate change scenario (blue), land use change scenario (green) and default scenario (black) based on data from different CMIP5 models. Units are in $\mathrm{t\,ha^{-1}\,year^{-1}}$.

A.2 Appendix of Chapter 3

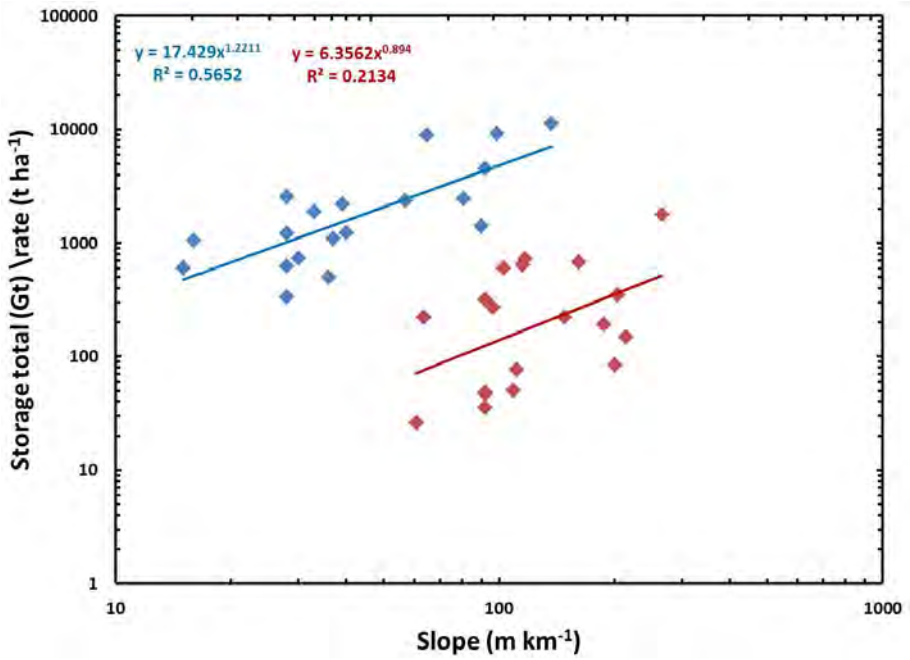

Figure A.2: Catchment slope versus change in sediment storage (red) and storage rate (blue).

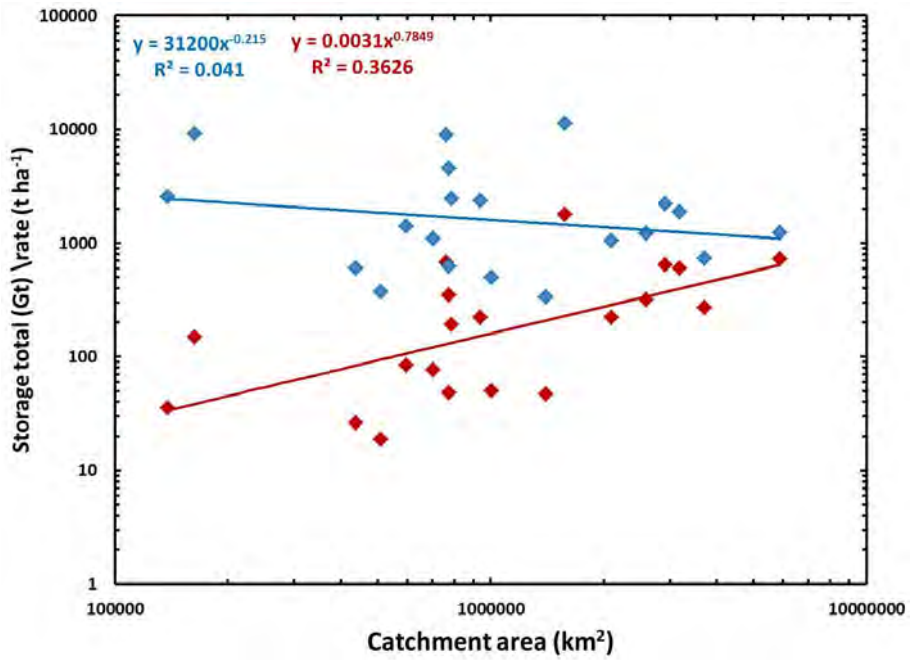

Figure A.3: Catchment area versus change in sediment storage (red) and storage rate (blue).

Table A.2: List of values for the residence time parameters, a_τ and b_τ

Continent	a_τ	b_τ
Europe	-9301752	1672772
Asia	-11385298	2047465
Africa	-13764033	2475242
Australia	-3359855	604217
North-America	-15542635	2795095
South-America	-22101816	3974660
Ventral-America	-2042211	367259

A.3 Appendix of Chapter 4

Table A.3: Global mean erosion rates of SOC, nitrogen (N) and phosphorus (P) for different land cover / land use types. The uncertainty in the mean is due to the uncertainty in erosion rates from the adjusted RUSLE model. Units are $\mathrm{g\,m^{-2}\,year^{-1}}$.

	SOC mean	SOC uncertainty	N mean	N uncertainty	P mean	P uncertainty
Forest	78.1	76 – 87.9	4.4	4.3 – 4.7	1.1	1.1 – 1.2
Shrub	29.4	22.4 – 63.8	2.1	1.6–4.5	0.8	0.6 – 1.4
Crop	34.8	32.9 – 38.4	2.7	2.6–3.0	1.0	0.9 – 1.1
Grass	29.2	21.7 – 34.6	1.9	1.4–2.2	0.5	0.3 – 0.6
Savanna	39.2	37.3 – 45.9	3.0	2.8 – 3.2	1.0	1.0 – 1.4
Bare	7.4	6.2 – 20	0.7	0.6–1.5	0.3	0.3 – 0.5

References

Angulo-Martinez, M., Lopez-Vicente, M., Vicente-Serrano, S. M., and Begueria, S. (2009). Estimating rainfall erosivity from daily precipitation records: a comparison among methods using data from the Ebro Basin (NE Spain). *Hydrology and Earth System Science*, 13:1907–1920.

Asselman, N. E. M., Middelkoop, H., and van Dijk, P. M. (2003). The impact of changes in climate and land use on soil erosion, transport and deposition of suspended sediment in the River Rhine. *Hydrological Processes*, 17(16):3225–3244.

Auerswald, K., Fiener, P., and Dikau, R. (2009). Rates of sheet and rill erosion in Germany A meta-analysis. *Geomorphology*, 111(3-4):182–193.

Balesdent, J., Chenu, C., and Balabane, M. (2000). Relationship of soil organic matter dynamics to physical protection and tillage. *Soil and Tillage Research*, 53(3-4):215–230.

Batjes, N. H. (1996). Total carbon and nitrogen in the soils of the world. *European Journal of Soil Science*, (47):151 163.

Bauer, J. E., Cai, W.-J., Raymond, P. a., Bianchi, T. S., Hopkinson, C. S., and Regnier, P. a. G. (2013). The changing carbon cycle of the coastal ocean. *Nature*, 504(7478):61–70.

Berhe, A. A., Harte, J., Harden, J. W., and Torn, M. S. (2007). The Significance of the Erosion-induced Terrestrial Carbon Sink. *Bioscience*, 57(4):337–346.

Bork, H.-R. (1989). SOIL EROSION DURING THE PAST MILLENNIUM IN CENTRAL EUROPE AND ITS SIGNIFICANCE WITHIN THE GEOMORPHODYNAMICS OF THE HOLOCENE. *CATENA*, 15:121–131.

Bork, H. R. and Lang, A. (2003). Quantification of past soil erosion and land use/land cover changes in Germany, in: Long term hillslope and fluvial system modelling. Concepts and case studies of the Rhine river catchment. *Springer*, 101:231–239.

Bosco, C., Rusco, E., and Montanarella, L. (2008). Actual soil erosion in the Alps. Technical report, European Commission. Joint Research Center. Institute for Environment and Sustainability.

Bracken, L. J. and Croke, J. (2007). The concept of hydrological connectivity and its contribution to understanding runoff-dominated geomorphic systems. *HYDROLOGICAL PROCESSES*, 21(February):1749–1763.

Cerdan, O., Govers, G., Le Bissonnais, Y., Van Oost, K., Poesen, J., Saby, N., Gobin, A., Vacca, A., Quinton, J., Auerswald, K., Klik, A., Kwaad, F., Raclot, D., Ionita, I., Rejman, J., Rousseva, S., Muxart, T., Roxo, M., and Dostal, T. (2010). Rates and spatial variations of soil erosion in Europe: A study based on erosion plot data. *Geomorphology*, 122(1-2):167–177.

Chang, K. T. and Tsai, B. W. (1991). The effect of DEM resolution on slope and aspect mapping. *Cartography and Geographic Information Science*, (18):69–77.

Chaopricha, N. T. and Marín-Spiotta, E. (2014). Soil burial contributes to deep soil organic carbon storage. *Soil Biology and Biochemistry*, 69:251–264.

Chappell, A., Baldock, J., and Sanderman, J. (2015). The global significance of omitting soil erosion from soil organic carbon cycling schemes. (October):1–5.

Ciais, P., Sabine, C., Bala, G., Bopp, L., Brovkin, V., Canadell, J., Chhabra, A., DeFries, R., Galloway, J., Heimann, M., et al. (2014). Carbon and other biogeochemical cycles. In *Climate change 2013: the physical science basis. Contribution of Working Group I to the Fifth Assessment Report of the Intergovernmental Panel on Climate Change*, pages 465–570. Cambridge University Press.

Cooper, K. (2011). Evaluation of the Relationship between the RUSLE R-Factor and Mean Annual Precipitation.

De Jong, S. M., Brouwer, L. C., and Riezebos, H. T. (1998). Erosion hazard assessment in the Peyne catchment, France, Working paper DeMon-2 Project.

de Moor, J. J. W. and Verstraeten, G. (2008). Alluvial and colluvial sediment storage in the Geul River catchment (The Netherlands) Combining field and modelling data to construct a Late Holocene sediment budget. *Geomorphology*, 95(3-4):487–503.

de Vente, J. and Poesen, J. (2005). Predicting soil erosion and sediment yield at the basin scale: Scale issues and semi-quantitative models. *Earth-Science Reviews*, 71(1-2):95–125.

Diodato, N. and Bellocchi, G. (2010). MedREM, a rainfall erosivity model for the Mediterranean region. *Journal of Hydrology*, 387(1-2):119–127.

Doetterl, S., Van Oost, K., and Six, J. (2012). Towards constraining the magnitude of global agricultural sediment and soil organic carbon fluxes. *Earth Surface Processes and Landforms*, 37(6):642–655.

Filippelli, G. M. (2008). The Global Phosphorus Cycle : Past , Present , and Future. *Elements*, 4:89–95.

Food and of the United Nations, A. O. (2015). *World fertilizer trends and outlook to 2018*. Rome,Italy.

Friedlingstein, P., Meinshausen, M., Arora, V. K., Jones, C. D., Anav, A., Liddicoat, S. K., and Knutti, R. (2014). Uncertainties in CMIP5 Climate Projections due to Carbon Cycle Feedbacks. *Journal of Climate*, 27(2):511–526.

Galy, V., France-Lanord, C., Beyssac, O., Faure, P., Kudrass, H., and Palhol, F. (2007). Efficient organic carbon burial in the Bengal fan sustained by the Himalayan erosional system. *Nature*, 450(7168):407–10.

Galy, V., Peucker-Ehrenbrink, B., and Eglinton, T. (2015). Global carbon export from the terrestrial biosphere controlled by erosion. *Nature*, 521(7551):204–207.

García-Ruiz, J. M. (2010). The effects of land uses on soil erosion in Spain: A review. *Catena*, 81:1–11.

Goll, D. S. (2013). *The influence of phosphorus cycling and temperature acclimation of photosynthesis*. PhD thesis, Max-Planck Institute for Meteorology, Bundesstrasse 53, Hamburg, Germany.

Goovaerts, P. (1999). Using elevation to aid the geostatistical mapping of rainfall erosivity. *CATENA*, 34:227–242.

Goudie, A. S. and Viles, H. A. (2012). Weathering and the global carbon cycle: Geomorphological perspectives. *Earth-Science Reviews*, 113(1-2):59–71.

Gumiere, S. J., Le Bissonnais, Y., Raclot, D., and Cheviron, B. (2011). Vegetated filter effects on sedimentological connectivity of agricultural catchments in erosion modelling: a review. *Earth Surface Processes and Landforms*, 36(1):3–19.

Harden, J. W., Sharpe, J. M., Parton, W. J., Ojima, D. S., Fries, T. L., Huntington, T. G., and Dabney, S. M. (1999). Dynamic replacement and loss of soil carbon on eroding cropland. *Global Biogeochemical Cycles*, 13(4):885–901.

Hoffmann, T. (2015). Sediment residence time and connectivity in non-equilibrium and transient geomorphic systems. *Earth Science Reviews*. Accepted.

Hoffmann, T., Erkens, G., Cohen, K. M., Houben, P., Seidel, J., and Dikau, R. (2007). Holocene floodplain sediment storage and hillslope erosion within the Rhine catchment. *The Holocene*, 17(1):105–118.

Hoffmann, T., Penny, D., Stinchcomb, G., Vanacker, V., and Lu, X. (2015). Global Soil and Sediment transfers in the Anthropocene. *PAGES MAGAZINE*, 23(1).

Hoffmann, T., Schlummer, M., Notebaert, B., Verstraeten, G., and Korup, O. (2013). Carbon burial in soil sediments from Holocene agricultural erosion, Central Europe. *Global Biogeochemical Cycles*, 27(3):828–835.

Honisch, B., Hemming, N. G., Archer, D., Siddall, M., and McManus, J. F. (2009). Atmospheric Carbon Dioxide Concentration Across the Mid-Pleistocene Transition. *Science*, 324(5934):1551–1554.

Hooke, J. (2003). Coarse sediment connectivity in river channel systems: a conceptual framework and methodology. *Geomorphology*, 56(1-2):79–94.

Hooke, R. L. (2000). On the history of humans as geomorphic agents. *Geology*, 28(9):843–846.

Houben, P., Hoffmann, T., Zimmermann, A., and Dikau, R. (2006). Land use and climatic impacts on the Rhine system (RheinLUCIFS): Quantifying sediment fluxes and human impact with available data. *Catena*, 66(1-2):42–52.

Howarth, R., Jensen, H. S., Marino, R., Postma, H., and Tiesen, H. (1995). Transport to and processing of P in near-shore and oceanic waters. *SCOPE*, 54:323–345.

Howarth, R. W. (2008). Coastal nitrogen pollution: A review of sources and trends globally and regionally. *Harmful Algae*, 8(1):14–20.

Hudson, N. (1971). *Soil Conservation*. Cornell University Press, Ithaca, USA.

Hurrell, J. and Visbeck, M. (2011). WCRP Coupled Model Intercomparison Project - Phase 5 Editorial WCRP Modelling Strategy Developments.

Ito, A. (2007). Simulated impacts of climate and land-cover change on soil erosion and implication for the carbon cycle, 1901 to 2100. *Geophysical Research Letters*, 34(9).

Joetzjer, E., Douville, H., Delire, C., and Ciais, P. (2013). Present-day and future Amazonian precipitation in global climate models: CMIP5 versus CMIP3. *Climate Dynamics*, 41(11-12):2921–2936.

Klinkenberg, B. and Goodchild, M. F. (1992). The fractal properties of topography: A comparison of methods. *Earth Surface Processes Landforms*, (17):217–234.

Lal, R. (2003). Soil erosion and the global carbon budget. *Environment international*, 29(4):437–50.

Lal, R. (2005). Soil erosion and carbon dynamics. *Soil and Tillage Research*, 81(2):137–142.

Lang, A., Bork, H.-R., Mäckel, R., Preston, N., Wunderlich, J., and Dikau, R. (2003). Changes in sediment flux and storage within a fluvial system: some examples from the Rhine catchment. *Hydrological Processes*, 17(16):3321–3334.

Le Quéré, C., Peters, G. P., Andres, R. J., Andrew, R. M., Boden, T., Ciais, P., Friedlingstein, P., Houghton, R. a., Marland, G., Moriarty, R., Sitch, S., Tans, P., Arneth, A., Arvanitis, A., Bakker, D. C. E., Bopp, L., Canadell, J. G., Chini, L. P., Doney, S. C., Harper, A., Harris, I., House, J. I., Jain, A. K., Jones, S. D., Kato, E., Keeling, R. F., Klein Goldewijk, K., Körtzinger, A., Koven, C., Lefèvre, N., Omar, A., Ono, T., Park, G.-H., Pfeil, B., Poulter, B., Raupach, M. R., Regnier, P., Rödenbeck, C., Saito, S., Schwinger, J., Segschneider, J., Stocker, B. D., Tilbrook, B., van Heuven, S., Viovy, N., Wanninkhof, R., Wiltshire, A., Zaehle, S., and Yue, C. (2013). Global carbon budget 2013. *Earth System Science Data Discussions*, 6(2):689–760.

Lehner, B., Verdin, K., and Jarvis, A. (2006). HydroSHEDS. pages 1–27.

Lenton, T. M. (2011). Early warning of climate tipping points. *nature climate change*, 1:201–209.

Léonard, J. and Richard, G. (2004). Estimation of runoff critical shear stress for soil erosion from soil shear strength. *Catena*, 57(3):233–249.

Liu, S., Bliss, N., Sundquist, E., and Huntington, T. G. (2003). Modeling carbon dynamics in vegetation and soil under the impact of soil erosion and deposition. *Global Biogeochemical Cycles*, 17(2).

Lohmann, U., Sausen, R., Bengtsson, L., Cubasch, U., Perlwitz, J., and Roeckner, E. (1993). The Köppen–Geiger climate classification as a diagostic tool for general circulation models. *Climate Research*, (3):177–193.

Ludwig, W. and Probst, J.-L. (1998). RIVER SEDIMENT DISCHARGE TO THE OCEANS: PRESENT-DAY CONTROLS ANd GLOBAL BUDGETS. *Americal Journal of Science*, 298:265–295.

Lüthi, D., Le Floch, M., Bereiter, B., Blunier, T., Barnola, J.-M., Siegenthaler, U., Raynaud, D., Jouzel, J., Fischer, H., Kawamura, K., and Stocker, T. F. (2008). High-resolution carbon dioxide concentration record 650,000-800,000 years before present. *Nature*, 453(7193):379–82.

Mayorga, E., Seitzinger, S. P., Harrison, J. A., Dumont, E., Beusen, A. H., Bouwman, A., Fekete, B. M., Kroeze, C., and Van Drecht, G. (2010). Global Nutrient Export from WaterSheds 2 (NEWS 2): Model development and implementation. *Environmental Modelling & Software*, 25(7):837–853.

Mehran, A., AghaKouchak, A., and Phillips, T. J. (2014). Evaluation of CMIP5 continental precipitation simulations relative to satellite-based gauge-adjusted observations. *Journal of Geophysical Research : Atmospheres*, 119:1695–1707.

Merritt, W., Letcher, R., and Jakeman, A. (2003). A review of erosion and sediment transport models. *Environmental Modelling & Software*, 18(8-9):761–799.

Meusburger, K., Steel, a., Panagos, P., Montanarella, L., and Alewell, C. (2012). Spatial and temporal variability of rainfall erosivity factor for Switzerland. *Hydrology and Earth System Sciences*, 16(1):167–177.

Mikhailova, E. A., Bryant, R. B., Schwager, S. J., and Smith, s. (1997). Predicting rainfall erosivity in Honduras. *Soil Science Society America Journal*, (61):273–279.

Milliman, J. D. and Meade, R. H. (1983). WORLD-WIDE DELIVERY OF RIVER SEDIMENT TO THE OCEANS. *THE JOURNAL OF GEOLOGY*, 91(1):1–21.

Milliman, J. D. and Syvitski, J. P. M. (1992). Geomorphic / Tectonic Control of Sediment Discharge to the Ocean : The Importance of Small Mountainous Rivers. *The Journal of Geology*, 100(5):525–544.

Montgomery, D. R. (2007). Soil erosion and agricultural sustainability. *PNAS*, 104(33):13268–13272.

Morgan, R. P. C. (2009). *Soil erosion and conservation*. John Wiley & Sons.

Nadeu, E., Gobin, A., Fiener, P., van Wesemael, B., and van Oost, K. (2015). Modelling the impact of agricultural management on soil carbon stocks at the regional scale: the role of lateral fluxes. *Global change biology*, 21(8):3181–92.

Naipal, V., Reick, C., Pongratz, J., and Van Oost, K. (2015). Improving the global applicability of the RUSLE model - adjustement of the topographical and rainfall erosivity factors. *Geoscientific Model Development*, (8):1–22.

Nearing, M. A. (1997). A single, continues function for slope steepness influence on soil loss. *Soil Science Society Americal Journal*, 61:917–929.

Notebaert, B., Vaes, B., Verstraeten, G., and Govers, G. (2006). WaTEM / SEDEM version 2006 Manual.

Notebaert, B., Verstraeten, G., Vandenberghe, D., Marinova, E., Poesen, J., and Govers, G. (2011). Changing hillslope and fluvial Holocene sediment dynamics in a Belgian loess catchment. *Journal of Quaternary Science*, 26(1):44–58.

of Agriculture, U. D. (2000). Summary Report: 1997 National Resources Inventory (revised December 2000). Technical report, Natural Resources Conservation Service, Washington, DC, USA, and statistical Laboratory, Iowa State University, Ames, Iowa, USA.

of Agriculture, U. S. D. (1978). *PREDICTING RAINFALL EROSION LOSSES. A GUIDE TO CONSERVATION PLANNING*. Science and Education Administration.

Oliveira, P. T. S., Wendland, E., and Nearing, M. a. (2013). Rainfall erosivity in Brazil: A review. *Catena*, 100:139–147.

Panagos, P., Borrelli, P., Meusburger, K., Alewell, C., Lugato, E., and Montanarella, L. (2015). Estimating the soil erosion cover-management factor at the European scale. *Land Use Policy*, 48:38–50.

Peel, M. C., Finlayson, B. L., and Mcmahon, T. A. (2007). Updated world map of the Koeppen-Geiger climate classification. *Hydrology and Earth System Science*, 11:1633–1644.

Pelletier, J. D. (2012). A spatially distributed model for the long-term suspended sediment discharge and delivery ratio of drainage basins. *Journal of Geophysical Research*, 117(F2):F02028.

Peucker-Ehrenbrink, B. (2009). Land2Sea database of river drainage basin sizes, annual water discharges, and suspended sediment fluxes. *Geochemistry, Geophysics, Geosystems*, 10(6).

Pimentel, D. (2006). Soil Erosion: A Food and Environmental Threat. *Environment, Development and Sustainability*, 8(1):119–137.

Pimentel, D., Harvey, C., Resosudarmo, P., Sinclair, K., Kurz, D., McNair, M., Crist, S., Shpritz, L., Fitton, L., Saffouri, R., and Blair, R. (1995). Environmental and Economic Costs of Soil Erosion and Conservations Benefits. *Science*, 267(5201):1117–1123.

Poesen, J. W., Torri, D., and Bunte, K. (1994). Effects of rock fragments on soil erosion by water at different spatial scales: a review. *CATENA*, (23):141–166.

Pradhan, N. R., Tachikawa, Y., and Takara, K. (2006). A downscaling method of topographic index distribution for matching the scales of model application and parameter identification. *Hydrological Processes*, 20(6):1385–1405.

Quinn, P., Beven, K., and Chevallier, P. (1991). THE PREDICTION OF HILLSLOPE FLOW PATHS FOR DISTRIBUTED HYDROLOGICAL MODELLING USING DIGITAL TERRAIN MODELS. *Hydrological Processes*, 5:59–79.

Quinton, J. N., Govers, G., Van Oost, K., and Bardgett, R. D. (2010). The impact of agricultural soil erosion on biogeochemical cycling. *Nature Geoscience*, 3(5):311–314.

Quinton, J. N., Mataix-Solera, J., Brevik, E. C., Cerda, A., Pereg, L., Six, J., and Van Oost, K. (2015). SOIL: A Journey Through Time and Space. In *A Voyage Through Scales*, page 9297.

Raymond, P. a., Hartmann, J., Lauerwald, R., Sobek, S., McDonald, C., Hoover, M., Butman, D., Striegl, R., Mayorga, E., Humborg, C., Kortelainen, P., Dürr, H., Meybeck, M., Ciais, P., and Guth, P. (2013). Global carbon dioxide emissions from inland waters. *Nature*, 503(7476):355–9.

Regnier, P., Friedlingstein, P., Ciais, P., Mackenzie, F. T., Gruber, N., Janssens, I. a., Laruelle, G. G., Lauerwald, R., Luyssaert, S., Andersson, A. J., Arndt, S., Arnosti, C., Borges, A. V., Dale, A. W., Gallego-Sala, A., Goddéris, Y., Goossens, N., Hartmann, J., Heinze, C., Ilyina, T., Joos, F., LaRowe, D. E., Leifeld, J., Meysman, F. J. R., Munhoven, G., Raymond, P. a., Spahni, R., Suntharalingam, P., and Thullner, M. (2013). Anthropogenic perturbation of the carbon fluxes from land to ocean. *Nature Geoscience*, 6(8):597–607.

Renard, K. G., Foster, G. R., Weesies, G. A., Mccool, D. K., and Yoder, D. C. (1997). *Predicting Soil Erosion by Water: a Guide to Conservation Planning with the Revised Universal Soil Loss Equation (RUSLE)*. USDA, Washington, DC, USA.

Renard, K. G. and Freimund, J. R. (1994). Using monthly precipitation data to estimate the R-Factor in the revised USLE. *Journal of Hydrology*, (157):287–306.

Renschler, C. S. and Harbor, J. (2002). Soil erosion assessment tools from point to regional scales the role of geomorphologists in land management research and implementation. 47:189–209.

Schuman, G. E .and Janzen, H. H. and Herrick, J. E. (2002). Soil carbon dynamics and potential carbon sequestration by rangelands. *Environmental Pollution*, 116(3):391–396.

Seitzinger, S. P., Harrison, J. A., Dumont, E., Beusen, A. H. W., and Bouwman, A. F. (2005). Sources and delivery of carbon, nitrogen, and phosphorus to the coastal zone: An overview of Global Nutrient Export from Watersheds (NEWS) models and their application. *Global Biogeochemical Cycles*, 19(4).

Shangguan, W., Dai, Y., Duan, Q., Liu, B., and Yuan, H. (2014). A global soil data set for earth system modeling. *Journal of Advances in Modeling Earth Systems*, 6:249–263.

Slaymaker, O. (2003). The sediment budget as conceptual framework and management tool. *Hydrobiologia*, (494):71–82.

Stallard, R. F. (1998). Terrestrial sedimentation and the carbon cycle : Coupling weathering and erosion to carbon burial processes. *Global Biogeochemical Cycles*, 12(2):231–257.

Steegen, A., Govers, G., Takken, I., Nachtergaele, J., Poesen, J., and Merckx, R. (2001). Factors Controlling Sediment and Phosphorus Export from Two Belgian Agricultural Catchments. *Journal of Environment Quality*, 30(4):1249.

Stewart, C. E., Paustian, K., Conant, R. T., Plante, A. F., and Six, J. (2007). Soil carbon saturation: concept, evidence and evaluation. *Biogeochemistry*, 86(1):19–31.

Stocking, M. (1984). Rates of erosion and sediment yield in the African environment. *IAHS*, (144).

Survey, U. G. (1996). GTOPO30 Arc-Second Elevation Data Set.

Syvitski, J. P. M., Peckham, S. D., Hilberman, R., and Mulder, T. (2003). Predicting the terrestrial flux of sediment to the global ocean: a planetary perspective. *Sedimentary Geology*, 162(1-2):5–24.

Syvitski, J. P. M., Vörösmarty, C. J., Kettner, A. J., and Green, P. (2005). Impact of humans on the flux of terrestrial sediment to the global coastal ocean. *Science (New York, N.Y.)*, 308(5720):376–80.

Taylor, K. E., Stouffer, R. J., and Meehl, G. A. (2009). A Summary of the CMIP5 Experiment Design. pages 1–33.

Thapa, P. K. (2010). *Physically-based spatially distributed rainfall runoff modelling for soil erosion estimation*. PhD thesis, Institute für Wasserbau der Universität Stuttgart.

Todd-Brown, K, E., Randerson, J. T., Post, W. M., Hoffman, F. M., Tarnocai, C., Schuur, E. A. G., and Allison, S. D. (2013). Causes of variation in soil carbon simulations from CMIP5 Earth system models and comparison with observations. *Biogeosciences*, (10):1717 1736.

Todd-Brown, K. E. O., Randerson, J. T., Hopkins, F., Arora, V., Hajima, T., Jones, C., Shevliakova, E., Tjiputra, J., Volodin, E., Wu, T., Zhang, Q., and Allison, S. D. (2014). Changes in soil organic carbon storage predicted by Earth system models during the 21st century. *Biogeosciences*, 11(8):2341–2356.

Torri, D., Poesen, J., and Borselli, L. (1997). Predictability and uncertainty of the soil erodibility factor using a global dataset. *CATENA*, (31):1–22.

Toy, T. J., Foster, G. R., and Renard, K. G. (2002). *Soil erosion: processes, prediction, measurement, and control*. John Wiley & Sons.

United States Environmental Protection Agency, E. (2001). Stormwater Phase 2 Final RUSLE, Construction Rainfall Erosivity Waiver. Technical report, Washington, DC, USA. EPA 833-F-00-014.

Van der Knijff, J. M., Jones, R. J. A., and Montanarella, L. (1999). Soil Erosion Risk Assessment in Italy.

Van Oost, K., Quine, T. A., Govers, G., De Gryze, S., Six, J., Harden, J. W., Ritchie, J. C., McCarty, G. W., Heckrath, G., Kosmas, C., Giraldez, J. V., da Silva, J. R. M., and Merckx, R. (2007). The impact of agricultural soil erosion on the global carbon cycle. *Science (New York, N.Y.)*, 318(5850):626–9.

Van Oost, K. V., Verstraeten, G., Doetterl, S., Notebaert, B., Wiaux, F., and Broothaerts, N. (2012). Legacy of human-induced C erosion and burial on soil atmosphere C exchange. *PNAS*, 109(47):19492–19497.

Van Rompaey, A. J. J., Verstraeten, G., Van Oost, K., Govers, G., and Poesen, J. (2001). MODELLING MEAN ANNUAL SEDIMENT YIELD USING A DISTRIBUTED APPROACH. *Earth Surface Processes and Landforms*, 26:1221–1236.

Vannoppen, W., Vanmaercke, M., De Baets, S., and Poesen, J. (2015). A review of the mechanical effects of plant roots on concentrated flow erosion rates. *Earth-Science Reviews*, 150:666–678.

Verstraeten, G. and Poesen, J. (2000). Estimating trap efficiency of small reservoirs and ponds : methods and implications for the assessment of sediment yield. *Progress in Physical Geography*, 24(2):219–251.

Vonk, J. E., Sánchez-García, L., van Dongen, B. E., Alling, V., Kosmach, D., Charkin, a., Semiletov, I. P., Dudarev, O. V., Shakhova, N., Roos, P., Eglinton, T. I., Andersson, a., and Gustafsson, O. (2012). Activation of old carbon by erosion of coastal and subsea permafrost in Arctic Siberia. *Nature*, 489(7414):137–40.

Wall, D. H. and Six, J. (2015). Give soils their due. *Science*, 347(6223):695–695.

Walling, D. and Collins, A. (2008). The catchment sediment budget as a management tool. *Environmental Science & Policy*, 11(2):136–143.

Walling, D. E., Collins, A. L., Sichingabula, H. M., and Leeks, G. J. L. (2001). INTEGRATED ASSESSMENT OF CATCHMENT SUSPENDED SEDIMENT BUDGETS : A ZAMBIAN EXAMPLE. *Land Degradation and Development*, 12:387–415.

Ward, P. J., van Balen, R. T., Verstraeten, G., Renssen, H., and Vandenberghe, J. (2009). The impact of land use and climate change on late Holocene and future suspended sediment yield of the Meuse catchment. *Geomorphology*, 103(3):389–400.

Wilkinson, B. H. and McElroy, B. J. (2007). The impact of humans on continental erosion and sedimentation. *Geological Society of America Bulletin*, 119(1-2):140–156.

Wilkinson, S. N., Prosser, I. P., Rustomji, P., and Read, A. M. (2009). Modelling and testing spatially distributed sediment budgets to relate erosion processes to sediment yields. *Environmental Modelling & Software*, 24(4):489–501.

Willenbring, J. K., Codilean, A. T., and McElroy, B. (2013). Earth is (mostly) flat: Apportionment of the flux of continental sediment over millennial time scales. *Geology*, 41(3):343–346.

Wischmeier, W. H. and Smith, D. D. (1978). *Predicting Rainfall Erosion Losses. A guide to conservation planning*. Washington, USA. 58 pp.

Wittmann, H. and von Blanckenburg, F. (2009). Cosmogenic nuclide budgeting of floodplain sediment transfer. *Geomorphology*, 109(3-4):246–256.

Yang, D., Kanae, S., Oki, T., Koike, T., and Musiake, K. (2003). Global potential soil erosion with reference to land use and climate changes. *Hydrological Processes*, 17(14):2913–2928.

Zhang, B., Yang, Y., and Zepp, H. (2004). Effect of vegetation restoration on soil and water erosion and nutrient losses of a severely eroded clayey Plinthudult in southeastern China. *Catena*, 57(1):77–90.

Zhang, W. and Montgomery, D. R. (1994). Digital elevation model grid size, landscape representation, and hydrologic simulations. *Water Resources Research*, (30):1019–1028.

Zhang, X., Drake, N., and Wainwright, J. (2002). Scaling land surface parameters for global-scale soil erosion estimation. *Water Resources Research*, 38(9):19–1–19–9.

Zhang, X., Drake, N. A., Wainwright, J., and Mulligan, M. (1999). COMPARISON OF SLOPE ESTIMATES FROM LOW RESOLUTION DEMS: SCALING ISSUES AND A FRACTAL METHOD FOR THEIR SOLUTION. *Earth Surface Processes Landforms*, 14:763–779.

Zhao, J., Van Oost, K., Chen, L., and Govers, G. (2015). Moderate topsoil erosion rates constrain the magnitude of the erosion-induced carbon sink and agricultural productivity losses on the Chinese Loess Plateau. *Biogeosciences Discussions*, 12(17):14981–15010.

Acronyms

bcc-csm1	Beijing Climate Center Climate System Model
CCSM4	Community Earth System Model 4.0; National Center for Atmospheric Research
CMIP5	project: Coupled Model Intercomparison Project Phase 5
CO_2	carbon dioxide
DEM	digital elevation model
ESM	Earth System Model
HUC4	Hydrologic Unit Code 4
GSDE	Global Soil Data set for use in Earth System Models
IPSL-CM5A	French earth system model; Institut Pierre-Simon Laplace
LAI	Leaf Area Index
LGM	Last Glacial Maximum
MIROC-ESM	Japanese earth system model; Japan Agency for Marine-Earth Science and Technology, Atmosphere and Ocean Research Institute (The University of Tokyo), and National Institute for Environmental Studies
MPI-ESM	Max Planck Institute Earth System Model
NDVI	Normalized Difference Vegetation Index
NRI	National Resources Inventory
PN	particulate nitrogen
POC	particulate organic carbon
PP	particulate phosphorus
SDII	simple precipitation intensity index
RUSLE	Revised Universal Soil Loss Equation
SOC	soil organic carbon
USLE	Universal Soil Loss Equation

List of Figures

List of Tables

Acknowledgements

I would like to express my gratitude to my supervisor Dr. Christian Reick, for creating the needed environment to do my research, and for giving me the freedom to develop my own ideas and the needed guidance to realize these ideas into this thesis.
I would like to thank Prof.Dr. Kristof Van Oost and Dr. Thomas Hoffmann for the scientific discussions through skype and involving me in the research community on soil erosion. I also would like to thank Prof.Dr. Kristof Van Oost for the very instructive and pleasant stay in Louvain la Neuve, which really gave the needed boost to my research.
I thank Dr. Julia Pongratz for the useful advises during my PhD, and Veronica Gayler and Reiner Schnur for the support whenever I needed it. I also would like to thank, Prof.Dr. Martin Claussen, and Prof.Dr. Alexander Loew for being motivating members of my advisory panel.
A big thank you to my long-time office mate Andreas, for making my stay in the office pleasant, and for all the advises. Also a big thank you to other fellow PhD colleagues and postdocs for adding more fun to my PhD time: Roger, Rohit, Fabio, Sarah-Sylvia, Jessica, Max, Ritthik, Josiane, Cheska. And ofcourse, a special thank you to my friends Julia and Marjan for always being there for me, and the funny lunch times we had together.
Furthermore, I like to take this opportunity to thank all the staff from the IMPRS school. Especially, Antje Weitz, Cornelia Kampmann, and Wiebke Böhm for caring about my progress and well-being, and making my PhD time as smooth as possible.
I thank my family and friends, who are spread all over the world, but still close to me. Especially, my father who introduced me into science and was always there to share his expertise and knowledge on climate change. Thank you Daniel, for the critical discussions about my research, the love, and understanding in difficult times. I am sure all of this made my thesis possible.
Finally I like to express my gratitude to everyone who influenced my research in any way.

Aus dieser Dissertation hervorgegangene Vorveröffentlichungen

List of Publications

Naipal, V., Reick, C., Pongratz, J., and Van Oost, K.: Improving the global applicability of the RUSLE model - adjustment of the topographical and rainfall erosivity factors, Geosci. Model Dev., 8, 28932913, doi:10.5194/gmd-8-2893-2015, 2015.

Eidesstattliche Versicherung
Declaration on Oath

Hiermit erkläre ich an Eides statt, dass ich die vorliegende Dissertationsschrift selbst verfasst und keine anderen als die angegebenen Quellen und Hilfsmittel benutzt habe.

I hereby declare, on oath, that I have written the present dissertation by myself and have not used other than the acknowledged resources and aids.

Hamburg, den 21. Januar 2016